Vibrational Energy Distribution, Electron Density and Electron Temperature Behavior in Nanosecond Pulse Discharge Plasmas by Raman and Thomson Scattering

Dissertation

Presented in Partial Fulfillment of the Requirements for the Degree Doctor of Philosophy in the Graduate School of The Ohio State University

By

Andrew M. Roettgen, B.S., M.S.

Graduate Program in Mechanical Engineering

The Ohio State University

2015

Dissertation Committee:

Professor Igor V. Adamovich, Advisor

Professor Jeffrey Sutton

Professor Vishwanath Subramaniam

Professor Emeritus J. William Rich

Abstract

Kinetic processes controlling N_2 vibrational distribution, electron temperature and electron density in nanosecond pulse, nonequilibrium plasma, electric discharges are studied through laser scattering diagnostic techniques. The experiments are conducted in high pulse energy ($\geq$4 mJ/pulse), nanosecond pulse gas discharge plasmas at moderate pressures (75-200 torr) in nitrogen, air, helium, H_2-He and O_2-He mixtures.

In electric discharges, local energy loading is a function of the electron number density (n_e) and electron temperature (T_e). Furthermore, electron temperature, and more specifically, electron energy distribution function (EEDF) control the electron energy partition in nonequilibrium plasmas by controlling the rates of critical kinetic processes including ionization, vibrational and electronic excitation, and recombination of molecules, atoms and electrons in the gas discharge. Thus, obtaining time-resolved, quantitative measurements for these values (n_e, T_e, and EEDF) is critical in understanding the energy requirements for sustaining these discharges, as well as discerning how electron energy is partitioned among different molecular energy modes, and which excited species and radicals are generated in the plasma. Furthermore, in molecular plasmas, significant electron energy is loaded into vibrational modes. Study of temporally resolved vibrational distribution function (VDF) and vibrational

temperature (T_v) is important in quantifying vibrational energy loading and relaxation in these plasmas. This affects the rate of temperature rise in nanosecond pulse discharges and the afterglow, as well as rates of vibrationally stimulated chemical reactions, such as NO formation. Applications of these studies include plasma flow control (PFC), plasma assisted combustion (PAC), electrically excited laser development and various plasma bio-medical applications.

Time-resolved N_2 vibrational distribution function (VDF) and first-level N_2 vibrational temperature have been measured via spontaneous Raman scattering in a nanosecond pulse, nonequilibrium, single-filament gas discharge sustained between two spherical copper electrodes. Gases studied include nitrogen and air (P=100 torr). Highly nonequilibrium N_2 VDFs have been observed (vibrational levels up to v=12 significantly populated and detected). Results in nitrogen have been compared with a 0-D, master equation kinetic model.

A Thomson scattering diagnostic, including a solid state Nd:YAG laser as the pump source, a custom-made glass test cell, and custom-built triple-grating spectrometer has been developed. Thomson scattering has very low signal intensity, and is therefore highly susceptible to several types of interference. Rayleigh scattering interference has been filtered from the spectra by using a spectral mask in the spectrometer, while a second slit was used to provide critical stray light rejection. Background interference due to plasma emission has been subtracted.

Time-resolved electron number density, electron temperature and electron energy distribution function (EEDF) have been measured via the Thomson scattering diagnostic. Studies of two highly nonequilibrium plasma environments have been conducted, including a nanosecond pulse, single-filament discharge sustained between

two spherical copper electrodes, as well as a nanosecond pulse near surface discharge (which develops initially as a surface ionization wave). Studies in helium, as well as mixtures of H_2 in helium and O_2 in helium have been conducted in the single-filament discharge, while a study in helium has been conducted in the near surface discharge. Results in helium for the single-filament discharge have been compared with a 2-D, axisymmetric, kinetic model. Electron density measurements in these experiments ranged from 10^{13} - 10^{15} cm^{-3}, while electron temperatures were observed to range from 0.1 - 7.0 eV.

Dedicated to my parents, Mark and Connie, whose unwavering support through my educational pursuits has been greatly appreciated

Acknowledgments

I wish to thank my advisor, Dr. Igor Adamovich, as well as Dr. Walter Lempert, for their unwavering support, encouragement and shared insight in my graduate studies and research.

I also want to express my gratitude to Dr. Vish Subramaniam, Dr. Jeffrey Sutton and Dr. J. William Rich for serving on my committee and providing helpful research discussions, as well as Dr. Kraig Frederickson for his patient mentorship in the lab.

Also, I would thank the financial supporters for my work and education, including the Airforce Office of Scientific Research (AFOSR) Multi-University Research Initiative (MURI), the National Science Foundation (NSF), the Department of Energy (DOE), and the Department of Defense (DoD) through the Science, Mathematics and Research for Transformation (SMART) fellowhsip program.

Furthermore, I want to express my sincere thanks and appreciation to all of my fellow students, post-doctoral researchers, research scientists and close friends over my years at the university. Whether through collaborative work and discussions, or social gatherings, our interactions and time together have left a profound impact on me both personally and professionally.

I would also like to thank my family, my mother Connie, father Mark, sister Amy and brother Ben for their encouragement, support and understanding throughout my academic pursuits.

Lastly, I offer a prayer of thanksgiving to God, who created the universe to be scientifically discoverable, who created me and my mind with the aptitude for such reasearch, and sent his son, my Lord and Savior Jesus Christ to die for my sin and the sin of the world. To him be all of the glory! Amen.

Vita

April 25, 1988 ..... Born - Racine, WI USA

2010 ..... B.S. Aerospace Engineering,
The Ohio State University

2014 ..... M.S. Mechanical Engineering,
The Ohio State University

2010-present ..... Graduate Research Fellow,
The Ohio State University.

Publications

Research Publications

J.R. Bruzzese, A.M. Roettgen, and I.V. Adamovich "The Effect of Iodine Dissociation and Flow Cooling on Gain and Output Power in an Electric Discharge Excited Oxygen-Iodine Laser". *41st AIAA Plasmadynamics and Lasers Conference, Chicago, IL*, AIAA 2010-5039, Jul. 2010.

A.M. Roettgen, W.R. Lempert, and I.V. Adamovich "Measurements of N_2 Vibrational Distribution Function in Pulsed Nanosecond Nonequilibrium Discharge by Spontaneous Raman Scattering". *51st AIAA Aerospace Sciences Meeting, Grapevine, TX*, AIAA 2013-0576, Jan. 2013.

A.M. Roettgen, I. Shkurenkov, W.R. Lempert, and I.V. Adamovich "Thomson Scattering Studies in He and He-H_2 Nanosecond Pulse Nonequilibrium Plasmas". *SciTech 2014: 52nd AIAA Aerospace Sciences Meeting, National Harbor, MD*, AIAA 2014-1358, Jan. 2014.

A.M. Roettgen, I. Shkurenkov, W.R. Lempert, and I.V. Adamovich "Time-Resolved Electron Temperature and Number Density Measurements in a Nanosecond Pulse

Filament Discharge Using Thomson Scattering". *Aviation 2014: 45th AIAA Plasmadynamics and Lasers Conference, Atlanta, GA*, AIAA 2014-2113, Jun. 2014.

A.M. Roettgen, V. Petrishchev, W.R. Lempert, and I.V. Adamovich "Thomson Scattering Measurements of Electron Density and Electron Temperature in a Nanosecond Pulse Surface Discharge". *SciTech 2015: 53rd AIAA Aerospace Sciences Meeting, Kissimmee, FL*, AIAA 2015-1829, Jan. 2015.

Fields of Study

Major Field: Mechanical Engineering

Studies in:

Plasma Physics	Prof. Igor Adamovich
Optical Diagnostics	Prof. Walter Lempert

Table of Contents

List of Tables

List of Figures

Chapter 1: Introduction

Plasma is the fourth fundamental state of matter, and is most simply described as a quasi-neutral, electrically conductive, ionized gas, where the electrostatic effect of individually charged species is important on a spatial scale which is governed by the Debye radius,

$$\lambda_D = \left(\frac{\epsilon_0 k_B T_e}{e^2 n_e}\right)^{1/2} \cong 743 \left(\frac{T_e(eV)}{n_e(cm^{-3})}\right)^{1/2} (cm) \tag{1.1}$$

where n_e and T_e are the electron number density and electron temperature, respectively, k_B is the Boltzmann constant, e is electron charge and ϵ_0 is the permittivity of free space. In order for a quasi-neutral, ionized gas to be considered a plasma, the Debye radius must be much smaller than the characteristic spatial scale (L) (i.e. size of the discharge),

$$\lambda_D \ll L \tag{1.2}$$

A plasma can be created by adding energy to a gas, which can be achieved by either heating, bombarding it with high-energy ionizing particles (such as an electron, ion or neutron beam), irradiating it with high intensity light (optical breakdown), or applying an electric field. The last of these methods, which generates an electric discharge is the type of plasma that is the main focus of this work.

In electric discharges, most of the bulk plasma ionization is produced by electron impact processes, where high energy electrons collide with the neutral species in the gas (atoms and molecules), causing them to expel electrons and become ionized. These processes are discussed in greater detail in chapter 2, section 2.1.

The specific type of gas discharge plasma studied in this work is a plasma generated by high peak voltage, nanosecond duration pulses between two electrodes. These plasmas are generated by applying very short (≈1-100 ns), high voltage pulses (≈1-100 kV), each of which produces a high peak electric field between the electrodes. Short duration pulses provide two major advantages over DC, AC, radio frequency (RF), microwave (MW), or longer duration (μs or ms) pulsed discharges. First, they allow for significant amounts of energy to be coupled to the plasma over a short time, resulting in high specific energy loading. This provides a highly nonequilibrium environment, which allows studies of a wide range of nonequilibrium kinetic processes, including rotationally, vibrationally and electronically excited species production and decay, as well as kinetics of free radicals. These high electron energy plasmas have several applications that are being widely studied, including: plasma assisted combustion [1, 2, 3, 4], plasma flow control [3, 4, 5, 6, 7], electrically-excited laser development [8, 9], and biological and medical applications [10]. The second advantage of using short pulse duration to sustain these plasmas is their superior stability over longer duration pulses, which is a result of the electric field being removed before ionization instabilities have sufficient time to develop.

While these nonequilibrium plasmas have several applications, as listed above, they remain far from understood on a fundamental level. Characterizing nonequilibrium phenomena in nanosecond pulse discharge plasmas is important in obtaining

quantitative insight into the kinetic processes involved, which controls the energy requirements for sustaining these plasmas, as well as their effect on the flow-field, fuel-air chemistry, laser processes, and living cells and tissues. Characterization of these plasmas requires a synergy between experimental studies and plasma kinetic modeling. Kinetic modeling can provide insight into various energy transfer processes and chemical reactions, and determine their effect on the flow field and combustion kinetics. However, predictive capability of the models can only be assessed by their comparison with experimental data. This requires the experimental community to provide accurate, detailed measurements of excited species concentrations and/or distributions, as well as translational, rotational, vibrational and free electron temperature/energy information. The work presented in this dissertation focuses on free electron number density (n_e) and temperature (T_e) measurements, as well as N_2 vibrational distribution measurements.

Specific examples of the effect of N_2 and O_2 vibrational level populations on plasma chemistry include (i) nitric oxide (a regulated pollutant) formation in nonequilibrium gas discharge plasmas [11], and (ii) low-temperature air plasma lifetime [12]. In essence, N_2 vibrational excitation accelerates the rate of the following chemical reaction,

$$N_2(v) + O \rightarrow NO + N \tag{1.3}$$

while, O_2 vibrational excitation stimulates electron detachment from O_2^- ions,

$$O_2^- + O_2(v) \rightarrow O_2 + O_2^-(v) \rightarrow O_2 + O_2 + e^- \tag{1.4}$$

thereby decreasing the rate of electron density decay and increasing air plasma lifetime [12]. The rates of electron recombination and electron attachment processes

are also sensitive to electron temperature and electron energy distribution function (EEDF). Thus, the capability for simultaneous measurements of N_2 and O_2 vibrational level populations, as well as electron density (n_e), electron temperature (T_e) and EEDF is critical for predicting nonequilibrium molecular plasma power budget and plasma lifetime. In this dissertation, experimental studies of vibrational excitation and relaxation of N_2 in ns pulse discharges in nitrogen and air (chapter 3), as well as electron density, electron temperature and EEDF in ns pulse discharges in He, H_2-He and O_2-He (chapter 5) are presented and discussed.

Measuring the vibrational distribution function (i.e. excited vibrational level populations) of diatomic molecules, such as N_2 in the plasma requires the use of non-intrusive, laser diagnostic techniques. These include laser induced fluorescence (LIF), spontaneous emission spectroscopy, Coherent Anti-Stokes Raman Scattering (CARS), and spontaneous Raman scattering.

LIF is a widely used diagnostic technique for measuring species concentrations, which is known to be very sensitive. LIF utilizes resonant absorption that occurs between select electronic states in the species of interest. In order that these selective, resonant absorption transition wavelengths can be achieved, this technique is usually implemented with a tunable laser source, such as a dye laser. This presents a difficulty in accessing different species, since multiple dyes and/or laser sources are required, depending on the molecule being studied. Emission spectroscopy is a useful technique, but is limited in that it is a line-of-sight, integrated measurement, and also that it can only be used to study polar molecules, such as CO and NO.

CARS is another technique that can be used to measure vibrational loading of molecules [13, 14, 15]. This four-wave mixing spectroscopic technique is known for

producing high-resolution vibrational/rotational spectra of non-polar molecules which do not have emission spectra, such as H_2, N_2, O_2, etc. However, CARS has two main disadvantages. First, three input photons (usually from two different laser sources) are required. Furthermore, CARS sensitivity scales quadratically with quantum state number density difference, making it difficult to use at low pressures and in environments close to population inversion.

Spontaneous Raman scattering, on the other hand, requires only a single-wavelength laser source to generate a complete scattering spectrum, and furthermore, the signal varies linearly with quantum state number density. With this technique, peaks corresponding to ground vibrational states of different molecules of interest are generally separated by several nanometers or more, avoiding inter-species interference in mixed-gas environments, and even allowing for simultaneous measurements of multiple species. The primary weakness of any scattering technique, with Raman scattering being no exception, is its inherently weak signal intensity. This is generally satisfactorily circumvented by utilizing a high-peak power, short pulse duration laser, such as an Nd:YAG laser. The studies presented here involving N_2 vibrational distribution function measurements utilize the spontaneous Raman scattering technique, driven by a frequency doubled (532 nm) Nd:YAG laser. This is discussed in more detail in chapter 3.

Characterizing free electron behavior in a plasma requires measuring electron number density and electron temperature (as well as inferring the electron energy distribution from these measurements). This is usually achieved through the use of either a Langmuir probe [16, 17], microwave interferometry [18] or Thomson scattering

[19, 20]. While Langmuir probes are widely used for electron density and temperature measurements, as they provide a technique that can be utilized over a wide range of parameters, the probes themselves are known to be intrusive to the measurement region by causing small, but significant perturbations of the plasma region near the probe tip [21, 22]. Furthermore, interpretation of probe measurement results in high pressure plasmas requires the use of fairly complex theoretical models. Although it is possible to get temporally and spatially resolved electron density and electron temperature data from Langmuir probe measurements, more accurate results for both of these parameters can be achieved through the use of other techniques. Microwave interferometry is a useful technique, especially at high pressures, where Langmuir probes perform poorly due to the reduction of the electron mean free path relative to the Debye length (eq. 1.1). However, microwave interferometry does not provide a measure of the electron temperature, and with this technique it is difficult to achieve spatially resolved data on the electron density [23].

Thomson scattering (quasi-elastic scattering of light by free charged particles), as a laser diagnostic technique, provides a non-intrusive alternative to Langmuir probe measurements, which also retains the ability to measure electron temperature, unlike microwave interferometry. Furthermore, since the scattering light source used for Thomson scattering is a laser beam, which has both short pulse duration ($\approx$ 10 ns or less) and can be focused down to the spatial scale of hundreds of microns, this technique lends itself well to both temporally and spatially resolved measurements. As such, the Thomson scattering technique is utilized in the present work for the determination of electron number density and electron temperature, and is also used to infer the electron energy distribution. The primary weakness of Thomson scattering

is its extremely weak scattering intensity. Other issues include interference from other elastic scattering processes (such as Rayleigh and Mie scattering), plasma emission, and stray light. The implementation and results obtained using this technique in the present work are discussed in more detail in chapters 4 and 5.

In order to filter out the interference sources (such as Rayleigh and Mie scattering, and stray light), two techniques are commonly used: selective absorption [24] and spectral masking [19]. Selective absorption, usually through the use of atomic vapor filters is the most common solution. This technique utilizes a filtering device, filled with an atomic species, such as sodium, potassium, mercury or rubidium. The laser source is then tuned to a specific wavelength, such that the narrow-band absorption line of the atomic species used in the filter will suppress the spectrally narrow Rayleigh scattering signal, but not the spectrally broader Thomson signal. However, this technique requires a tunable laser source, such as a dye laser or Ti:Sapphire laser, as well as temperature control of a vapor filter filled with hazardous, difficult-to-handle chemicals. A simpler alternative is to use a spectral mask, which is placed within the spectrometer at an appropriate location so as to physically block a portion of the spectrum that needs to be suppressed. This latter technique is utilized in the present work.

In a brief overview, the experiments presented here use a custom-designed, triple-grating spectrometer, in conjunction with a stainless steel spectral mask, to filter out undesirable scattered and stray light, while ICCD (Intensified Charge Coupled Device) camera subtractive methods are used to remove background plasma emission. The triple-grating spectrometer developed for this experiment was designed based on a similar instrument used by a research group at Ruhr-University Bochum, in

Germany [19]. This device operates by using the first grating to diffract the light that initially enters the spectrometer into a spectrum. This spectrum is then sent through a spectral mask, which physically blocks the undesirable, relatively narrow-band quasi-elastic scattering signals (i.e. Rayleigh and Mie scattering), while allowing the majority of the relatively broadband Thomson scattering spectrum to continue to propagate through the spectrometer. The remaining Thomson spectrum is then incident on a second grating, which is set up subtractively. This re-compresses the spectrum back into an image, which is then sent through a slit (to block any remaining stray light) and is incident upon the third grating. The image is then re-dispersed into a spectrum before being collected by an ICCD camera for analysis. This instrument and its implementation are explained in further detail in chapter 4.

The triple-grating spectrometer is not only useful for measuring Thomson scattering signal, but also allows for the collection of pure rotational Raman scattering. Measuring Raman spectral intensity for a known rotational transition in a molecular gas mixture is important in inferring the absolute electron number density from the Thomson spectrum. This is discussed further in chapter 5, section 5.4.

This dissertation includes six chapters. In chapter 2, an overview of dominant kinetic processes in nonequilibrium, nanosecond pulse plasmas is given. This includes a brief discussion of charged species production (primarily via electron impact processes) and the energy partition in these plasmas. This is followed by an overview of N_2 vibrational kinetics that play a significant role in these plasmas, including the anharmonic V-V up-pumping process that can enhance the populations of high vibrational levels of molecules.

Chapter 3 presents the background, implementation and results of measurements of N_2 vibrational distributions obtained via spontaneous Raman scattering. First, a brief overview of general scattering theory is presented, followed by a discussion of Raman scattering, as it pertains to vibrational population measurements. Next, the spontaneous Raman scattering laser diagnostic apparatus used in the experiment is presented and discussed. Following this, the general characteristics of a nanosecond pulse discharge plasma, sustained between two spherical electrodes, used in these measurements are presented and analyzed. Next, the procedure for extracting the vibrational distribution function from the vibrational Raman spectrum is summarized. Then, a brief discussion of a 0-D kinetic model, which was used to model the N_2 vibrational distribution measurements in nitrogen, is provided. The chapter concludes with the presentation and discussion of the N_2 vibrational distribution measurement results obtained in both nitrogen and air plasmas.

Chapter 4 gives the necessary background and design information related to the triple-grating spectrometer. First, motivation for using this type of device is discussed. This is followed by a brief overview of Thomson scattering and a comparison between Thomson and Rayleigh scattering, highlighting the key differences that make the use of spectral masking feasible and effective. Finally, the design and implementation of the spectrometer itself is presented.

Chapter 5 presents Thomson scattering measurements of electron density, temperature, and energy distributions in both sphere-to-sphere and near-surface, nanosecond pulse discharges. First, an overview of the Thomson scattering experimental setup is presented. This is followed by a description of the fitting procedure used to infer the data from the raw Thomson spectra. Next, procedures for extraction of the electron

temperature and number density, as well as inference of the electron energy distribution function (EEDF) are discussed. Following this, the experimental conditions and characteristics for the nanosecond pulse, single-filament discharge, sustained between two spherical electrodes are given. This is followed by a brief overview of a 2-D kinetic model that was used to analyze a portion of the electron temperature and electron density results. Next, the single-filament discharge results (temperature, density and EEDF) are presented and analyzed. Finally, the near-surface discharge experimental conditions, and results obtained in this discharge, are similarly shown and discussed.

The dissertation concludes with Chapter 6, which summarizes the work that has been done and formulates the major conclusions. Suggestions for diagnostic improvements and future work to be pursued are also discussed.

Chapter 2: Nonequilibrium Plasma Kinetics Overview

This chapter will present an overview of kinetic processes in nanosecond pulse, electric discharges. First, an overview of production and decay of charged species (ions and electrons) in an electric discharge is discussed (section 2.1). Next, the energy loading to the plasma form the applied electric field, and the subsequent partition of the electron energy among various molecular energy modes is discussed (section 2.2). The chapter then concludes with a brief discussion of vibrational kinetics in harmonic and anharmonic oscillating diatomic gas mixtures (section 2.3).

2.1 Charged Particle Production

A gas may be considered a plasma when it becomes sufficiently ionized to be electrically conductive, is quasi-neutral, and the Debye radius is much shorter than the characteristic length scale (e.g. size of the discharge, see eq. 1.2). Important mechanisms and processes involved in the generation and decay of charged species in gas discharges are discussed in detail in the literature [25], and are only summarized here. When a plasma is generated via an applied electric field, as is the case for this work, the main source of ionization of the gas is direct electron impact. In most cases, this involves applying a high voltage between two electrodes in a gas, which can be produced by a DC, AC, radio frequency (RF), or pulsed high-voltage source. The

latter approach is used in the work presented in this dissertation. Regardless of the power source, ionization and breakdown are achieved primarily by electron impact. In many electric discharges sustained between two metal electrodes, an additional key process sustaining electric current between the electrodes during breakdown is secondary emission from the cathode, which is maintained by ion bombardment. This is discussed in further detail later in the section.

Electron impact ionization occurs by the following process. Free electrons are rapidly accelerated by the strong electric field toward the positively charged electrode. Along the way, some of these electrons collide with molecules in the gas. If the colliding electron is sufficiently accelerated by the field to be above the ionization energy of the collision partner (i.e. molecule or atom), a second electron is liberated, and an ion generated, from the collision molecule, which is then also accelerated by the field. This process continues, resulting in what is called an electron avalanche. Eventually, enough free electrons are present throughout the plasma volume such that it is electrically conductive (able to carry current). The moment at which this occurs is referred to as electrical breakdown.

The ionization coefficient, α, is used to characterize the rate of ionization in a gas discharge. It is defined as the number of ionization events produced by an electron over a 1 cm path along the electric field lines. The ionization coefficient is given as

$$\alpha = \nu_i / v_d \tag{2.1}$$

where ν_i is the ionization frequency [s^{-1}] and v_D is the electron drift velocity $\left[\frac{cm}{s}\right]$. Figure 2.1 shows values of α vs. E/p (Electric field over pressure; a form of the reduced electric field) for different gases.

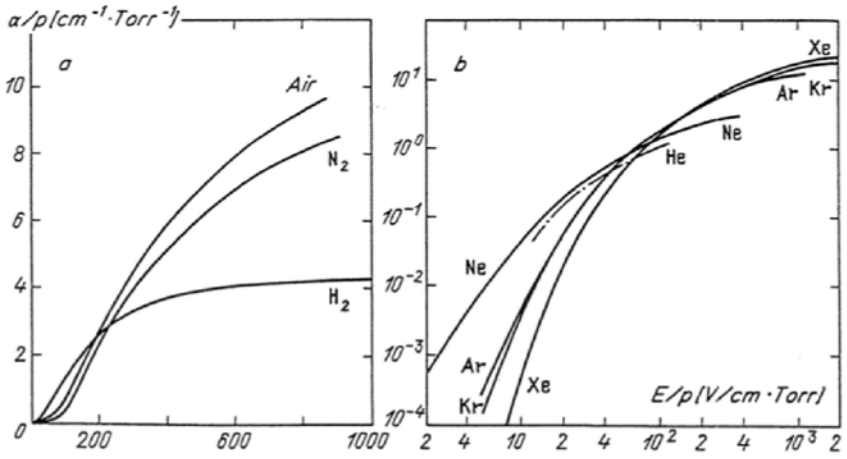

Figure 2.1: Ionization coefficients vs. reduced electric field for a large range of E/p values (E is the electric field, p is pressure) in molecular gases (left) and in inert gases (right). From reference [25].

Other, less prevalent, ionization processes in the plasma include photoionization, which is the ionization of an atom or molecule by interaction with a photon,

$$h\nu + A \rightarrow A^+ + e^- \tag{2.2}$$

ionization by electronically excited atoms,

$$A^* + A \rightarrow A + A^+ + e^- \tag{2.3}$$

and associative ionization,

$$A^* + A \rightarrow A_2^+ + e^- \tag{2.4}$$

Another critical process in the production of charged particles in gas discharges, and in gas breakdown dynamics, is secondary electron emission, which involves extracting free electrons from the metal in the electrode. The work function of the metal used in an electrode's material dictates how much energy is required to extract

an electron from the bulk of the material. The work function is given by

$$W = -e\phi - E_F \tag{2.5}$$

where e is electron charge, ϕ is the electrostatic potential and E_F is the electrochemical potential of the electrons in the material. When photons interact with the electrode material, electrons are released from the material due to the photoelectric effect, as governed by the work function. There are several mechanisms of secondary emission involving positive ions (cations), electronically excited atoms, electrons and photons. One of the most important mechanisms is secondary emission due to ion bombardment of the cathode. This process involves a cation accelerated toward the cathode surface by a strong electric field. When the cation reaches a distance from the surface which is comparable with its diameter, an electron from the electrode surface tunnels into the ion and neutralizes it. The excess energy gained from this process can then be used to expel a second, emission electron. This process plays a significant role in increasing the overall current of the discharge following breakdown, ultimately creating a self-sustained discharge, so long as a sufficiently strong electric field remains present. Other mechanisms, involving electronically excited atoms, electrons and photons can also result in secondary emission from the electrode surface. It is often difficult to determine the specific channel by which secondary emission is occuring. As such, a generalized secondary emission coefficient, γ, incorporating all of these complex processes is defined for a given material and gas. Figure 2.2 shows experimentally measured values for γ for select materials and gases. It should be noted that copper electrodes are used exclusively in the experiments presented in this work (chapters 3, 5).

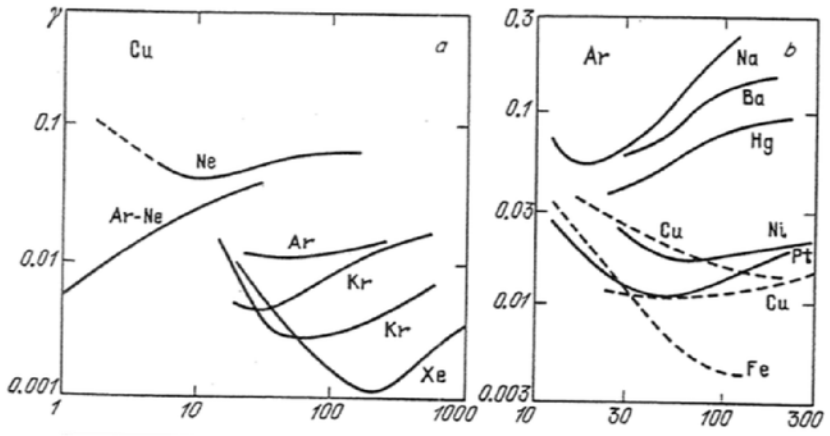

Figure 2.2: Experimentally determined effective secondary emission coefficients for copper in select gases (left) and select materials in argon (right). X-axis is E/P (reduced electric field). From reference [25].

Electron-ion recombination processes begin competing with impact and secondary emission when the electron/ion density in the plasma becomes sufficiently high, such that the rate of ionization ($\nu_i n_e = \alpha v_d n_e$) becomes comparable with the rate of recombination ($\nu_r n_e = \beta n_i n_e \approx \beta n_e^2$), where β is the recombination coefficient. However, in short pulse duration discharges, recombination may only gain a dominant foothold after the electric field is turned off (i.e. in the afterglow). Once this happens, recombination mechanisms begin to dominate the electron kinetics and the plasma begins to decay. Some of the major recombination processes are as follows. Dissociative recombination, the reverse process of associative ionization, is among the most rapid bulk recombination mechanisms,

$$A_2^+ + e^- \rightarrow A^* + A \tag{2.6}$$

Another process, radiative recombination,

$$A^+ + e^- \rightarrow A + h\nu \tag{2.7}$$

not only provides a mechanism for removing electrons, but also results in light emission. Three-body recombination,

$$A^+ + e^- + e^- \rightarrow A + e^- \tag{2.8}$$

is another important mechanism, but only at very low electron temperatures and/or at very high electron densities. Here, a free electron is captured by an ion, forming a highly excited atom. This excited atom is then deactivated, step-by-step by further electron impacts in a cascading effect until it reaches the lowest excited state level. The atom then emits a photon (radiative transmission) to complete de-excitation to the ground state. Three-body recombination with an atom or molecule acting as the third body is much less likely (typically by 7-8 orders of magnitude) compared to an electron, and only plays a significant role at very high pressures and/or in very low electron density plasmas. Lastly, ion-ion recombination is the dominant mechanism for recombination in gases with significant electron affinity, where negative ions, through electron attachment processes, have been formed (i.e. in electronegative gases). At low pressures (<10 torr), ion-ion recombination in two-body collisions, where excess energy results in an electronically excited atom, are important,

$$A^- + B^+ \rightarrow A + B^* \tag{2.9}$$

At moderate pressures, three-body collisions, where excess energy is removed by a third, neutral collision partner are more significant,

$$A^- + B^+ + C \rightarrow A + B + C \tag{2.10}$$

As is evident from the previous discussion, multiple mechanisms play a role in electron production and decay. In order to study these processes and develop kinetic

models for these mechanisms, obtaining accurate time-resolved experimental data for electron density, electron temperature and electron energy distribution in different gas mixtures is critical. These quantities are the focus of the Thomson scattering measurements presented in chapter 5. Ultimately, all of these values are controlled by one parameter, the reduced electric field strength (E/N). The importance of the reduced electric field can be seen through the following analysis. The energy gained by an electron between collisions is,

$$\epsilon = eE\lambda_{MFP} \tag{2.11}$$

where e is electron charge, E is the electric field, and λ_{MFP} is the mean free path length. The mean free path length is defined as,

$$\lambda_{MFP} = \frac{1}{N\sigma_{coll}} \tag{2.12}$$

where N is number density and σ_{coll} is the electron-neutral collision cross-section.

Combining equations 2.11 and 2.12, yields an equation for the average electron energy gained by an electron between collisions, which is dependent on reduced electric field (E/N),

$$\bar{\epsilon} = e\frac{1}{\sigma_{coll}}\frac{E}{N} \tag{2.13}$$

Equation 2.13 shows the dependence of electron temperature on reduced electric field (E/N) in the absence of collisional losses.

To understand why electron temperature is much greater than the translational/rotational temperature ($T_e \gg T$) in a nonequilibrium gas discharge, a brief discussion of the electron energy balance is required. The electron energy equation can be derived from the Boltzmann equation for electrons, or obtained using a simpler approach, and is

given as [25],

$$\frac{d\epsilon}{dt} = \left(\frac{e^2E^2}{m\nu_m^2} - \delta\epsilon\right)\nu_m \tag{2.14}$$

where δ is the average electron energy fraction lost per collision, which varies for elastic and inelastic collision dominated environments, and ν_m is the electron collision frequency. In equation 2.14, the first term represents energy gained by the electrons due to the applied electric field. The second term represents energy lost in collisions. In the second term, the δ coefficient incorporates all elastic and inelastic collisional losses to the electrons in a particular environment. In the limit of purely elastic collisions, $\delta \rightarrow 2m/M$. In atomic gas discharges, elastic collisions dominate under most circumstances, since ionization and electronic excitation thresholds are relatively high ($\epsilon_I \approx$10 eV). In molecular gas discharges, electron energy transfer to vibrational and rotational modes is very efficient, and inelastic collisions may become dominant (see figure 2.3). Inelastic losses to these modes are typically greater by up to two orders of magnitude compared to elastic losses ($\delta_{inelastic} \approx 10^{-3} - 10^{-2}$, $\delta_{elastic} = 2m/M \approx 10^{-4} - 10^{-5}$, [25]). It can be shown from the equation that the average electron energy has a linear dependence on reduced electric field (E/N) and a $\sqrt{\delta^{-1}}$ dependence, as follows,

$$\bar{\epsilon} = \frac{e}{\sigma_{coll}}\frac{E}{N}\frac{1}{\sqrt{\delta}} \tag{2.15}$$

Equation 2.15 shows the dependence of electron temperature on reduced electric field (E/N). Since $\delta \ll 1$, it can be seen that acceleration of the electrons by the strong electric field is far more efficient than collisional losses. As a result, as long as a sufficiently strong electric field is applied, electrons in a gas discharge gain energy more rapidly than they lose it due to collisions, which results in a much higher electron temperature compared to the gas itself (i.e. nonequilibrium conditions, $T_e \gg T$).

2.2 Energy Loading and Partition

In nanosecond pulse, electric discharges, the total energy loading to the plasma can be inferred from voltage and current probe measurements,

$$\epsilon_{total} = \int_0^\infty V(t)I(t)dt \tag{2.16}$$

However, the energy loading is not necessarily uniform across the plasma, since a significant fraction (up to ≈50% in nanosecond pulse discharges [26]) of the voltage fall between the electrodes occurs across the cathode layer, which is very small compared to the discharge gap ($L_{CL} \ll L$). As a result, the energy loading calculated from equation 2.16 is not indicative of the energy loading distribution in the plasma. To determine the local energy loading, the electron number density and electric field are required,

$$\epsilon_{local} = \int_0^\infty j\mathbf{E}dt \tag{2.17}$$

where j is the current density given by $j = en_e\mu_e\mathbf{E}$, where μ_e is the electron mobility. Since the electric field is related to the electron temperature (see eqn. 2.15), the latter can be measured instead of the electric field to yield the same information. As a result time-resolved measurements of n_e and Te are critical in understanding and predicting the plasma power budget. Furthermore, electron temperature and the electron energy distribution control how the electron energy is partitioned among different modes, as discussed in chapter 1.

Some electron collision processes which control how the electron energy is partitioned in gas discharge plasmas are discussed below. Electron impact dissociation of diatomic molecules plays a significant role when electrons in the discharge are sufficiently accelerated by the field, such that their energy exceeds the dissociation energy

of the molecule.

$$e^- + AB \rightarrow A + B + e^- \tag{2.18}$$

The dissociation energy threshold for most diatomic molecules is in the range of 2-12 eV. In the case of N_2, which is studied in this work (presented in chapter 3), the dissociation energy is approximately 10 eV. As a result, in N_2 containing plasmas, this process only becomes significant at fairly high electron energies.

Another important electron impact process, in electronegative gases, is electron attachment, which was alluded to in section 2.1. Attachment occurs mainly through two mechanisms: dissociative attachment,

$$e^- + AB \rightarrow A + B^- \tag{2.19}$$

and three-body attachment,

$$e^- + AB + M \rightarrow AB^- + M \tag{2.20}$$

For electronegative gases such as O_2, dissociative attachment requires electron energy of ≈4.2 eV, which is well within the energy range of electrons in gas discharges.

Another important electron collisional process which occurs is electronic excitation of molecules and atoms,

$$e^- + A_2 \rightarrow e^- + A_2^* \tag{2.21}$$

This process typically requires significant energy (up to several eV), though less than dissociation. For example, for N_2 (studied in this work; see chapter 3), excitation of electronic states requires electron energies of ≈6-11 eV.

Another electron impact process which can play a significant role in gas discharges in molecular gases is vibrational excitation. This process occurs in two steps,

$$e^- + AB(v = 0) \rightarrow AB^-(v^*) \tag{2.22}$$

$$AB^-(v^*) \rightarrow AB(w) + e^- \tag{2.23}$$

First, an electron is captured by the ground vibrational state molecule, causing it to become an unstable, excited negative ion (anion). Due to the instability of the anion, the electron is almost immediately expelled, leaving behind a vibrationally excited molecule and a free electron (of lower energy than prior to the collision). Vibrational excitation has a relatively large cross-section ($\sigma \approx 10^{-15}$ cm^{-2}) which is comparable to the total electron-molecule collision cross-section, and typically requires ≈1-3 eV of electron energy. Thus, it is a prevalent process in gas discharges sustained by moderately strong electric fields.

Figure 2.3 gives an illustration of the electron energy partition in DC electric discharges in air, including energy fractions going into the excitation of molecular vibrations, rotations, electronic excitation, ionization, and translational losses. As can be seen from the figure, N_2 rotations and O_2 vibrations and rotations are most prevalent at lower E/N values (E/N $<$ 10 Td). At moderate E/N (E/N ≈10-50 Td), N_2 vibrational excitation is the dominant channel of electron energy loss. See chapter 3 for studies of this phenomenon. At high E/N, electronic excitation becomes more important, and ionization becomes more prominent.

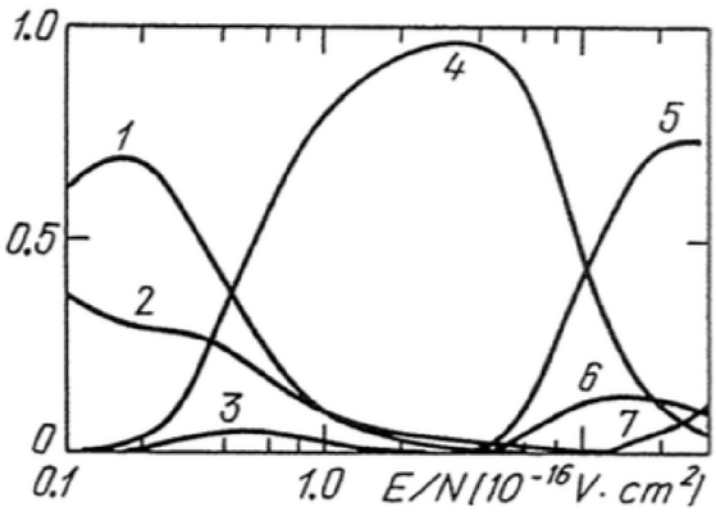

Figure 2.3: Fractions of energy transferred by electron impact processes in air to (1) O_2 vibrations, (2) O_2 rotations, (3) elastic (translational) losses, (4) N_2 vibrations, (5) N_2 electronic excitation, (6) O_2 electronic excitation, and (7) ionization of N_2 and O_2. From reference [25].

2.3 N_2 Vibrational Kinetics

As has been shown, vibrational excitation of diatomic molecules in a gas discharge plasma can occur due to electron impact (e-V energy transfer, see equations 2.22 and 2.23). In gas discharges, this is the dominant source of vibrational excitation, while relaxation (deactivation) proceeds mainly by the collisional exchange of vibrational quanta among the molecules (V-V energy exchange) and collisional energy transfer to translational/rotational degrees of freedom (V-T relaxation). Additional channels of vibrational deactivation include energy transfer from vibrational to electronic excitation (V-E transfer), which has been observed in CO e.g. $CO(X^1\Sigma, v \approx 40) + M \rightarrow CO(A^1\pi_1, v \approx 0) + M$ [27], and vibrationally stimulated chemical reactions (V-chemical) [11, 28], such as NO formation in vibrationally

nonequilibrium air plasmas,

$$N_2(X, v) + O \rightarrow NO + N \tag{2.24}$$

A Maxwell-Boltzmann vibrational distribution among the molecules is realized at equilibrium. From statistical mechanics, the generalized Maxwell-Boltzman distribution is given as,

$$\frac{N_i}{N} = \frac{g_i \exp\left[-\frac{\epsilon_i}{k_B T}\right]}{Z} \tag{2.25}$$

where N_i is the number density of molecules at energy level 'i', N is the total number density of molecules, g_i is the degeneracy of the energy level 'i', ϵ_i is the energy of quantum energy level 'i', k_B is the Boltzmann constant, T is the temperature, and Z is the partition function, given as,

$$Z = \sum g_i \exp\left[-\frac{\epsilon_i}{k_B T}\right] \tag{2.26}$$

In the case of a harmonic oscillator, the vibrational partition function becomes,

$$Z_{vib} = \frac{\exp\left[-\frac{\theta_{vib} v}{2T}\right]}{1 - \exp\left[-\frac{\theta_{vib}}{T}\right]} \tag{2.27}$$

where θ_{vib} is the characteristic vibrational temperature of the molecule (θ_{vib,N_2}=3395 K), and v is the vibrational quantum number, used to denote the vibrational energy levels,

$$\epsilon_v = \left(v + \frac{1}{2}\right) \theta_{vib} k_B \tag{2.28}$$

Thus, the harmonic oscillator vibrational energy distribution reduces to,

$$\frac{N_v}{N} = \left[1 - \exp\left(-\frac{\theta_{vib}}{T}\right)\right] \exp\left(-\frac{\theta_{vib} v}{T}\right) \tag{2.29}$$

In reality, diatomic molecules are not harmonic oscillators, but in fact exhibit weak anharmonicity. Although molecular anharmonicity is quite small (of the order of 1%), such that,

$$\epsilon_v = \omega_e \left(v + \frac{1}{2}\right) + \omega_e x_e \left(v + \frac{1}{2}\right)^2 + ... \tag{2.30}$$

where $x_{e,N_e} = 6.2 \cdot 10^{-3}$, it has a very strong effect on vibrational distribution function at the conditions when the rate coefficients of V-V exchange greatly exceed the V-T rate coefficients. In this case, the anharmonic vibrational up-pumping process [29], which results from unequal energy spacing between vibrational levels in anharmonic oscillators, overpopulates higher vibrational levels through V-V exchange. To illustrate this process, consider the following V-V exchange process between two vibrationally excited molecules, at vibrational levels v and w, where $v < w$,

$$AB(v) + AB(w) \underset{k_r}{\overset{k_f}{\rightleftarrows}} AB(v-1) + AB(w+1) \tag{2.31}$$

The companion energy level diagram is given in figure 2.4.

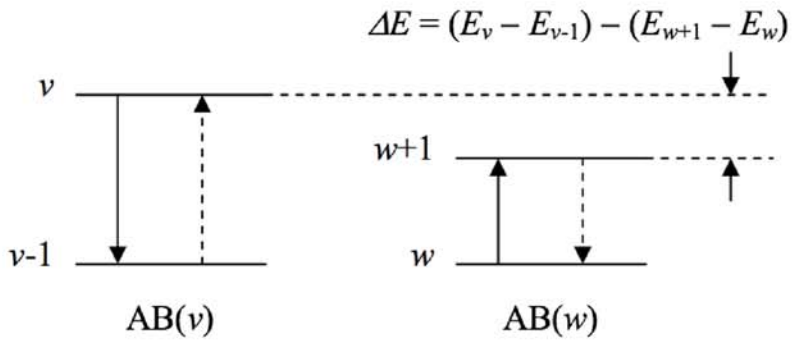

Figure 2.4: V-V exchange energy level diagram for an anharmonic oscillator ($v < w$). From reference [24].

Here, ΔE represents the vibrational energy defect which is transferred to/from translational and rotational degrees of freedom in the exchange process. At equilibrium, the forward and reverse rate coefficients of this process are related as follows,

$$\frac{k_f}{k_r} = \frac{1}{\exp\left[-\frac{\Delta E}{k_B T}\right]} \tag{2.32}$$

Since ΔE is positive (see figure 2.4), the forward process has a higher rate coefficient than the reverse process. This indicates, assuming the absence of any other significant processes (such as V-T relaxation or spontaneous radiative decay), that higher vibrational levels will become overpopulated via the V-V exchange process. This effect is enhanced at lower temperatures. It can be rigorously shown that at steady-state, in the absence of other processes (i.e. at the conditions of conservation of vibrational quanta), this effect results in a Treanor distribution [30] (see solid curve in figure 2.5),

$$f_v = f_0 \cdot \exp\left[-\frac{\epsilon_i v}{k_B T_{V01}} + \frac{x_e v(v-1)}{k_B T}\right] \tag{2.33}$$

where v is the vibrational quantum number, x_e is the absolute anharmonicity (i.e. the energy defect between vibrational levels), T is the temperature and T_{V01} is the 'first-level' vibrational temperature, given as,

$$T_{V01} = \frac{\omega_e(1-2x_e)}{ln\left(\frac{f_0}{f_1}\right)} \tag{2.34}$$

Note that the second term in the exponent of equation 2.33 disappears in the case of harmonic oscillators as $x_e \to 0$.

Since for many diatomic molecules, such as N_2, O_2, CO, NO, H_2, etc., V-T rate coefficients among low vibrational levels are much lower compared to V-V energy

transfer rates [31, 32], anharmonic up-pumping becomes the dominant effect controlling vibrational level populations among low levels. At high vibrational levels, rates of vibration to translation/rotation (V-T) relaxation processes increase considerably with vibrational quantum number. This is due to the reduction of vibrational energy level spacing with the quantum number. As a result, V-T relaxation becomes dominant at high vibrational quantum numbers such that the ascending branch of the distribution is not observed at steady state. An example of a vibrational distribution in a CO-N_2-He glow discharge is shown in figure 2.5 [33]. It can be observed that the vibrational distribution follows a Treanor distribution closely for vibrational populations at low energy levels ($v < 6$), while at high energy levels ($v > 35$), V-T relaxation begins to dominate such that vibrational level populations are reduced rapidly.

Vibrational kinetics of nitrogen plasma, which has been studied in this work (results are presented in chapter 3) is similar to that of CO, since V-T relaxation rates in both CO and N_2 are very low compared to V-V rates [31, 32]. As a result, the vibrational energy distributions in nonequilibrium conditions are qualitatively similar. The highest N_2 vibrational level observed in this work is v=12, which is still relatively low. Therefore, vibrational level populations in nitrogen and air, measured in the present work, do not exhibit a well pronounced V-V pumped plateau, such as has been measured in CO [33].

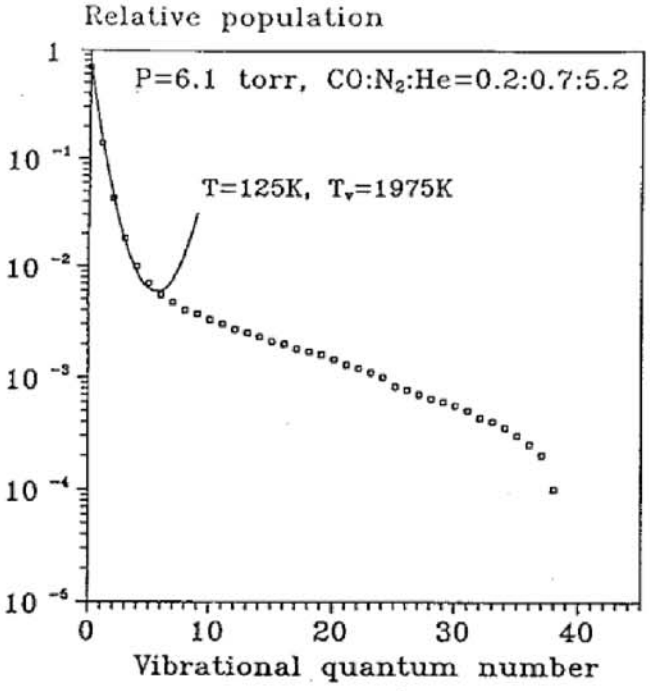

Figure 2.5: Measured CO vibrational distribution function (points) and Treanor distribution (curve) in a CO-N_2-He glow discharge, showing effect of V-V up-pumping and V-T energy transfer. From reference [33].

Chapter 3: Measurements of Vibrational Distribution Function of N_2 by Spontaneous Raman Scattering

This chapter details the spontaneous Raman scattering study of time-resolved N_2 vibrational distribution in nitrogen and air, generated in a nanosecond pulse discharge sustained between two spherical electrodes. The chapter begins with a brief background of the theory of light scattering (section 3.1), and Raman scattering in particular (section 3.2). This is followed by a discussion of the spontaneous Raman scattering laser diagnostic setup used in the experiment (section 3.3). Then, a summary of the characteristics of the sphere-to-sphere, nanosecond pulse discharge used for this experiment is given (section 3.4). Next, an outline of the data reduction procedure used to extract N_2 vibrational distribution functions (VDFs) (i.e. vibrational level populations), 'first-level' N_2 vibrational temperature and the average number of vibrational quanta per N_2 molecule is provided (section 3.5). This is followed by a brief outline of a 0-D kinetic model used to analyze the experimental data in nitrogen (section 3.6). Finally, the experimental results, including N_2 VDFs, 'first-level' vibrational temperature, and average number of vibrational quanta per N_2 molecule are presented for studies in nitrogen (compared with 0-D kinetic modeling results) and air (section 3.7).

3.1 Scattering Theory Overview

When light impinges upon a particle (atom, molecule, free electron or ion), the electric field of the incident electromagnetic wave induces an oscillating polarization, or dipole, of the bound or free electrons. The scattering particle is then in a virtual excited state, which is a linear combination of time-independent quantum states, resulting from the perturbation of the particle by the incident electric field. The scattering particle does not reside in the virtual state for any measurable amount of time, but quickly releases the energy it has just gained through radiation (i.e. emission of a photon). This near-instantaneous process is known as light scattering. When the scattering particle is a free electron, or if the atom, molecule, or ion of interest is in its ground electronic state, and is not rotationally or vibrationally excited, then, due to energy conservation, the emitted photon wavelength is nearly identical to that of the incident light. In this case, the only shift in the emitted photon wavelength occurs due to translations of motion of the particle (Doppler effect), which is very minor. This situation, where the energy difference between the incident and scattered photons is very small, is known as quasi-elastic scattering. In the case of atoms and molecules, this is called Rayleigh scattering. In the case of scattering by free charged particles (i.e. electrons and ions), this is called Thomson scattering. On the other hand, when molecules are rotationally and/or vibrationally excited, energy exchange between the rotational and/or vibrational modes of the molecule and the incident photon occurs, resulting in a scattered photon which is shifted in wavelength by an amount based on the level of rotational and/or vibrational excitation (Raman shift). This is called Raman scattering and is discussed in more detail in section 3.2.

Though molecules involved in the scattering process radiate light in all directions, the photon emission is not wholly isotropic. Rather, directional scattering probability is a function of the direction of incident radiation (light impingement) and number density fluctuations within the scattering volume. The scattered light field at any given time is the superposition of all of the electric fields radiated from each of the dipoles in the scattering volume. As a result, density fluctuations depend on the position of the dipoles. Since the particles, atoms and molecules in the scattering volume are constantly translating, and often rotating and vibrating as well, due to collisions, the positions of the dipoles are constantly changing, resulting in fluctuations in the scattered electric field. These fluctuations can be described by time-corellation functions, which can be inferred from bulk macroscopic properties of the gas or plasma.

Fluctuation scattering theory states that if the dielectric constant in the scattering medium has a uniform spatial distribution, the only direction in which net scattering will occur is the forward direction; scattering in all other directions will cancel out. However, kinetic theory states that the dielectric constant is dependent on both position and orientation of the particles in the medium, and since these are constantly translating and rotating (if the temperature is above absolute zero), the dielectric constant fluctuates as well, and thus net scattering occurs in non-forward directions. Whether any particular non-forward scattering direction is preferential depends on the polarizability tensor within the scattering volume, as well as the polarization and direction of the incident radiation. Typically, the light source used in scattering experiments is a solid-state laser, which provides a very narrow-band, uni-directional, coherent, polarized beam of light. While the strongest intensity of scattered radiation is in the forward direction, it is difficult to collect experimentally

since the light which passes through the scattering medium is much stronger than the scattered light, and thus drastically interferes with the measurements. Fortunately, due to the fluctuations in the local dielectric constant, a secondary, more experimentally suitable scattering angle, at which the maximum intensity of scattered light may be collected without interference from the unperturbed laser light, can be found, though choice of scattering angle in an experiment is often subject to the practical physical layout of the experiment (see figure 4.1 in section 4.2).

3.2 Raman Scattering

Raman scattering is the inelastic scattering of light from neutral molecules. There are three main types of Raman scattering: rotational Raman, vibrational Raman, and electronic Raman scattering. Each of these processes results in a scattered photon which is frequency shifted based on the energy associated with the rotational, vibrational, or electronic level of the scattering molecule, respectively. It is important to note that vibrationally excited molecules can be in different rotational states, resulting in ro-vibrational Raman scattering. Similarly, electronically excited molecules can be simultaneously vibrationally and rotationally excited, resulting in vibronic Raman or ro-vibronic Raman scattering, respectively. Regardless of this, since molecular energy levels are quantized, the frequencies of scattered photons in molecular gases are also discrete, and contain information about the internal energy levels of the molecule. Both spatially and time-resolved aspects of this information can be accessed through the use of laser Raman spectroscopy (see section 3.3).

Two types of Raman shift can occur when a photon is scattered by an excited molecule. If the scattered (radiated) photon loses energy (longer wavelength) and

the molecule gains the energy difference, it is called a Stokes shift and pertains to Stokes Raman scattering. The reverse case, where the scattered photon gains energy (shorter wavelength) and the molecule loses the energy difference, is called an anti-Stokes shift and pertains to anti-Stokes Raman scattering. It is important to note that anti-Stokes Raman scattering can only occur if the initial state of the scattering particle is excited. Figure 3.1 shows the corresponding energy level diagrams for these two processes, along with Rayleigh (quasi-elastic) scattering.

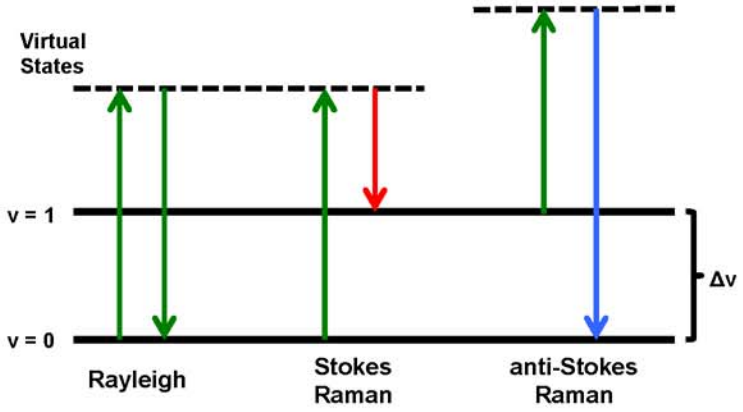

Figure 3.1: Energy level diagram for Rayleigh scattering, and Stokes and anti-Stokes Raman scattering.

Raman scattering theory is detailed in many textbooks and publications [24, 34, 35], and will only be outlined here. Raman scattering can be explained semiclassically (i.e. utilizing both classical and quantum mechanical arguments) as follows. The interaction between a harmonic oscillator and the incident electric field is governed by the dipole moment p,

$$\mathbf{p} = \alpha \mathbf{E} \tag{3.1}$$

where **E** is the electric field. As can be seen, the dipole moment is, in turn, controlled by the polarizability of the oscillator, α. Polarizability can be defined as the ability of an electron cloud to attain an electric dipole moment in response to an electric field. Applying a first-order (linear) expansion about a normal coordinate (r) in the vibrational mode of a harmonic oscillator, the polarizability is given as,

$$\alpha = \alpha_0 + \left(\frac{\delta\alpha}{\delta r}\right)_0 r \tag{3.2}$$

where the normal coordinate, with a natural frequency ν_v, is given as,

$$r = r_0 cos(2\pi\nu_v t) \tag{3.3}$$

Furthermore, the electric field, with a frequency ν_0, is

$$\mathbf{E} = \mathbf{E}_0 cos(2\pi\nu_0 t) \tag{3.4}$$

The dipole moment, induced by the electric field, then becomes,

$$\mathbf{p} = \alpha_0 \mathbf{E}_0 cos(2\pi\nu_0 t) + \left(\frac{\delta\alpha}{\delta r}\right)_0 \frac{r_0 \mathbf{E}_0}{2} \left[cos(2\pi(\nu_0 - \nu_v)t) + cos(2\pi(\nu_0 + \nu_v)t)\right] \tag{3.5}$$

The first term in equation 3.5 indicates a dipole oscillation at the incident electric field frequency and therefore represents Rayleigh scattering. The second term has a frequency shift which corresponds to a lower frequency relative to the incident field $(\nu_0 - \nu_v)$, representing Stokes scattering, while the third term has a frequency which is higher than the incident field $(\nu_0 + \nu_v)$, and corresponds to anti-Stokes scattering. See figure 3.1 for the energy level diagram of each of these processes.

It can be seen from equation 3.5 that Raman scattering will only occur when there is a perturbation in the normal coordinate, i.e. an oscillation (ν_v) in the polarizability of the molecule. For rotational Raman scattering to occur, the molecular

polarizability must vary when the molecule rotates. Vibrational Raman scattering, on the other hand, requires the polarizability to vary as the molecule vibrates. Note that this does not require a permanent dipole moment, as in infrared absorption or emission spectroscopy. Homonuclear diatomics, such as N_2 and O_2 are good examples of this (see sections 3.5, 3.7).

Since Raman scattering is governed by quantum energy level transitions, probabilities for scattering transitions are governed by selection rules. The selection rule for pure rotational Raman scattering of linear molecules is given by

$$\Delta J = 0, \pm 2 \tag{3.6}$$

where $\Delta J = 0$ corresponds to Rayleigh scattering, while $\Delta J = -2$ and $\Delta J = 2$ correspond to Stokes and anti-Stokes Raman scattering, respectively. For vibrational Raman scattering of harmonic oscillators, the selection rules are

$$\Delta v = \pm 1, \Delta J = 0, \pm 2 \tag{3.7}$$

Here, $\Delta J = -2, 0, +2$ represent O, Q and S rotational branches about the ground state vibrational level (v=0), respectively. $\Delta v = \pm 2, \pm 3, etc.$ are called overtone transitions, which are allowed for anharmonic oscillators, but are very weak in intensity and typically do not come into play in spectroscopic experiments.

3.3 Spontaneous Raman Laser Diagnostic

The spontaneous Raman scattering experiment, used to infer N_2 vibrational distribution function in nitrogen and air, utilizes a 1.75 meter long glass test cell, with copper, spherically tipped electrodes placed in the center of the cell. Figure 3.2 shows

a photograph of the cell, with an inset (in the upper-left corner) showing the electrode setup. The cell has Brewster angle, fused silica windows for optical access of an Nd:YAG laser. The extended length of the cell allows for a high pulse energy laser beam to enter the cell without damaging the windows by using a long focal length lens, thus allowing the laser beam diameter to remain relatively large (and thus the incident power density on the windows to remain low) upon entering the cell, before continuing to focus down to the center of the cell where the plasma is generated between the electrodes. Furthermore, by having the entrance windows at Brewster's angle, and using a linearly polarized laser source, reflected/stray light production is minimized.

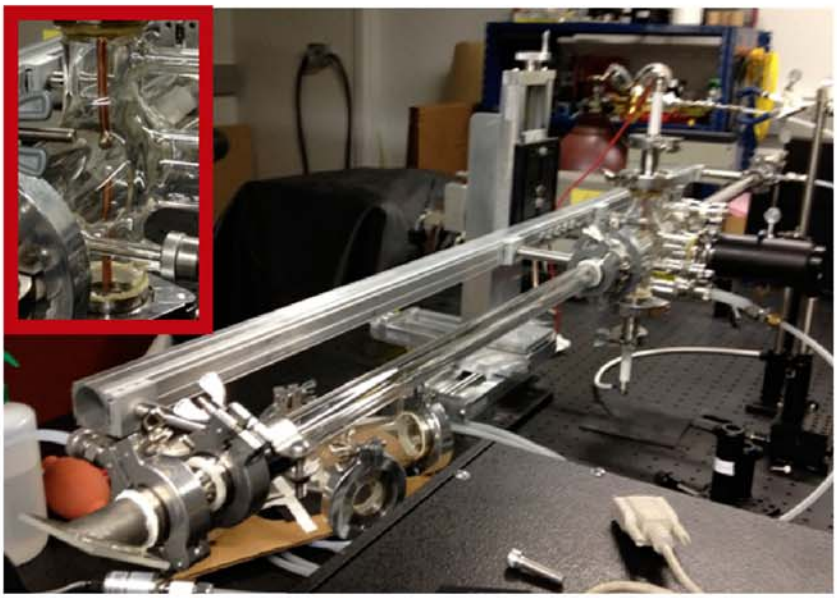

Figure 3.2: Photograph of the electric discharge cell with inset showing copper, spherically tipped electrodes. From reference [36].

An MKS mass flow controller is used to deliver gas flow to the cell. The gas flow direction is opposite to the laser beam direction. The total flow rate is controlled by the mass flow controller. The flow from the cell exhausts from the opposite end of the cell to a vacuum pump system. The pressure in the cell is controlled by a ball valve located in the exhaust line leading to a vacuum pump, effectively controlling pumping capacity. Total pressure in the cell is monitored just below the discharge in the center of the cell by an Omega digital pressure gauge. Gases used in this experiment are 99.998% pure N_2 and vehicle emission zero air (with very low hydrocarbon content), at a pressure of 100 torr.

The discharge is sustained between two copper spherical electrodes (D=7.5 mm, 1 cm gap). The electrodes are powered by a custom-built, magnetic compression, nanosecond pulsed, high voltage power supply. This device is capable of producing pulses of ≈18 kV peak voltage of ≈125 ns duration, at repetition rates up to 10 kHz. The output voltage of the pulser is controlled by input from a DC voltage supply. Pulse duration is approximately constant (125 ns), while pulse repetition rate is controlled by the frequency of an input trigger square wave (min. amplitude of 2 V and 1 μs duration). In the present study, a repetition rate of 60 Hz is used, at peak voltages of 10 kV (in nitrogen) and 9 kV (in air), producing a stable, diffuse, single filament discharge (see figure 3.6). The total flow rate used in the spontaneous Raman scattering experiments was 1.1 slm, which corresponds to a flow velocity of .07 m/s through the cell, which is sufficient to refresh the gas flow between successive laser pulses (30 Hz).

Figure 3.3 shows a schematic diagram of the entire spontaneous Raman scattering experimental setup. The system begins with a frequency doubled (532 nm), Nd:YAG

laser (30 Hz, 10 ns FWHM), which serves as the pump source for the scattering. The output energy of the laser is ≈425 mJ/pulse, with a FWHM of 10 ns. The Gaussian, ≈1 cm diameter beam is redirected with 532 nm, high-reflective coated one inch mirrors into a 2-inch diameter, 950 mm focal length, plano-convex lens. The beam then enters the glass test cell through the front, fused silica Brewster-angle window, and is focused down until it reaches the center of the cell. The focal point (with a calculated ≈60 μm diameter beam waist) is achieved at a point in the center of the plasma filament, midway between the top and bottom electrodes. The entire glass test cell is mounted onto a three-axis translation stage to allow for accurate adjustment of the focal point position (see figure 3.2). The unscattered portion of the beam exits the test cell through a second, rear Brewster-angle window and is subsequently directed to a beam dump.

The scattered light is collected from an ≈2.75 mm long section (see figure 3.8) of the laser beam at 90^o from the laser propagation direction, via a 2-inch BK-7 window (centered at the electrodes) and a subsequent 2-inch collection lens, which collimates the collected scattered light. This signal is then sent to an image rotator (made of 3 silver-protected, 2-inch mirrors), which rotates the initally vertically polarized, horizontal image to a horizontally polarized, vertical image. The image is then redirected and focused onto the vertical entrance slit of a 0.5-meter Acton spectrometer via an f-number matched plano-convex lens (f/6.5). The spectrometer has a three-grating turret setup, of which the 1800 groove/mm grating was used in this work. The grating angle is chosen through the spectrometer software such that the spectral range from 594 nm to 608 nm (607.1 nm is $v = 0$ for N_2) will be accesible to the detector. After the image is dispersed by the grating, the subsequent spectrum is collected

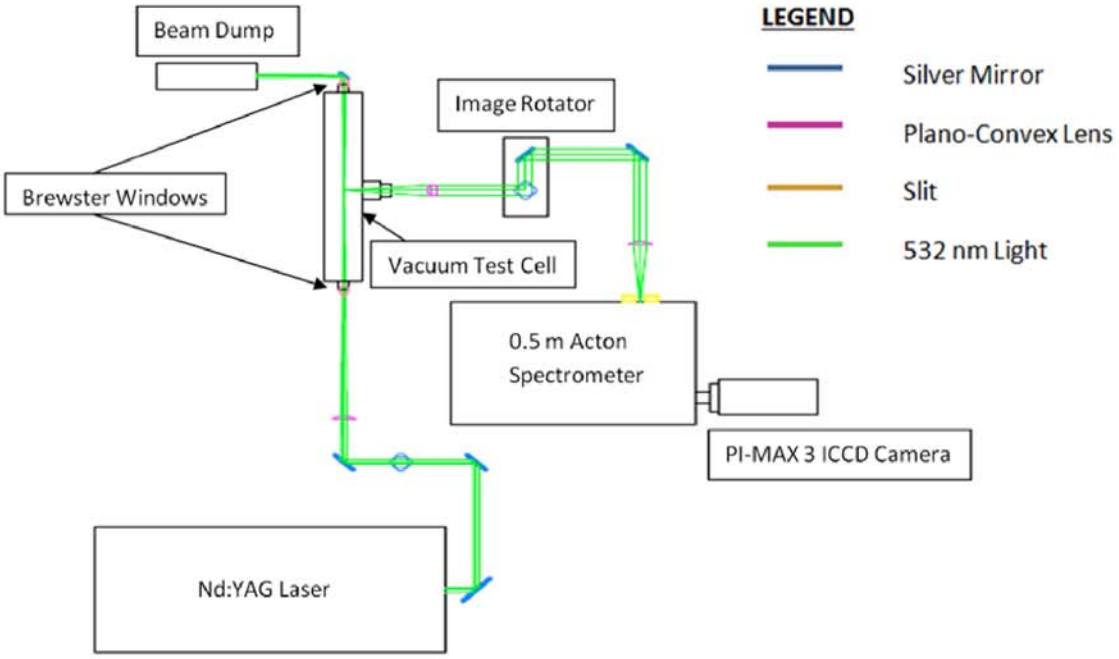

Figure 3.3: Spontaneous Raman Scattering Diagnostic Setup. From reference [36].

by a Princeton Instruments PI-MAX 3 ICCD camera. The linear dispersion for this diagnostic setup is ≈1.2 mm/nm.

3.4 Sphere-to-Sphere Nanosecond Pulse Discharge Characteristics

Figure 3.4 shows the voltage, current and coupled energy waveforms for the discharge in nitrogen. The reference point in time is the beginning of the main current pulse (t=0). The peak voltage is ≈10 kV. Peak current is ≈55 A, and is achieved approximately 70 ns after the start of the pulse. Pulse duration is ≈125 ns. An important feature of these waveforms is the presence of a second (lower amplitude) pulse, starting approximately 600 ns after the beginning of the primary pulse. This is a feature of the high-voltage pulser, and is consistently reproducible. As a result of this 'secondary' pulse, a small amount of additional energy is coupled to the plasma 600-700 ns after the primary pulse. This effect will be apparent in the data discussed in section 3.7. Total energy coupled to the discharge is ≈19 mJ/pulse, with 17 mJ coupled by the primary pulse, and 2 mJ coupled by the secondary pulse.

Figure 3.5 shows the voltage, current and coupled energy waveforms in the nanosecond pulse discharge in air. Peak voltage is ≈9 kV, while peak current is ≈45 A. The total coupled energy in this case is ≈14 mJ/pulse, with 12.5 mJ coupled during the primary pulse and 1.5 mJ during the secondary pulse.

Figure 3.6 shows single-shot ICCD images for the primary pulse of the discharge in nitrogen and air. Each pulse produces a single, diffuse filament, approximately 2.5 mm in diameter in nitrogen, and 2 mm in diameter in air. These filaments are both stable and consistent, providing a high specific energy loading plasma environment, suitable for measurements of vibrational level populations in nitrogen and air.

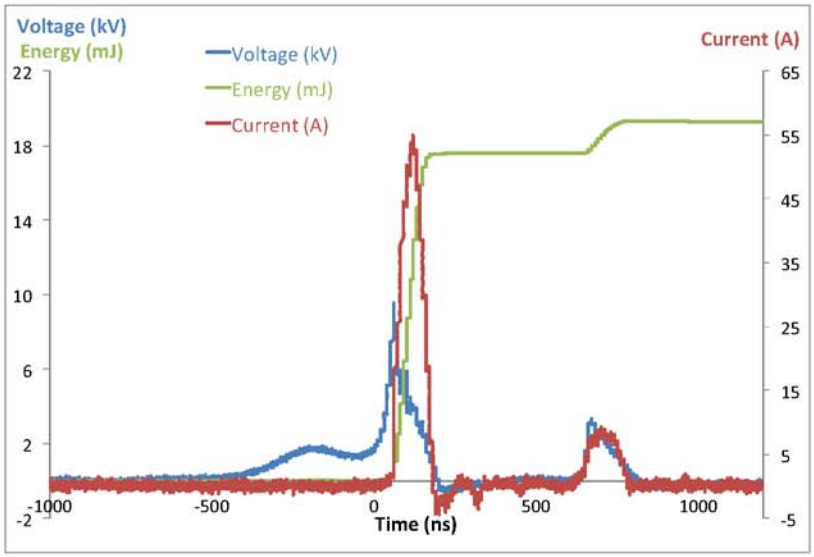

Figure 3.4: Voltage, current, and coupled energy waveforms in sphere-to-sphere discharge in nitrogen (P=100 torr).

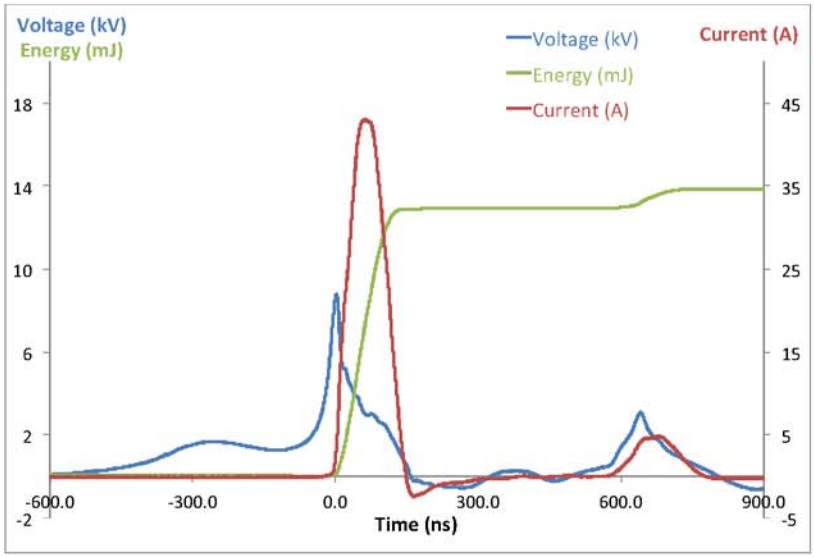

Figure 3.5: Voltage, current, and coupled energy waveforms in sphere-to-sphere discharge in air (P=100 torr).

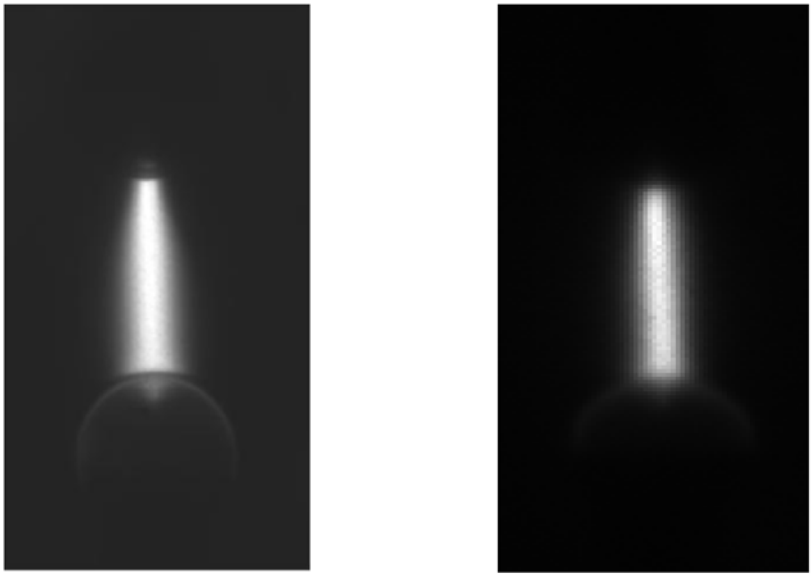

Figure 3.6: Broadband plasma emission (P=100 torr, 125 ns camera gate, single-shot) in sphere-to-sphere discharges in N_2 (left) and air (right).

3.5 Vibrational Distribution Function Inference

Figure 3.7 shows a typical spontaneous Raman spectrum obtained in a nanosecond pulse discharge in nitrogen. This spectrum is collected through a two-stage signal collection process with additional background subtraction: first, a large number of individual laser shots are collected on the ICCD camera chip, creating a single 'exposure'; next, several of these exposures are collected in succession and then averaged. Both processes increase the signal-to-noise ratio (S/N), with the former increasing it linearly with number of laser shots accumulated and the latter increasing it by the square-root of the number of exposures. Ultimately, a balance between S/N and reasonable signal collection time needs to be formed. For the present experiments, the number of laser shots accumulated per exposure varied between 2,500-24,000 for

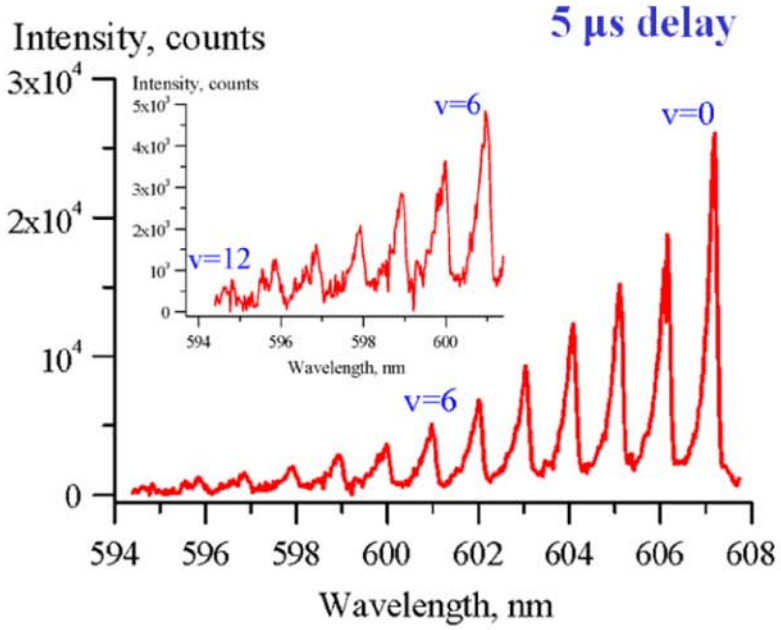

Figure 3.7: Typical spontaneous Raman spectrum in a nanosecond pulse discharge in N_2 (P=100 torr, 5 μsec after start of the current pulse). From reference [36].

the nitrogen plasma and between 9,000-22,000 for the air plasma, and was chosen individually for each data set (i.e. delay time after the pulse) to maximize S/N without saturating the ICCD detector. The number of exposures averaged varied between 5-16, and was chosen for each data set as a trade-off between further S/N improvement and overall signal collection time. Data sets (i.e. spectra) were collected for the range of 135 ns-10 ms after the start of the primary discharge current pulse (for nitrogen) and 200 ns-5 ms (for air). The camera gate used for the spectra collections in nitrogen was 6 ns for delay times below 1 μs and 30 ns for longer delays. The shorter gate was used at earlier delay times in order to discriminate background plasma emission,

Table 3.1: N_2 Vibrational Raman Scattering Spectra Collection Conditions.

Gas	Laser Shots per Exposure	Accumulation Time per Exposure (min.)	No. of Averaged Exposures	Camera Gate (ns)	Time Delay Range
99.998% Pure N_2	2,500 - 24,000	1.4 - 13.3	12 - 16	6, 30	135 ns-10 ms
Vehicle Emission Zero Air	9,000 - 22,000	5.0 - 12.2	5 - 6	45	200 ns-5 ms

which is very intense during and shortly after the discharge pulse; especially in nitrogen. In air, a camera gate of 45 ns was used for all data sets. Table 3.1 summarizes the spontaneous Raman spectra collection conditions used in nitrogen and air.

In addition to the procedure outlined above, a plasma background emission spectrum was taken for each data set (using the same collection conditions as the corresponding Raman spectrum) with the laser turned off (i.e. without scattering) and subtracted from the respective Raman spectrum. This gives a vibrational Raman spectrum such as the one shown in figure 3.7. As can be seen, vibrational levels up to $v = 12$ were detected.

As discussed previously (see section 3.3), the Raman scattering signal was collected from a 2.75 mm long, 60 μm diameter, roughly cylindrical probe volume, centered midway between the electrodes. ICCD camera chip pixels corresponding to the length of the measurement volume were 'binned together' prior to the readout of the spectrum. Thus, all of the data collected are inherently spatially averaged over this volume. Figure 3.8 shows a radial distribution of broadband plasma emission

intensity from the discharge filament in nitrogen, with a full width at half maximum (FWHM) of ≈2.3 mm. The signal collection region, corresponding to a 2.75 mm length, is also shown in the diagram.

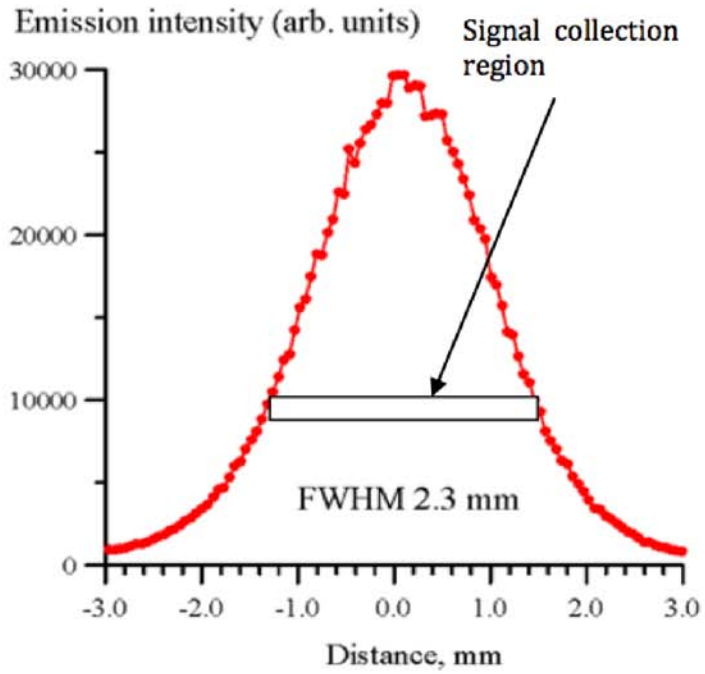

Figure 3.8: Discharge filament emission intensity distribution in N_2 with depiction of 2.75 mm long signal collection region (P=100 torr, camera gate=125 ns). From reference [36].

The following procedure for fitting the raw Raman spectra, and subsequently inferring the vibrational distribution functions (VDFs), assumes that the Raman scattering cross-section scales as $v + 1$, which is accurate for harmonic oscillators. This is not entirely accurate, however the effect of anharmonicity on the cross-section is small, even for levels as high as $v = 12$ [37], justifying this approach.

Returning to figure 3.7, it is notable that although the rotational structure of vibrational bands due to individual ro-vibrational transitions is not resolved by the present diagnostic, asymmetry within the vibrational bands can be observed as a result of the shape of the rotational line envelope. This asymmetry is taken into account by fitting each vibrational band in the spectrum by a superposition of Gaussian lineshapes, spectrally centered at each ro-vibrational transition wavelength. Since the degree of asymmetry varies for each vibrational band, the number of Gaussian lineshapes used was determined on a 'best least-squares fit' basis. Figure 3.9 shows a sample, Gaussian lineshape fitted spectrum taken 100 μs after the start of the main current pulse in nitrogen. It can be seen that, especially lower vibrational levels, the vibrational bands are not fully resolved, and some overlap occurs in the fitting, which introduces some uncertainty into the vibrational level populations inferred from the integrated intensities of these bands. This is discussed in further detail shortly.

After the synthetic spectrum has been generated, the area under each vibrational band is numerically integrated and divided by $v+1$, to account for the scaling of the Raman cross-sections used. These scaled intensities are then summed and normalized to 1, yielding the relative populations of each vibrational level, or the vibrational distribution function (VDF),

$$f_v = \frac{N_v}{N} \tag{3.8}$$

where N_v represents the absolute population of level v, and N is the total N_2 number density.

The uncertainty in the N_2 VDFs (i.e. relative populations of vibrational levels) arising from uncertainty of the integrated intensities of the vibrational bands in the

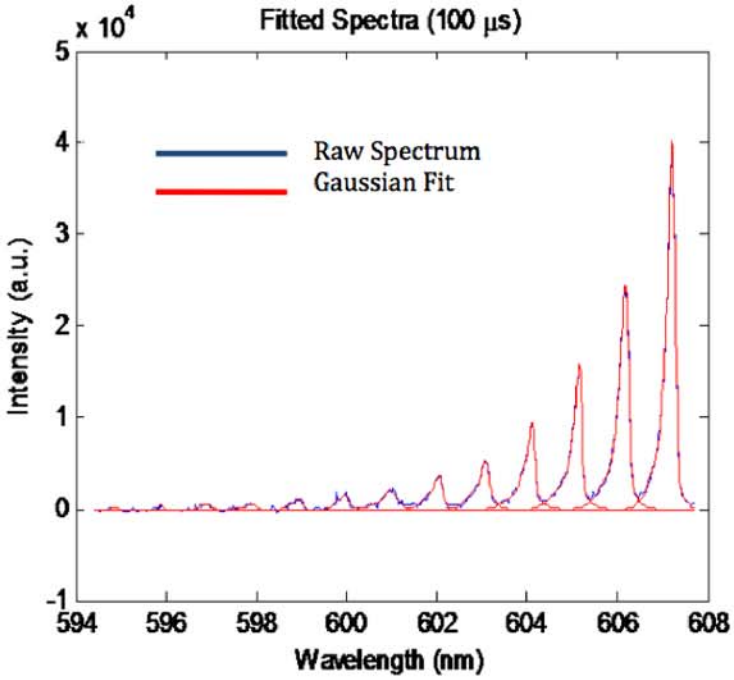

Figure 3.9: Sample spontaneous Raman spectrum in a nanosecond pulse discharge in N_2 (P=100 torr, 100 μs after beginning of current pulse) shown together with a synthetic spectrum (which is a superposition of individual Gaussian lineshapes). From reference [36].

spontaneous Raman spectra (δA_v) can be calculated as,

$$\delta f_v = \frac{A_v/(v+1)}{A_{tot}} \delta A_v \tag{3.9}$$

where A_v is the integrated area of vibrational level 'v', and A_{tot} is $\sum A_v$. In general, the uncertainty in the relative N_2 vibrational level populations, $\delta f_v/f_v$ ranged from 0.1% to 10%. For low vibration levels ($v = 0-3$), signal intensity was relatively high, and fits used to calculate the areas under the vibrational bands tended to be quite accurate, yielding uncertainties of $\delta f_v/f_v \approx \pm 0.1$-1.5%. At higher vibrational levels ($v = 4-7$), signal intensity was lower (due to lower populations of these levels), and

the fits became somewhat less accurate, with uncertainties of $\delta f_v/f_v \approx \pm$0.5-3.0%. At the highest vibrational levels measured ($v = 8 - 12$), the fits became significantly less accurate, resulting in uncertainties of $\delta f_v/f_v \approx \pm$1.0-10.0%.

In addition to uncertainty in the N_2 relative vibrational populations which arises from uncertainty in the fit due to low signal-to-noise, additional uncertainty arises due to the overlap of the vibrational bands in the fitting procedure ($\delta A_{v-overlap}$, since vibrational bands are not fully resolved). In general, lower vibrational bands have more significant overlap, while higher vibrational bands were increasingly better resolved. This represents a trend opposite to uncertainty arising from fitting, which increases with vibrational quantum number. Additional overlap uncertainty ranges from 0.1% to 7%. Taking into account both sources of uncertainty, the combined uncertainty of the N_2 vibrational level populations, $\delta f_{v-total}/f_v$, ranges from 2% to 12%.

It should be noted that statistical uncertainty (i.e. precision) of the N_2 vibrational level populations is not analyzed here. This is because the repeated measurements required for this type of analysis would require extremely long signal collection times, since accumulating a single spectrum requires up to 3-4 hours.

An additional parameter, characterizing the vibrational energy loading per molecule, is the average number of vibrational quanta per N_2 molecule, which can be calculated from the VDF as follows,

$$Q = \sum_{v=0}^{v=12} v f_v \tag{3.10}$$

Finally, 'first-level' N_2 vibrational temperature (the slope of the vibrational distribution function at $v = 0$), can be inferred from the $v = 0$ and $v = 1$ vibrational level

populations,

$$T_{V01} = \frac{\theta_{vib}}{ln\left(f_{v=0}/f_{v=1}\right)} \tag{3.11}$$

where θ_{vib} is the characteristic vibrational temperature (see section 2.3) of nitrogen; $\theta_{vib,N_2} = \omega_e\left(1 - \frac{2\omega_e x_e}{\omega e}\right) = 3353$ K.

3.6 0-D Kinetic Model

A 0-D, 'master equation' kinetic model was used to simulate the present experimental results in nitrogen (although not in air) to study kinetic mechanisms which control N_2 vibrational energy level populations in the discharge and afterglow. This model has been previously discussed in detail [36], and is therefore only briefly outlined here. In essence, the model incorporates key energy transfer processes in nitrogen and air nonequilibrium plasmas. These include vibrational and electronic excitation, as well as dissociation of N_2 and O_2 by electron impact, vibration-to-vibration (V-V) energy exchange among N_2, O_2, and NO molecules, vibration-to-translation (V-T) energy relaxation, plasma chemical reactions of various air species in their ground electronic states (N, N_2, O, O_2, O_3, NO, NO_2, and N_2O), as well as collisional and radiative quenching of electronically excited species {$N_2(A^3\sum)$, $N_2(B^3\Pi)$, $N_2(C^3\Pi)$, $N_2(a'^1\sum)$, $O_2(a^1\Delta)$, $O_2(b^1\sum)$, $O_2(c^1\sum)$, $N(^2D)$, $N(^2P)$, $O(^1D)$, $O(^1S)$}.

A two-term expansion Boltzmann equation solver using experimental electron impact cross sections, is used to predict the electron impact excitation rates as functions of the reduced electric field, E/N [38, 39]. A set of ordinary differential equations ('master equation') is used to predict time-dependent population of each vibrational level of N_2 in the ground electronic state:

$$\frac{df_v}{dt} = (e - V) + (V - V) + (V - T) + Diffusion, v = 0 - 45 \tag{3.12}$$

Vibrational nonequilibrium of O_2 and NO is taken into account using the harmonic oscillator approximation. For each of these species, vibrational nonequilibrium is accounted for by using a single equation for the vibrational energy mode. Justification for this approach is based on recent N_2 and O_2 vibrational population measurements in a nanosecond pulse discharge filament in air [37], which show significantly lower vibrational disequilibrium in oxygen, compared to nitrogen. Two other processes playing a key role in time-resolved vibrational level populations of the three major diatomic species (N_2, O_2 and NO) are V-V energy exchange,

$$AB(v) + AB(w) \rightleftarrows AB(v-1) + AB(w+1) \tag{3.13}$$

and V-T energy transfer (see section 2.3),

$$AB(v) + M \rightleftarrows AB(v-1) + M \tag{3.14}$$

In the present experiments, relatively low translational/rotational temperatures are expected (≈300 K), resulting in domination of single-quantum processes. State-specific V-V and V-T rates are taken from the literature ([40] and references therein). Rate coefficients for chemical reactions among the ground electronic state species are taken from the NIST Chemical Kinetics Database. The coupling of state-specific rates of chemical reactions (such as N_2, O_2 and NO dissociation and Zel'dovich mechanism reactions) and vibrational nonequilibrium is accounted for using the approach of Treanor, et al. [41]. Collisional quenching rates of excited electronic states, including electronic-electronic (E-E) energy transfer as well as reactive quenching rates are taken from the literature ([42] and references therein).

In the present work, a point-to-point (sphere-to-sphere) nanosecond pulse discharge between two bare, copper electrodes is utilized. The reduced electric field and

electron density in the plasma are inferred by the model from the experimental voltage and current waveforms, along with the filament diameter inferred from the ICCD images (see figures 3.6 and 3.8). Cathode voltage fall, v_c, is estimated by solving a set of parametric equations relating cathode voltage fall, and the discharge current density, assuming that a quasi-steady state, one-dimensional, abnormal glow discharge develops between the electrodes during the main discharge pulse. These relations can be found in reference [36, 25]. Modeling calculations are completed assuming constant pressure conditions in the discharge volume. The filament cooling rate is calculated from the characteristic diffusion time, which is in turn estimated based on the filament radius and diffusion coefficient.

3.7 VDF Measurements in Sphere-to-Sphere Nanosecond Pulse Discharge

This section details the experimental results on N_2 vibrational level populations using spontaneous Raman scattering. Time-resolved experimental data for the vibrational distribution function (VDF), first-level vibrational temperature, and average number of vibrational quanta per N_2 molecule are presented in nitrogen and air. In addition to the experimental results, the nitrogen discharge has been modeled by a 0-D, master equation kinetic model (see section 3.6). Time-resolved modeling results for the reduced electric field, electron density, species mole fractions, energy loading per molecule, VDFs, first-level vibrational temperature, translational/rotational temperature and average number of quanta per N_2 molecule are presented and compared to experimental data in nitrogen. Modeling predictions in air have not been obtained.

3.7.1 Results in Nitrogen

Results presented in this section are for nitrogen (99.998% pure) at P=100 torr with initial temperature of ≈300 K. Delay times (135 ns - 10 ms) are given with respect to the leading edge of the primary current pulse (t=0). Highly nonequilibrium conditions in the plasma filament were observed, with significant excitation of N_2 vibrations (up to v=12 observed). Energy coupled to the filament was ≈19 mJ/pulse, with 17 mJ coupled by the primary pulse and 2 mJ by the secondary pulse (see figure 3.4).

Figure 3.10 is a zoomed version of figure 3.4, showing experimental pulse voltage, current and coupled energy waveforms, which are used by the 0-D kinetic model to infer pulse reduced electric field (E/N) and electron density (see figure 3.11).

Figure 3.11 shows time-resolved reduced electric field (E/N) and electron density as calculated by the 0-D model from the experimental voltage and current waveforms, and the discharge filament diameter (≈2.3 mm FWHM from figure 3.8), as discussed in section 3.6. As can be seen, the electric field peaks just before breakdown (t=0) at ≈275 Td. Electron density is predicted to reach $\approx 4.5 \cdot 10^{14}$ cm^{-3}.

Figure 3.12 plots model predicted mole fractions of N atoms and excited electronic states of N_2. It can be seen that shortly after the pulse, N_2(A), N_2(a) and N_2(B) are the dominant excited states, while only N_2(a) remains in significant quantities for up to 100 μs after the pulse.

Figure 3.14 shows the experimentally obtained, first-level vibrational temperature (T_v) and average number of vibrational quanta per N_2 molecule. Although spontaneous Raman spectra could not be taken during the first 125 ns of the discharge pulse (due to strong interference from plasma emission), it is clear that an initial rise

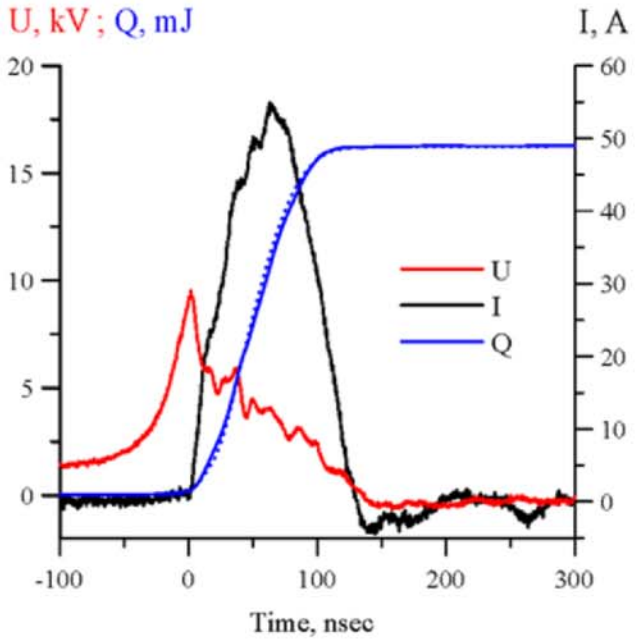

Figure 3.10: Experimental pulse voltage, current and coupled energy waveforms (P=100 torr, nitrogen). From reference [36].

in vibrational quanta occurs during the pulse. For a short duration after the end of the primary discharge pulse (135 ns - 1 μs) the average number of vibrational quanta remains nearly constant. Following this, an apparent, secondary rise by $\approx$70% occurs from 1 μs to 10 μs. This appears to indicate that additional energy is loaded into N_2 vibrations after the discharge pulse. However, it may be possible that this apparent rise is due to the expansion of the discharge filament, which becomes significant on this timescale, coupled with some lateral movement of the filament shot-to-shot. Figure 3.13 shows ICCD images taken in a nanosecond pulse plasma, sustained between two spherical electrodes in air for 200 ns (left), 300 ns (middle) and 400 ns (right)

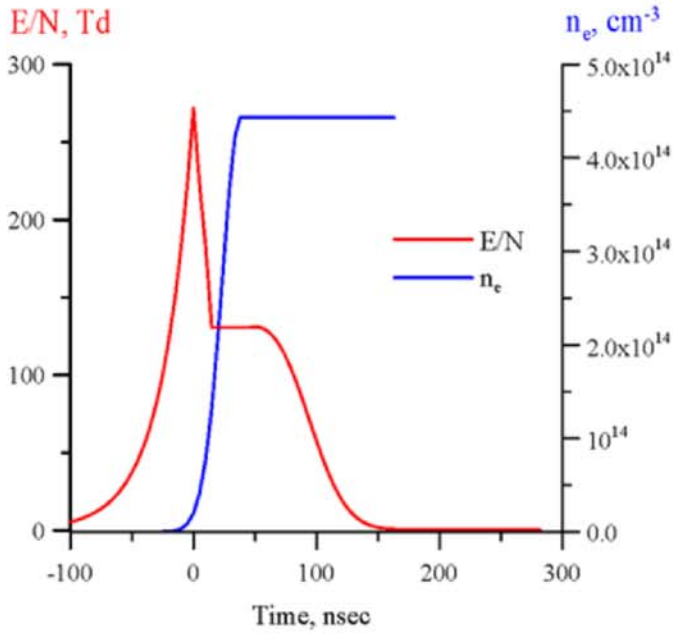

Figure 3.11: Pulse reduced electric field (E/N) and electron density profiles, inferred from the waveforms in figure 3.10 with 0-D kinetic model (P=100 torr, nitrogen). From reference [36].

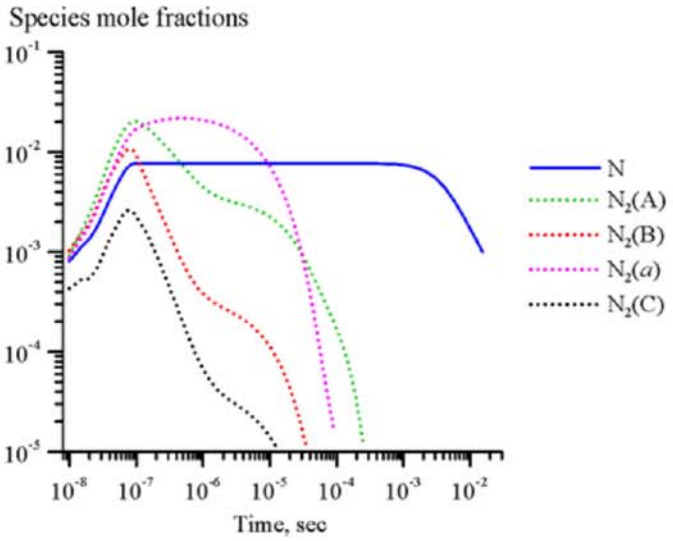

Figure 3.12: N-atom and excited electronic state species mole fractions predicted by the 0-D kinetic model (P=100 torr, nitrogen). From reference [36].

after the secondary discharge pulse. 30-shot averaging is used for all images. It can be observed that the filament expands significantly over this time period.

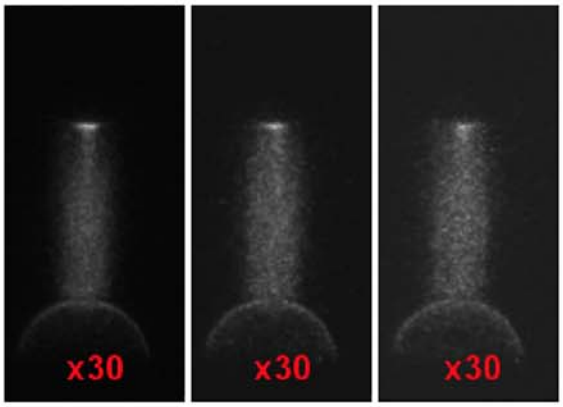

Figure 3.13: ICCD images of nanosecond pulse plasma sustained between two spherical electrodes in air (P=100 torr) for 200 ns (left), 300 ns (middle) and 400 ns (right) after the secondary discharge pulse illustrating filament expansion with time. The images are averaged over 30 discharge pulses

Recall that Raman spectra are obtained from a 2.75 mm long line across the filament diameter in the longitudinal direction (direction of laser beam travel, see figure 3.3). However, in the lateral direction (perpendicular to the laser beam), the volume probed by the laser is only $\approx$60 μm diameter (beam waist). Initially, the filament diameter is relatively small ($\approx$2.3 mm FWHM). If the filament moves laterally, even slightly ($<$.1 mm), the laser beam may probe the peripheral region of the plasma, which is not as strongly excited. Because of this effect, the average number of vibrational quanta per N_2 molecule measured would appear to be somewhat lower than the value on the filament centerline. However, as the filament expands radially outward later in time (on the order of microseconds), this effect would become less

significant, as the laser beam would more consistently probe a region of the plasma that is closer to the centerline (i.e. more excited, nonequilibrium region). As a result, an apparent rise in vibrational quanta at this time would appear, as is seen in the data. This phenomenon, analyzed in more detail in section 3.7.3, appears to be consistent with similar measurements conducted in a sphere-to-sphere, nanosecond pulse filament discharge by Montello, et al. [13] using the same high voltage pulse generator. In their experiment, Coherent Anti-Stokes Raman Scattering (CARS) was used to measure N_2 vibrational level populations at conditions similar to the present work. An even greater increase in vibrational quanta per N_2 molecule after the discharge was observed in their case (as much as 90% in nitrogen). Since the plasma volume in CARS is much smaller than at the present conditions, ≈0.5 mm x 100 μm [13], the effect of plasma filament radial expansion would be even stronger. Furthermore, since CARS collects the signal over a much shorter region in the direction of the laser beam, longitudinal movement of the filament would effect the CARS measurement as well, perhaps even to a larger degree. In the spontaneous Raman scattering study presented here, the signal is inherently averaged in the longitudinal direction (over a 2.75 mm line), and therefore a lesser overall affect of the plasma filament expansion is observed (only due to filament expansion in the lateral direction).

From figure 3.14, it can be seen that the first-level N_2 vibrational temperature after the pulse reaches a plateau (at 200-800 ns) before rising steadily from 1 μs to ≈20 μs, when it peaks at ≈4200 K. The vibrational temperature then steadily decreases, eventually approaching near-equilibrium conditions. This behavior is analyzed in more detail in the discussion related to figure 3.16.

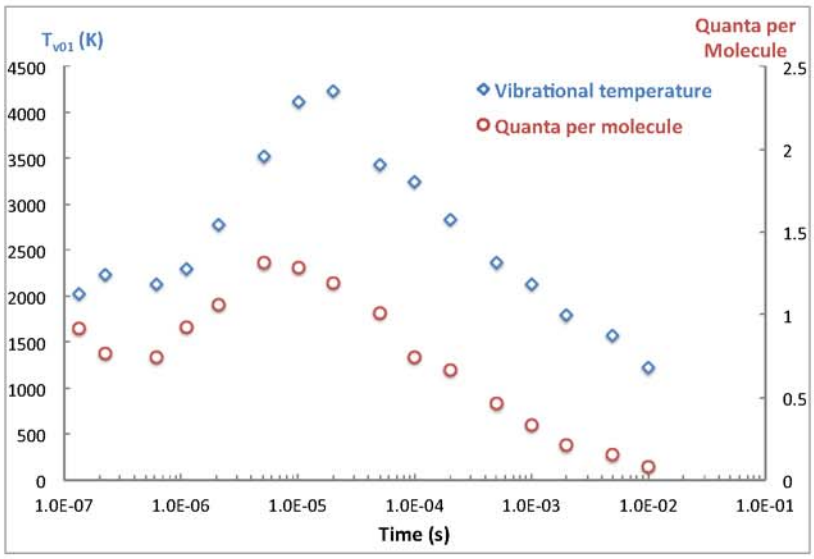

Figure 3.14: N_2 first level vibrational temperature and average number of vibrational quanta per N_2 molecule in a nanosecond pulse discharge and afterglow in nitrogen (P=100 torr).

Recalling figure 3.11, it can be seen that for the portion of the discharge pulse from 25 ns to 100 ns, the reduced electric field (E/N) is on the order of 100 Td. This corresponds to a timescale when a significant fraction of the discharge input energy is expected to be loaded into the N_2 vibrational mode by electron impact ($\approx$50% at E/N = 100 Td). Discharge energy loading per molecule and energy loaded into nitrogen vibrations, as predicted by the model, are shown in figure 3.15. The model predicts approximately 32% (240 meV/molecule) of the total coupled energy (740 meV/molecule) to be loaded into the N_2 vibrational mode. Also shown is the comparison between model and experimental number of average vibrational quanta per N_2 molecule. After an initial rise during the discharge pulse, the model predicts the number of vibrational quanta to remain essentially constant from t$\approx$100 ns - 100 μs.

This prediction stems from the fact that the total number of quanta in the N_2 vibrational mode is conserved during V-V exchange among nitrogen molecules. Thus, if the effect of the secondary rise of the number of quanta is due to expansion/movement of the plasma filament, the model would not be able to reproduce it. The decay of the number of quanta per N_2 molecule is reproduced by the model, since it includes V-T relaxation and radial diffusion, both of which reduce the average number of quanta. However, peak number of vibrational quanta per N_2 molecule (at 10-100 μs) is underpredicted by the model by $\approx$40%. Following this, the model predicts that the number of vibrational quanta decays back to near-equilibrium conditions on the scale of several milliseconds, due to radial diffusion.

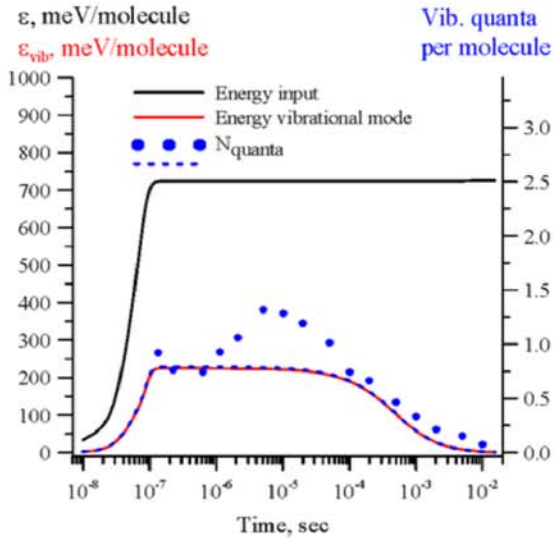

Figure 3.15: **Discharge energy loading per molecule**, **energy into N_2 vibrations** and **number of vibrational quanta per N_2 molecule** predicted by the 0-D kinetic model and compared with experimental data in a nanosecond pulse discharge in nitrogen (P=100 torr). From reference [36].

Figure 3.16 shows a comparison between the experimental and model predicted first-level N_2 vibrational temperature, along with the predicted rotational/translational temperature. As is shown, the vibrational temperature rise immediately following the discharge pulse, along with its subsequent decay is predicted fairly well by the model. However, the model underestimates both the absolute rise (i.e. peak temperature value), as well as the rate of vibrational temperature rise for the first $\approx$20 μs after the discharge pulse. However, the qualitative trend is captured reasonably well, which suggests that the observed N_2 vibrational temperature rise after the pulse is largely due to V-V exchange among N_2 molecules (see figures 3.20-3.22 and surrounding discussion).

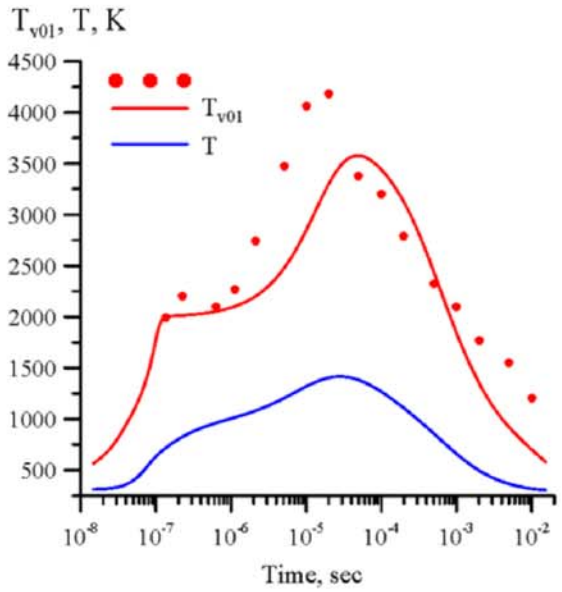

Figure 3.16: Comparison between experimental and predicted N_2 first level vibrational temperature, with model prediction for translational/rotational temperature (P=100 torr, nitrogen). From reference [36].

Figures 3.17-3.19 show the experimentally extracted N_2 VDFs in a nanosecond pulse discharge in nitrogen for 135-635 ns, 1-10 μs, and 20 μs-10 ms time delays, respectively. Figure 3.17 shows results for the time regime immediately following the primary discharge pulse (135-635 ns). This corresponds to the plateau region in figure 3.14. Here it can be seen that the distributions are nearly on top of each other, and there is little change in the vibrational populations at this stage.

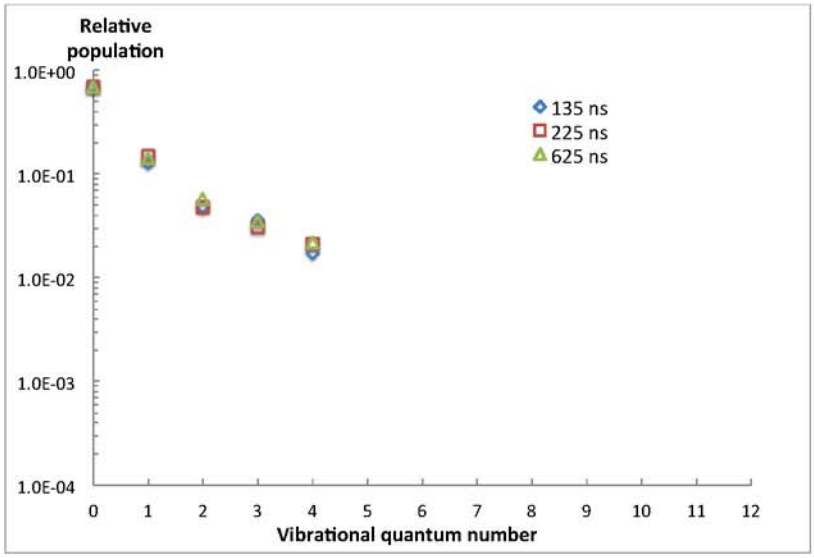

Figure 3.17: Experimental N_2 vibrational level populations for time delays ranging from 135 ns to 635 ns after the beginning of the discharge pulse (P=100 torr, nitrogen).

Figure 3.18 shows the N_2 VDFs for time delays from 1 μs to 10 μs, which represents the stage with vibrational temperature rise and apparent secondary rise in the number of average vibrational quanta per N_2 molecule in figure 3.14. At this point, the VDFs begin to show a rise in the populations of the higher vibrational levels.

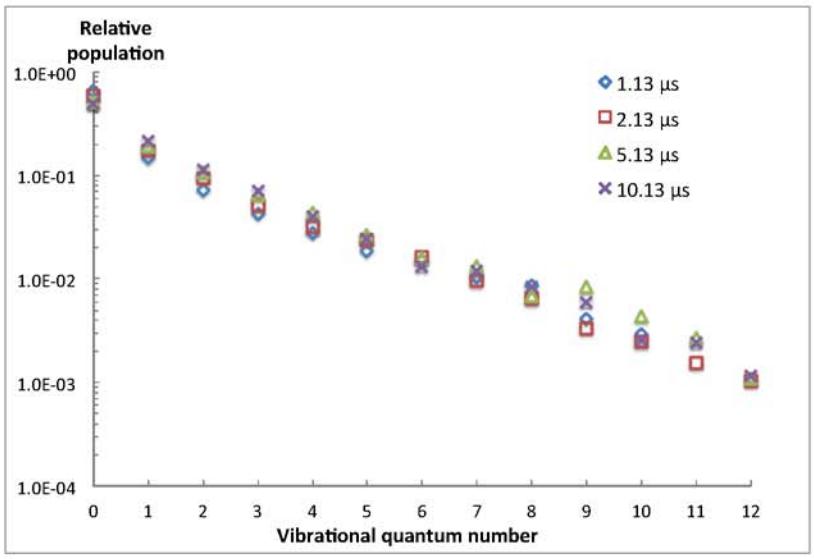

Figure 3.18: Experimental N_2 vibrational level populations for time delays ranging from 1 μs to 10 μs after the beginning of the discharge pulse (P=100 torr, nitrogen).

Figure 3.19 plots the time delays from 20 μs-10 ms, which represents the stage when T_v and Q peak and then decay in figure 3.14. At this stage, radial diffusion begins to dominate, such that gradual decay to near equilibrium can be observed.

Figures 3.20-3.22 compare the experimental results shown in figures 3.17-3.19 with the modeling predictions for the VDFs. In figure 3.20, it can be seen that the model predicts the initial vibrational energy distribution, which is created by electron impact during the discharge pulse, fairly well, although somewhat overpredicting vibrational level populations $v \geq 2$.

Figure 3.21 shows the results for the t =1 to 10 μs range. Here, the model does not reproduce the apparent continuous rise of the v=2-12 vibrational level populations. Rather, a gradual redistribution of these vibrational level populations by V-V exchange is predicted. Underprediction of $v \geq 9$ by the model is expected because

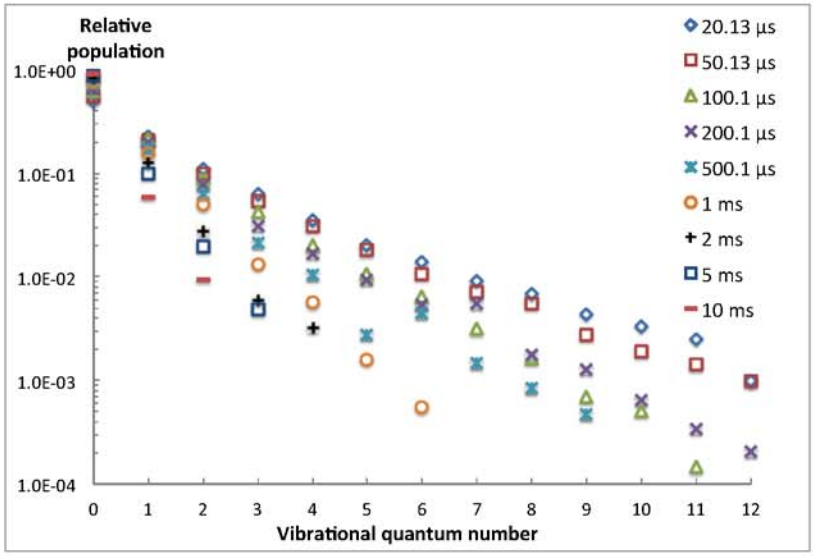

Figure 3.19: Experimental N_2 vibrational level populations for time delays ranging from 20 μs to 10 ms after the beginning of the discharge pulse (P=100 torr, nitrogen).

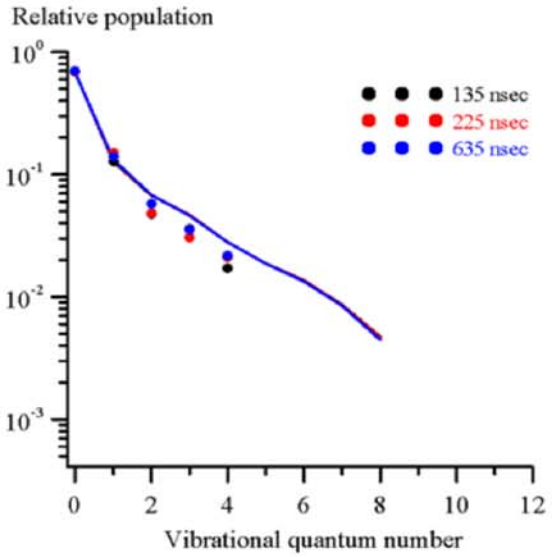

Figure 3.20: Comparison of experimental and 0-D model predicted N_2 vibrational level populations for time delays of 135 ns-635 ns after the beginning of the discharge pulse in nitrogen(P=100 torr). From reference [36].

it only incorporates electron impact vibrational excitation processes for $v = 0 - 8$, for which experimental cross sections are available. However, it is also apparent that the rise in $v = 2 - 12$ populations is not reproduced. As discussed previously, this may be caused, to some extent, by the expansion and lateral movement of the plasma filament (see discussion related to figure 3.14). At this stage, the model predicts that the VDF becomes closer to a Treanor distribution, due to the V-V energy transfer process,

$$N_2(v = 0) + N_2(w) \rightarrow N_2(v = 1) + N_2(w - 1) \tag{3.15}$$

which results in "downward" flow of vibrational quanta. This process is also responsible for the rise in the first-level N_2 vibrational temperature which occurs during the 1 μs to 20 μs time regime (see figure 3.14), although the total number of vibrational quanta per N_2 molecule predicted by the model remains the same. This effect is evident in figure 3.16, although it is even more pronounced in the experimental data due to the apparent rise in vibrational quanta per molecule as discussed above.

Finally, figure 3.22 compares the experimental and predicted VDFs during the relaxation to near equilibrium (50 μs-10 ms after the pulse). It can be seen that the model captures the qualitative relaxation trend well, however, the relaxation rate is significantly overpredicted. This may be due to the fact that, in the modeling calculations, the VDF begins relaxation from significantly lower peak vibrational level populations than in the experiment.

Figures 3.23 and 3.24 provide additional illustration of these vibrational distribution function trends over time by plotting the populations of select vibrational levels vs. time. Figure 3.23 shows only the experimental data, while figure 3.24 shows a comparison between the model-predicted values and the experiment. From these

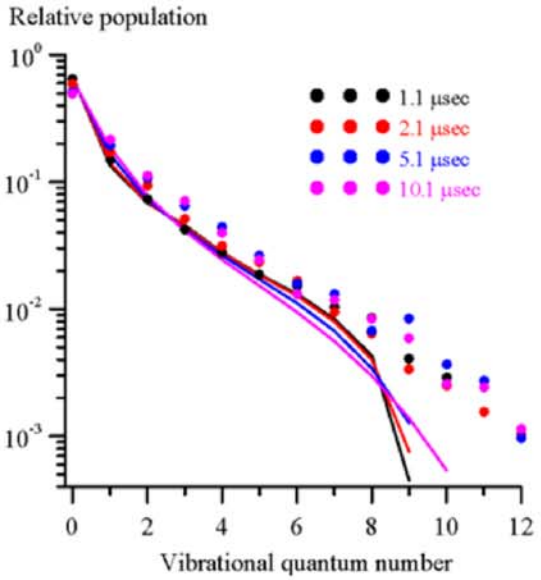

Figure 3.21: Comparison of experimental and 0-D model predicted N_2 vibrational level populations for time delays of 1 μs-10 μs after the beginning of the discharge pulse in nitrogen (P=100 torr). From reference [36].

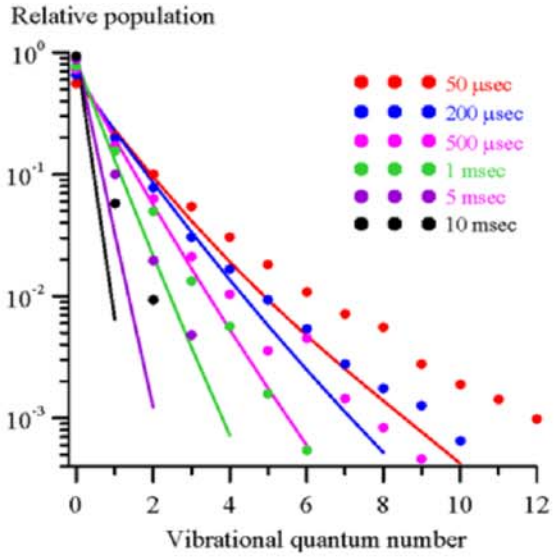

Figure 3.22: Comparison of experimental and 0-D model predicted N_2 vibrational level populations for time delays of 50 μs-10 ms after the beginning of the discharge pulse in nitrogen (P=100 torr). From reference [36].

figures, it can be clearly seen that experimental vibrational levels v=1-4 exhibit significant population increase from t=1-10 μs. This is consistent with the apparent rise in the number of vibrational quanta per molecule at this time. Following this, vibrational populations at levels $v > 2$ remain relatively constant until $\approx$20 μs. At this point, populations of vibrational levels $v > 10$ begin to relax (primarily due to V-V exchange; see eqn. 3.15). Populations of lower levels also begin to decay since radial diffusion begins to dominate all vibrational level populations (v=2-12), reducing them towards near equilibrium conditions.

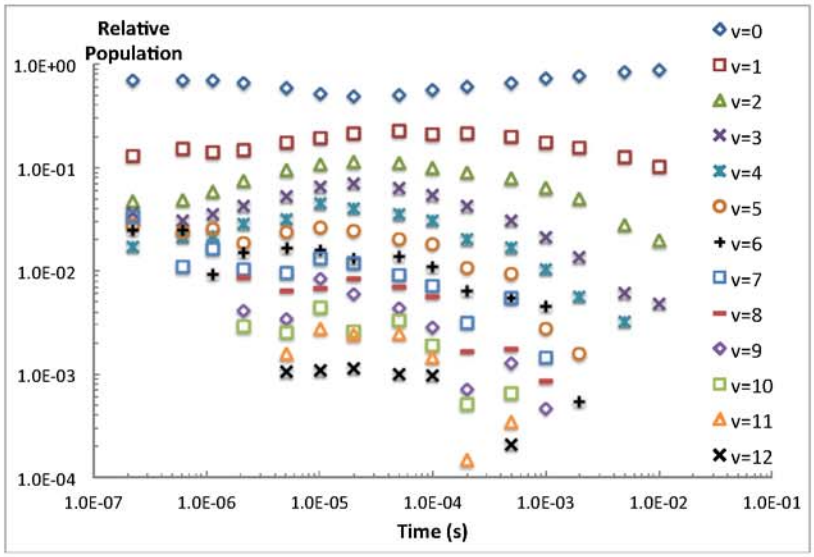

Figure 3.23: Time-resolved N_2 vibrational level populations for all vibrational levels observed in the present experiments ($v = 0 - 12$, P=100 torr, nitrogen).

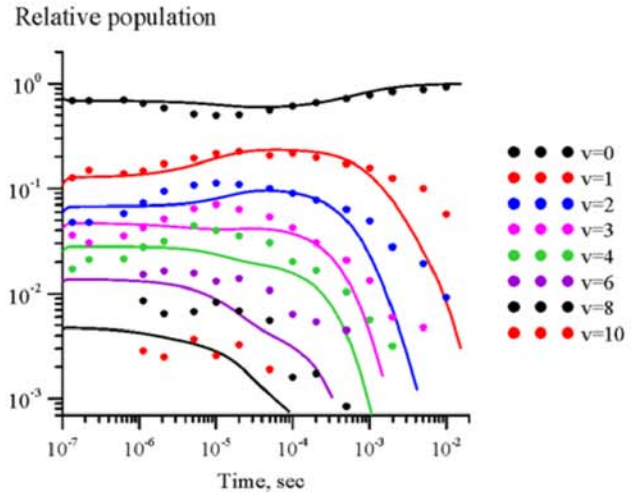

Figure 3.24: Experimental and 0-D model predicted comparison of time-resolved N_2 vibrational level populations for select observed vibrational levels (P=100 torr, nitrogen). From reference [36].

3.7.2 Results in Air

The experimental data presented in this section are taken in a nanosecond pulse discharge sustained in "vehicle emission zero" (low hydrocarbon content), air at P=100 torr with initial temperature of ≈300 K. Data are taken at delay times from 200 ns to 5 ms with respect to the leading edge of the primary current pulse (t=0). Similar to nitrogen plasma, highly nonequilibrium conditions in the air plasma filament were observed, with significant excitation of the N_2 vibrational mode (vibrational level populations up to v=11 observed). Energy coupled to the filament was ≈14 mJ/pulse, with 12.5 mJ coupled by the primary pulse and 1.5 mJ by the secondary (see figure 3.5).

Figure 3.25 shows experimentally obtained, 'first-level' N_2 vibrational temperature (T_{V01}) and average number of vibrational quanta per N_2 molecule. Similar to the

nitrogen results, an initial rise in average number of vibrational quanta during the pulse occurs. However, at this point, the trend for the number of average quanta per molecule begins to differ from that of nitrogen. Following the primary pulse (200 ns - 1 μs), instead of remaining steady, as occurs in nitrogen, the number of vibrational quanta per N_2 molecule continues to steadily rise. There is perhaps a brief period of time, from 1-2 μs, when the number of quanta per molecule remains steady, however more data would need to be collected during this time range to confirm this. Following this, an apparent, secondary rise appears from 2 μs to 10 μs. This, once again, may be due to the expansion of the filament coupled with some, pulse-to-pulse lateral movement of the filament (see explanation in section 3.7.1). It is notable, however, that the apparent secondary rise in the number of vibrational quanta is less pronounced than in nitrogen ($\approx$30% in air as opposed to $\approx$70% in N_2). This trend is similar to the one detected in CARS measurements in a ns pulse discharge at similar conditions by Montello, et al. [13], where N_2 quanta increase in nitrogen on this timescale was measured to be $\approx$85%, while an increase of only $\approx$45% was observed in air at otherwise similar conditions. Direct comparison between the number of vibrational quanta per molecule in nitrogen and air is shown in figure 3.26.

The 'first-level' N_2 vibrational temperature follows a similar trend to nitrogen; it remains nearly constant from 200 ns to 1 μs, followed by a steady increase between 1-100 μs, and subsequent decay to near equilibrium. It is notable that the absolute rise in the vibrational temperature from 1 to 100 μs after the discharge pulse is significantly less pronounced than in nitrogen, and also that the rise continues over a longer period of time (an additional $\approx$60 μs compared to nitrogen). This suggests a significant effect of V-T relaxation by O atoms, which limits peak N_2 vibrational

temperature in the afterglow. Direct comparison between T_{V01} measured in nitrogen and air is shown in figure 3.26.

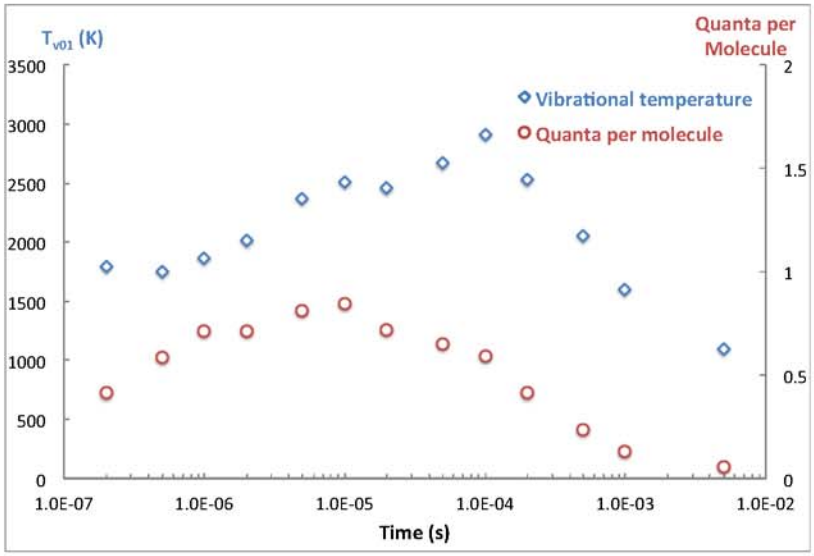

Figure 3.25: N_2 first level vibrational temperature and average number of vibrational quanta per N_2 molecule in a nanosecond pulse discharge in air (P=100 torr).

Figures 3.27 and 3.28 show the N_2 VDFs inferred from experimental Raman scattering spectra at 200 ns-5 μs and 10 μs-5 ms, respectively. Figure 3.27 shows VDFs for the time period immediately following the primary discharge pulse (t = 200 ns) through the moment where the average number of vibrational quanta per N_2 molecule peaks ($t = 5$ μs; see figure 3.25). During this stage, it can be observed that $v = 1 - 9$ vibrational level populations appear to rise slightly. On this time scale, it is almost certain that V-V exchange processes, conserving vibrational quanta, dominate vibrational energy transfer.

Figure 3.28 shows the VDFs obtained from 10 μs to 5 ms after the discharge pulse, where the average number of vibrational quanta per molecule begins to decrease (see

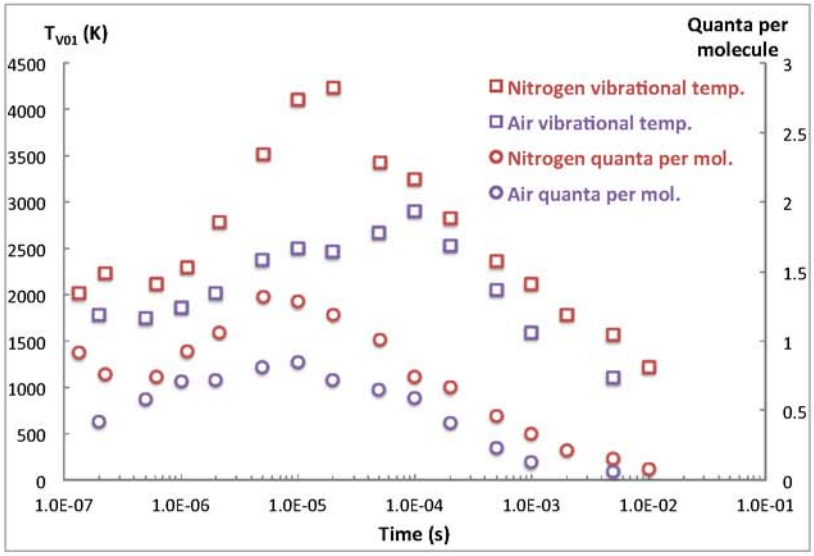

Figure 3.26: Comparison of N_2 first level vibrational temperature and average vibrational quanta per N_2 molecule between nitrogen and air nanosecond pulse discharges (P=100 torr).

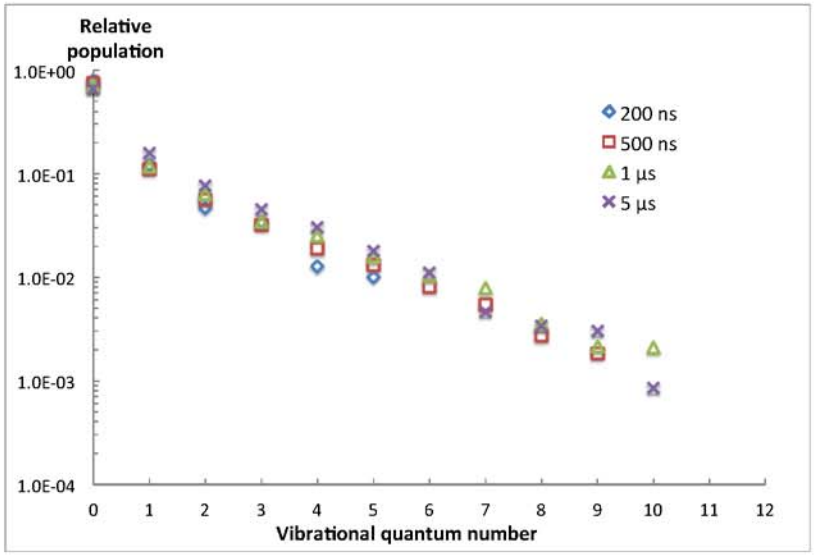

Figure 3.27: Experimental N_2 vibrational level populations for time delays of 200 ns to 5 μs after the beginning of the discharge pulse in air (P=100 torr).

figure 3.25). It can be observed here that all excited vibrational levels, with the exception of v=1, which continues to rise until ≈100 μs due to 'downward' V-V exchange (see equation 3.15), begin to decay, likely due to V-T relaxation of N_2 by O atoms. Eventually, higher vibrational level populations become undetectable with the current diagnostic. Vibrational levels up to v=11 were detected in air (at $t = 10$ μs).

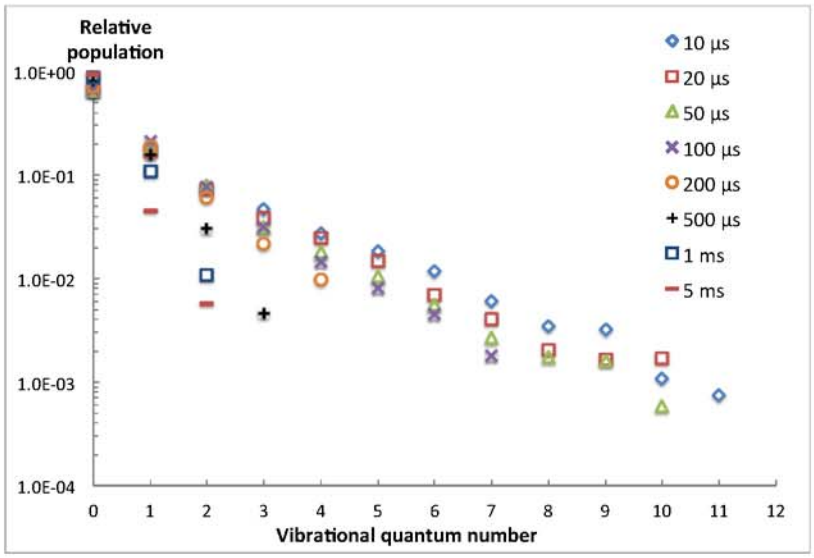

Figure 3.28: Experimental N_2 vibrational level populations for time delays of 10 μs to 5 ms after the beginning of the discharge pulse in air (P=100 torr).

Figure 3.29 provides an additional perspective of vibrational level population change over time by plotting the populations of select vibrational levels vs. time. From this figure, it can be clearly seen that vibrational levels v=1-6 show moderate population increase from 1 to 10 μs. This is consistent with the apparent, secondary rise in number of vibrational quanta per N_2 molecule at this time. Following this, populations of vibrational levels $v > 2$ remain relatively constant until ≈20 μs. At

this point, moderate and higher vibrational levels ($v > 3$) begin to relax (primarily by V-V exchange, see eqn. 3.15). Subsequently lower level populations begin to decay, until V-T relaxation of N_2 by O atoms and radial diffusion become dominant and populations of all detected levels (v=2-12) are reduced quickly towards near equilibrium conditions (starting around 100 μs).

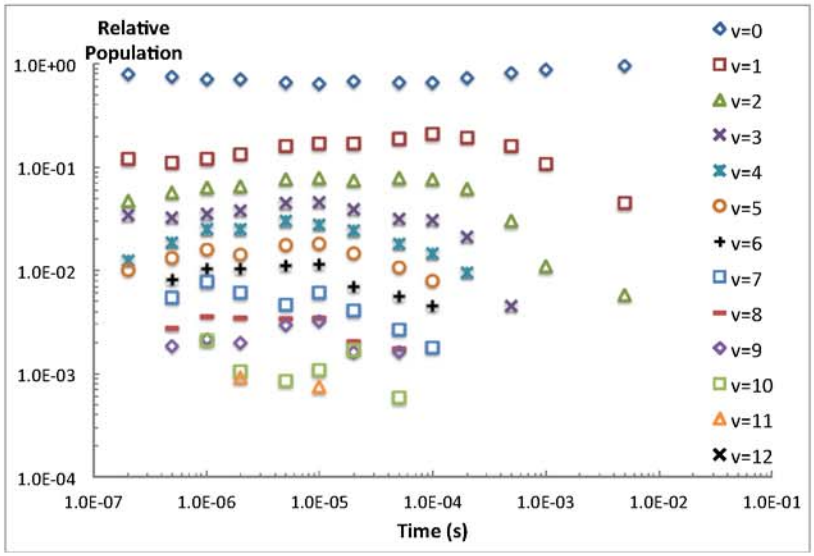

Figure 3.29: Time-resolved N_2 vibrational level populations for all observed vibrational levels in a nanosecond pulse discharge in air (P=100 torr).

3.7.3 Preliminary Spatially-Resolved Measurements

In order to determine how significant of an effect the plasma filament expansion has on the number of vibrational quanta per N_2 molecule and first-level N_2 vibrational temperature measurements, additional time-resolved spontaneous Raman spectra, for different sized signal collection regions in the plasma, were collected. The signal collection region size was controlled by limiting the vertical region-of-interest (ROI)

on the ICCD camera. By reducing the size of this ROI vertically, scattering signal from an effectively shorter portion of the focused laser line is collected by the camera. Two ROIs, corresponding to a 2.75 mm long region along the laser beam (ROI 1, 105 camera pixels; same as previously presented data in sections 3.7.1, 3.7.2) and a 1.75 mm long region along the laser beam (ROI 2, 65 camera pixels) were collected for select time delays after the discharge pulse. The resulting number of vibrational quanta per N_2 molecule and first-level N_2 vibrational temperatures are compared in figure 3.30, where ROI 1 is shown in red, and ROI 2 in blue.

Comparing the number of vibrational quanta per N_2 molecule (circles in figure 3.30), it can be observed that initially ($t \leq 2$ μs) the smaller ROI (ROI 2) results in a slightly higher value. However, after this time, once the filament has begun to significantly expand, the number of quanta measured using ROI 1 becomes higher. This supports the interpretation given in section 3.7.1 that the coupling of small lateral movement of the filament with filament expansion is at least partially responsible for the apparent secondary rise in number of vibrational quanta per molecule observed in the data, when in reality the initial rise in the number of quanta (during the discharge pulse; t <150 ns) is underestimated. In the case of the smaller ROI (ROI 2), the data are collected initially within the more strongly excited, near-axis portion of the plasma filament compared to the larger ROI (ROI 1), resulting in a higher number of quanta per molcule. However, as the filament expands, the smaller ROI actually detects a smaller portion of the more intensely excited regions of the plasma, resulting in a lower measured number of vibrational quanta per N_2 molecule.

Comparing the first-level vibrational temperatures for the two ROIs in figure 3.30, it can be observed that there is relatively little difference (<7%) at short time delays

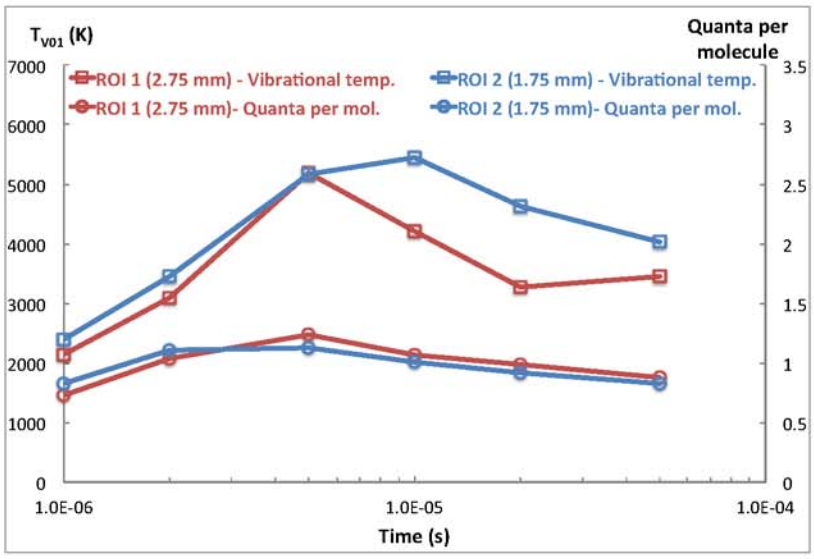

Figure 3.30: N_2 first level vibrational temperature and number of vibrational quanta per N_2 molecule for two different Raman scattering signal collection volumes, or regions of interest (ROI) in a nanosecond pulse discharge in nitrogen (P=65 torr, nitrogen). ROI 1=2.75 mm region (105 camera pixels, used in all previous data). ROI 2=1.75 mm region (65 camera pixels).

after the pulse ($t \leq 5$ μs), but as filament expansion becomes a prevalent factor, the smaller ROI shows a significantly higher vibrational temperature (up to $\approx$35%). It is likely that with the larger ROI (ROI 1), a larger portion of the more highly excited region of the plasma is captured during filament expansion. This more highly excited region would have more highly populated $v > 2$ levels, and less populated v=0 and v=1 levels (which control first-level vibrational temperature). Thus, a lower T_{V01} would be measured, on average, for ROI 1 compared to the smaller ROI 2. Clearly, spatially-resolved measurements across the filament, particularly at time delays when filament expansion is prevalent ($t > 2$ μs) are needed to draw more definite conclusions.

Chapter 4: Development of Triple-Grating Spectrometer Thomson Scattering Instrument

This chapter details the development of the triple-grating spectrometer used in the Thomson scattering experiments that are presented in chapter 5. The chapter begins with a summary of the motivation for using a triple-grating spectrometer instrument for the Thomson scattering technique (section 4.1). This is followed by a brief overview of Thomson scattering theory (section 4.2), as well as a comparison between the Thomson and Rayleigh scattering profiles (section 4.3). Next, the design and implementation of the triple-grating spectrometer used in the work in chapter 5 is summarized (section 4.4). The chapter concludes with a brief discussion of laser probe energy considerations that were taken into account for the Thomson scattering experiments (section 4.5).

4.1 Motivation

4.1.1 Experimental Issues

As discussed in chapter 1, the Thomson scattering technique provides a non-intrusive method to measure both spatially and temporally resolved electron density,

electron temperature and energy distribution in nonequilibrium plasmas. These parameters and their behavior in these environments are of vital importance for understanding the fundamental kinetic processes that dominate these plasmas in various applications (e.g. plasma flow control, plasma assisted combustion, etc.). Insight into these kinetics can be obtained using a combined effort of measuring them experimentally and comparing the results with kinetic modeling predictions.

Thomson scattering has a number of advantages compared to Langmuir probes and microwave interferometry due to its non-intrusive nature and ability to measure electron temperature and energy distribution. However, Thomson scattering also has some disadvantages. Most importantly, it has inherently, very weak scattering intensity, which makes it susceptible to several key sources of interference.

4.1.2 Sources of Interference

The most important source of interference in Thomson scattering is other quasi-elastic scattering signal, such as, Rayleigh scattering, which is the quasi-elastic scattering of light from neutral species. Since neutral species number densities in nonequilibrium plasmas are several orders of magnitude higher than those of charged species (Thomson scattering species), Rayleigh scattering presents a significant problem to Thomson scattering data collection. This is discussed in more detail in section 4.3.

Other significant interference sources include stray light and plasma emission. Stray light is often generated from incidental surface scattering, and even very small amounts can significantly impact Thomson scattering signal data collection. Plasma emission, generated primarily due to spontaneous emission from excited electronic

states of atoms and molecules in the plasma, is often very intense during and after the pulse in nanosecond pulse plasmas, contributing significantly to interference. The approaches utilized to resolve these problems are discussed in more detail in sections 4.4 and 5.2, respectively.

One final consideration when taking Thomson scattering measurements is the potential for laser-induced (or optical) breakdown to occur. When focusing a high energy, short-duration, pulsed laser beam, if the laser peak power density and gas pressure are sufficiently high, the electromagnetic wave (i.e. the laser beam) can cause an electron avalanche to form, and subsequent breakdown of the gas, thus producing an extra influx of free-electrons and ions at the measurement region within the larger nanosecond pulsed plasma. If this occurs, the measurement technique is no longer non-intrusive, and electron density and temperature measurements would be strongly effected. Thus it is important to avoid this phenomena when performing Thomson scattering. This is discussed in more detail in section 4.5.

4.2 Thomson Scattering Overview

Thomson scattering is the quasi-elastic scattering of light by free charged particles (i.e. ions and electrons). For an overview of general scattering theory, which is based on density gradients in the scattering volume, see section 3.1. Since ions are much heavier than electrons, their contribution to the Thomson scattering signal is usually negligible, and only the contribution from free electrons is of importance. Though Thomson scattering has a relatively large cross section (≈100 times larger compared to that of Rayleigh scattering depending on the species), due to much higher electron velocities, there are relatively few free electrons in a plasma (i.e. low electron number

density), resulting in a very weak overall scattering intensity. As a result of this, as well as difficulties from interference sources such as Rayleigh scattering, plasma emission and stray light, Thomson scattering experiments are generally limited to plasmas with reasonably high electron number densities and temperatures ($n_e \gtrsim 10^{13}$ cm^{-3}, $T_e \approx$10-100s of eV), although some researchers have measured electron densities as low as 10^{10} cm^{-3} [19].

Thomson scattering theory has been detailed elsewhere in the literature [43, 44], and will therefore be only summarized here. The differential Thomson scattering cross section for linearly polarized photons can be expressed as [24],

$$\frac{d\sigma}{d\Omega} = \left(\frac{e^2}{4\pi\epsilon_0 m_e c_0^2}\right)^2 \left(1 - cos^2\phi\right) = r_e^2 \left(1 - cos^2\phi\right) \tag{4.1}$$

where ϵ_0 is the permittivity in vacuum, ϕ is the scattering angle, or the angle between the incident light wave vector and the scattered light wave vector, and r_e is the electron radius (r_e=2.818$\times 10^{-15}$ m). The differential cross section can be integrated over the full solid angle to obtain the integrated Thomson scattering cross section,

$$\sigma_T = \frac{8}{3}\pi r_e^2 = 6.65 \times 10^{-25} cm^2 \tag{4.2}$$

which is notably independent of incident radiation wavelength (unlike Rayleigh and Raman scattering cross sections).

Figure 4.1 shows the wave vector diagram for the Thomson scattering process induced by a coherent laser beam. The wave vector of the incident radiation is given by $\mathbf{k}_0$, the wave vector of the scattered light by $\mathbf{k}_s$, and the differential scattering wave vector by $\mathbf{k}$, with

$$\mathbf{k} = \mathbf{k}_s - \mathbf{k}_0 \tag{4.3}$$

If it is assumed that the scattered radiation has the same wavelength as the incident light (i.e. scattering is fully elastic), the magnitude of the differential scattering wave vector is given by [24],

$$|\mathbf{k}| = k \cong 2|\mathbf{k}_0| sin\left(\frac{\theta}{2}\right) = \frac{4\pi}{\lambda} sin\left(\frac{\theta}{2}\right) \tag{4.4}$$

where θ is the scattering angle, and λ is the wavelength of the incident radiation.

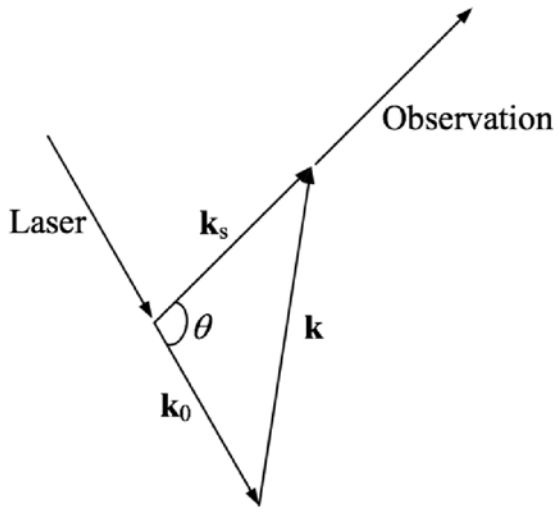

Figure 4.1: Thomson scattering wave vector diagram. $\mathbf{k}_0$ is the incident laser radiation vector, $\mathbf{k}_s$ is the scattered light wave vector, and $\mathbf{k}$ is the differential scattering wave vector. From reference [24].

In general, individual contributions to the scattering intensity from every free electron and ion in the scattering volume should be added coherently to obtain the full scattering signal intensity. This requires obtaining information on the relative phases of each contributing electron and ion, in addition to the amplitude. However, in low electron density plasmas, where the incident photon wavelength is much

shorter than the effective distance between free electrons, the phases of the contributions are uncorrelated, and electrons and ions can be essentially viewed as individual, randomly distributed particles. This limit is called incoherent Thomson scattering, and is characterized by the dimensionless Salpeter parameter [45],

$$\alpha = \frac{1}{k\lambda_D} \tag{4.5}$$

where k is the magnitude of the scattering wave vector, and λ_D is the Debye length (eqn. 1.1).

When $\alpha \ll 1$ (which is true for $n_e \lesssim 10^{18}$ cm^{-3}), free charged species do not significantly affect each other (i.e. Coulomb interactions are negligible), and the total scattering intensity is simply the sum of the intensities from each scatterer. In addition, due to a much smaller cross section for scattering by ions at these number densities, ionic contributions can be ignored and only scattering from free electrons is of importance. Ion and electron contributions to the Thomson scattering intensity are plotted vs. α in figure 4.2. In all experiments presented in chapter 5, $\alpha \ll 1$ (max value $\alpha \approx 0.08$), such that Thomson scattering is incoherent, and ion contributions are negligible.

In the limit of $\alpha \to 0$, the Thomson scattering lineshape reduces to a Gaussian lineshape, which is a function of the Maxwellian velocity distribution for the electrons ($f_e(\mathbf{v})$),

$$S(k) = \left(\frac{k}{2\pi}\right) f_e(\mathbf{v}) \tag{4.6}$$

with,

$$f_e(\mathbf{v}) = \sqrt{\left(\frac{m_e}{2\pi k_B T_e}\right)^3} 4\pi \mathbf{v}^2 \exp\left[-\frac{m_e \mathbf{v}^2}{2k_B T_e}\right] \tag{4.7}$$

where $\mathbf{v}$ is the velocity and m_e is the electron mass.

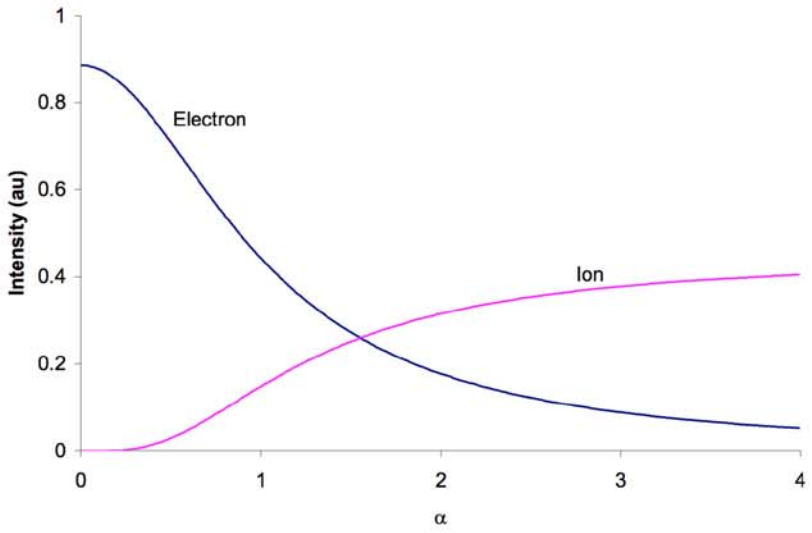

Figure 4.2: Electron and ion relative contributions to Thomson scattering intensity as functions of α parameter. From reference [24].

As α increases, the velocity distribution becomes increasingly non-Maxwellian, and eventually side-bands appear in the scattering spectrum, which are the result of fluctuations in charge density within the scattering volume. When the effective length for these fluctuations becomes short compared to the scattering wave vector, which occurs at high electron densities, the side-bands are formed. These are analogous to Brillouin scattering side-bands, which arise from density fluctuations propagating as acoustic waves in environments without charged particles. To illustrate what this effect does to the Thomson scattering lineshape, the Salpeter spectral function ($\Gamma_\alpha(x)$), which is essentially equivalent to the Thomson lineshape, is plotted for different α values in figure 4.3 [45]. Side band formation, as the value of α increases, is apparent. The deviation of the electron velocity distribution from Maxwellian is studied and discussed in more detail when the Thomson scattering data reduction procedure for

inferring the electron energy distribution function (EEDF) is presented (chapter 5, section 5.5).

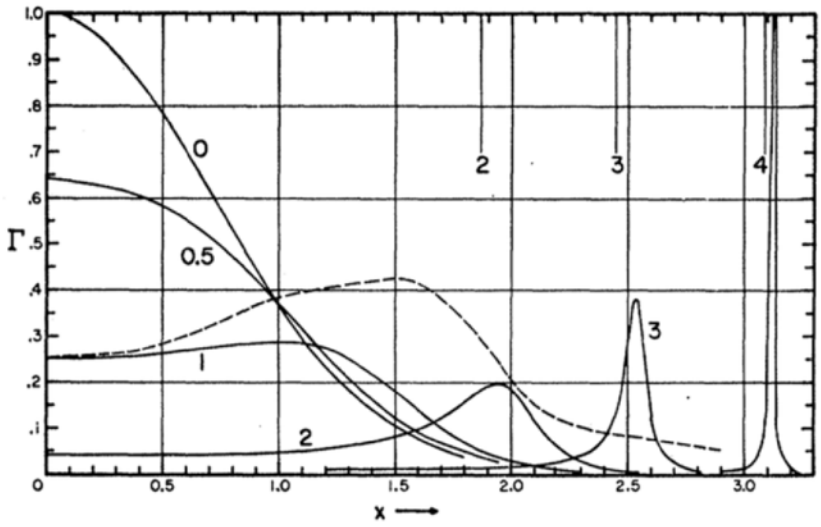

Figure 4.3: Salpeter Spectral function $\Gamma_\alpha(x)$ for α=0, 0.5, 1, 2, 3, 3.5, 4 (values of α are indicated in the plot). From reference [45].

4.3 Comparison of Thomson and Rayleigh Scattering Profiles

As mentioned previously, Rayleigh and Thomson scattering are both quasi-elastic scattering processes, and therefore interfere with one another. Scattering intensity in both cases is proportional to the differential scattering cross section $\left(\frac{d\sigma}{d\Omega}\right)$ and the number density of the scatterers (N).

$$I \propto \frac{d\sigma}{d\Omega} N \tag{4.8}$$

Rayleigh scattering has a cross section $\approx$2 orders of magnitude (depending on the species) smaller than that of Thomson scattering. However, there are several orders

of magnitude more neutral species than free electrons in a nonequilibrium plasma. Depending on the type of plasma (DC, AC, RF, MW, ns-pulse), pressure and discharge power, ionization fractions in nonequilibrium plasmas range from $\approx 10^{-8}$ to 10^{-4} [25]. The net result is that Rayleigh scattering signal intensity is usually 2-4 orders of magnitude stronger than Thomson scattering. However, analysis of the lineshapes yields another important aspect.

As a result of their quasi-elastic nature, at low number density conditions (where pressure broadening is not a significant factor), such as studied in this work, both Rayleigh and incoherent Thomson scattering only produce a wavelength shift in the scattered photon due to the Doppler effect (Doppler broadening). The full-width at half-maximum (FWHM) for Doppler broadening is given as [46],

$$\Delta\nu_D = 2\nu_0\sqrt{\frac{2k_B T ln(2)}{mc^2}} \tag{4.9}$$

where ν_0 is the incident radiation frequency, T is the translational temperature of the particles of interest, and m is the mass of the particles of interest. The two key variables to take note of here are temperature (T) and particle mass (m). As discussed in section 2.1, in nonequilibrium plasmas, electron temperature is much higher compared to that of neutral species temperature (usually by $\approx$2 orders of magnitude). Also, the electron mass is $\approx$5 orders of magnitude lighter than that of neutral species. Both of these factors contribute to a much wider spectral profile for Thomson scattering compared to Rayligh scattering, with the net difference in linewidth being a factor of $\approx$200-1000. Figure 4.4 shows a synthetic spectra comparison of the lineshapes for Rayleigh scattering of N_2 at 300 K and 100 torr, and Thomson scattering for n_e=10^{13} cm^{-3} and T_e=1 eV (typical experimental conditions for data presented

in chapter 5). The Rayleigh intensity is divided by a factor of 5000, indicating its significant advantage in intensity strength compared to Thomson.

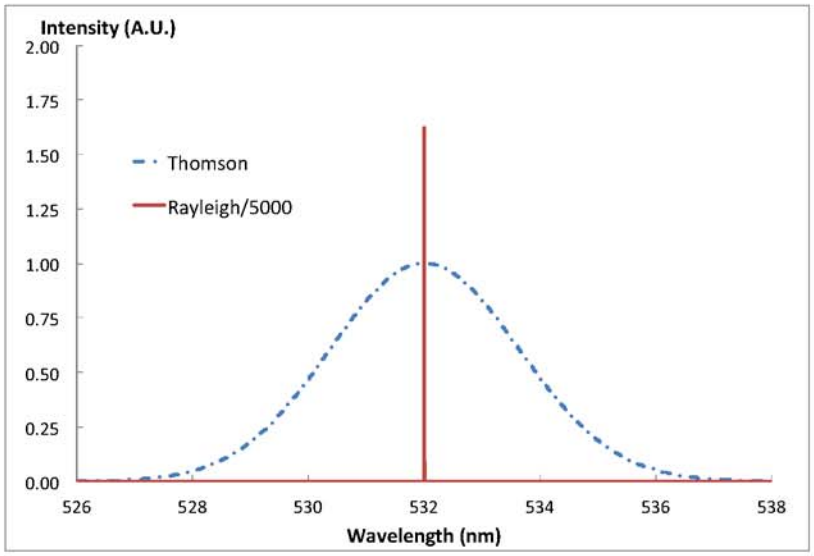

Figure 4.4: Comparison of synthetic spectra for Rayleigh (N_2, 100 torr, 300 K) and Thomson (n_e=10^{13} cm^{-3}, T_e=1 eV) scattering.

It is clear that in order to collect Thomson scattering spectra at these conditions, the Rayleigh scattering will need to be filtered out in some manner. As discussed in chapter 1, two methods are often employed, namely selective absorption filtering and spectral masking. The latter method is used in the experiments presented in chapter 5 and is discussed in more detail in section 4.4.

4.4 Triple-Grating Spectrometer Instrument Design and Implementation

A schematic diagram of the triple grating spectrometer is shown in figure 4.5. The spectrometer design was modeled after a similar device used at Ruhr-University

Bochum, in Germany [19]. The triple grating spectrometer is designed to collect Thomson spectra, while effectively masking Rayleigh scattering signal and mitigating stray light. The spectrometer utilizes two, vertical, micrometer-controlled slits, three identical blazed holographic, plane diffraction gratings (1800 gr/mm, 400 nm blaze), six identical achromatic doublet lenses (D = 63 mm, f = 400 mm), one 2", silver-protected turning mirror, and one custom-machined, stainless steel spectral mask. The achromatic doublet lenses were chosen to mitigate chromatic aberration losses. The gratings have ≈40% efficiency for horizontally polarized light at 532 nm (used for Thomson experiments presented in chapter 5). The groove density was chosen as a balance between spectral resolution and linear dispersion (≈1 mm/nm). Functional and theoretical information about gratings and their use in spectroscopy can be found in reference [47].

The spectrometer functions as follows. A focused, vertical image of collected scattering signal enters the spectrometer through the vertical entrance slit shown in the top-left corner of the schematic. The focused image then expands, and is collimated with an achromatic lens. The image from the slit is then diffracted by the first grating at an incident angle of α_i=14.72^o and a resulting diffraction angle of β_d=44.72^o. This produces a spectrum propagating at 30^o from the incident light direction. Another achromatic lens is then used to focus the spectrum. During focusing, the spectrum is turned by 150^o with a silver-protected mirror. At the focal point, a focused spectrum, with both Rayleigh and Thomson scattering signals overlapping one another is realized. As discussed in section 4.3, the Rayleigh scattering signal is much more intense, but also much more spectrally narrow than the Thomson scattering signal (see figure 4.4). In order to filter out the Rayleigh signal, a spectral mask is utilized, placed

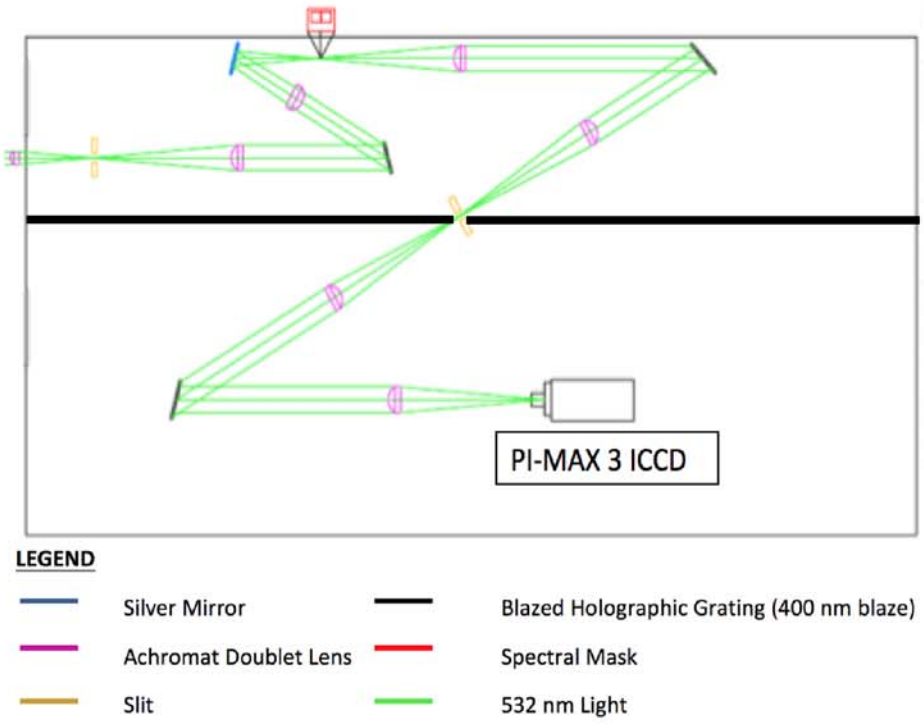

Figure 4.5: Triple-grating spectrometer schematic diagram. From reference [48].

at the focal point. This mask is custom machined out of stainless steel, and has a 1 mm wide, solid strip in the center, surrounded by two rectangular apertures on either side. The mask functions by physically blocking the central portion of the focused scattering spectrum at this location. Thus, when the mask is properly aligned, it effectively blocks the entire Rayleigh scattering signal, as well as the central portion of the Thomson scattering signal, while allowing the 'wings' of the spectrally wider Thomson scattering signal to propagate through the mask. An illustration of this is shown in figure 4.6, where the mask has been made partially transparent.

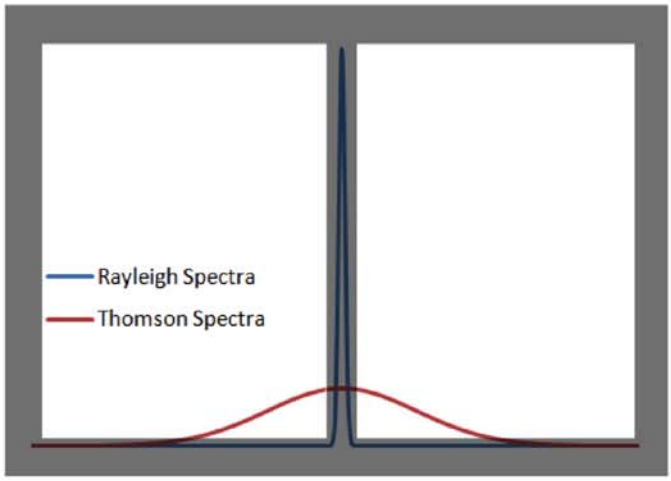

Figure 4.6: Diagram showing the effect of a stainless steel spectral mask on the scattering spectrum through the triple-grating spectrometer.

The remaining Thomson signal, which has passed through the spectral mask, is then re-collimated by another achromatic lens and is subsequently incident upon the second grating (see top-right corner of figure 4.5). This grating is set up (angled) in a 'subtractive' mode, so as to recompress the previously dispersed spectrum back into an image. This image is then focused down, with another achromatic lens, onto a second

vertical slit. The entire spectrometer volume beyond the second slit is partitioned off from the rest of the spectrometer, as shown in figure 4.5. The combination of the second slit and partition acts as an excellent stray light rejector for any light that may have scattered off of surfaces. From this juncture, the rest of the device functions like a conventional, single-grating spectrometer. The image is collimated with another achromatic lens before striking the third grating, which disperses the image back into a spectrum once more. This spectrum is then focused down, with a final achromatic lens, onto a detector. In the experiments presented in chapter 5, the detector used is a PI-MAX 3 ICCD camera.

A sample Thomson scattering spectrum, as collected by the triple-grating spectrometer just described, is shown in figure 4.7 for a nanosecond pulse helium discharge, sustained between two spherical, copper electrodes at a pressure of 200 torr. As can be observed in the figure, the central portion of the Thomson scattering spectrum is missing, as a result of the spectral masking procedure described previously. The sensitivity of the diagnostic allows for collection of Thomson spectra, with S/N $\geq$ 2, down to electron densities of $n_e \approx 1\times10^{12}$ cm^{-3}. Sensitivity could be improved by utilizing higher efficiency gratings or a higher quantum efficiency ICCD camera at the incident wavelength of interest.

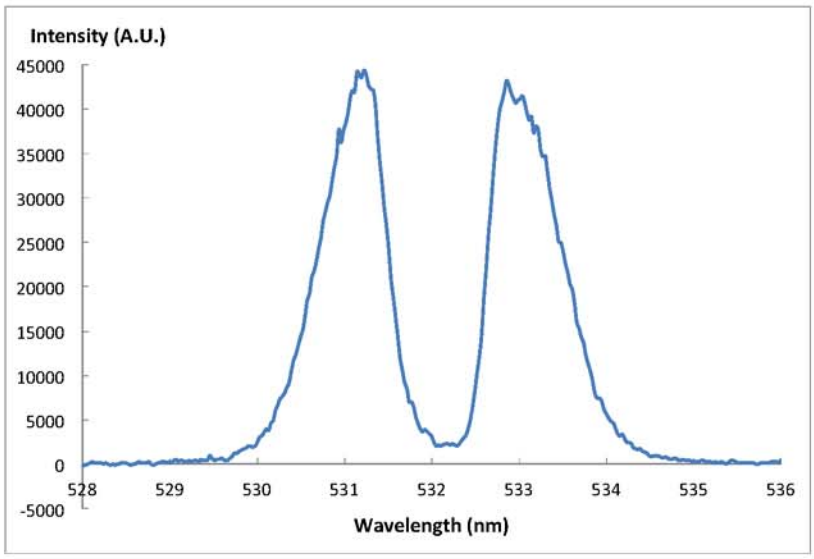

Figure 4.7: Sample Thomson scattering spectrum collected by the triple-grating spectrometer with a stainless steel mask in a nanosecond pulse discharge in helium (P=200 torr).

4.5 Laser Energy Considerations

As mentioned in section 4.1, when collecting Thomson scattering spectra produced using a high-energy pulsed laser, there is potential for optical (laser-induced) breakdown to occur at the focal point. This phenomenon is a result of the strong electromagnetic field of the high energy laser beam causing an electron avalanche at or near the focal point, which results in significant ionization and eventually breakdown. Optical breakdown occurs more readily at higher pressures. If this occurs within the controlled plasma environment between the electrodes of an experiment, the laser is no longer non-intrusive, and can significantly effect the electron density and temperature in the discharge. With the present diagnostic, laser energies exceeding 700 mJ/pulse consistently cause visible optical breakdown at pressures exceeding 100 torr

in nitrogen, air, or helium. In the present experiments, laser pulse energy of less than 600 mJ/pulse was used in all cases. To ensure that optical breakdown is not an issue in the present Thomson scattering measurements, a brief study was conducted, with the diagnostic setup presented in section 4.4, observing the effect of varying laser energy on the extracted Thomson scattering data (electron density, electron temperature and electron energy distribution function). Ideally, no variation should occur, and only signal accumulation times should increase at lower laser energy. Figure 4.8 shows the measured electron density and electron temperature inferred from Thomson scattering spectra gathered at P=200 torr in helium in a sphere-to-sphere, nanosecond pulse discharge, for laser energies of 45 mJ/pulse, 260 mJ/pulse, and 585 mJ/pulse. The latter pulse energy value was used in the experiments presented in chapter 5. For more information on the data reduction procedures, see sections 5.2-5.5.

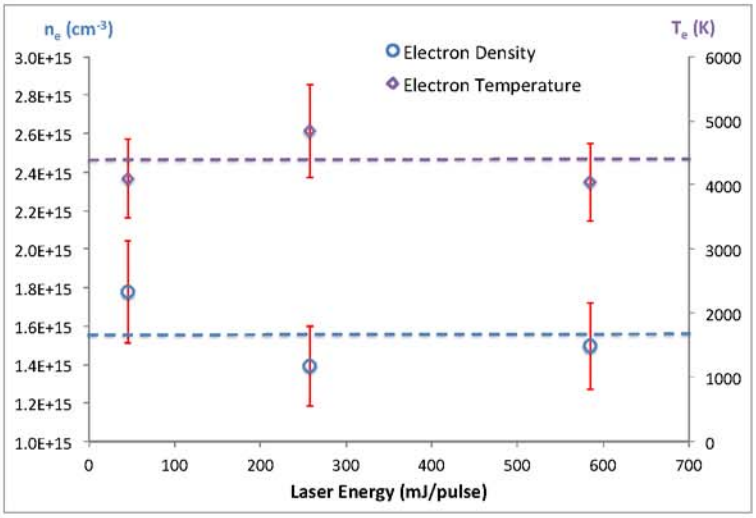

Figure 4.8: Laser-energy resolved electron number density and electron temperature in a nanosecond pulse discharge in helium (P=200 torr, ≈15 mJ/pulse, t = 125 ns after beginning of discharge current pulse).

It can be observed that, while there are minor changes in the measured electron density and electron temperature values for the three laser energies, the changes are within the estimated ≈15% uncertainty of the experiment at these conditions (see sections 5.3 and 5.4). As a result, it is concluded that laser-induced breakdown is not occurring in these experiments. This is further illustrated by comparing electron energy distributions (EEDFs), inferred from the data taken, at the three different laser energies, as shown in figure 4.9. It can be observed that the 45 mJ/pulse and 585 mJ/pulse EEDFs are very nearly identical, while the EEDF inferred at 260 mJ/pulse deviates slightly. This deviation is once again within the estimated uncertainty of the experiment. Furthermore, if optical breakdown were to occur, electron density would increase with laser pulse energy, which is clearly not the case at the present conditions.

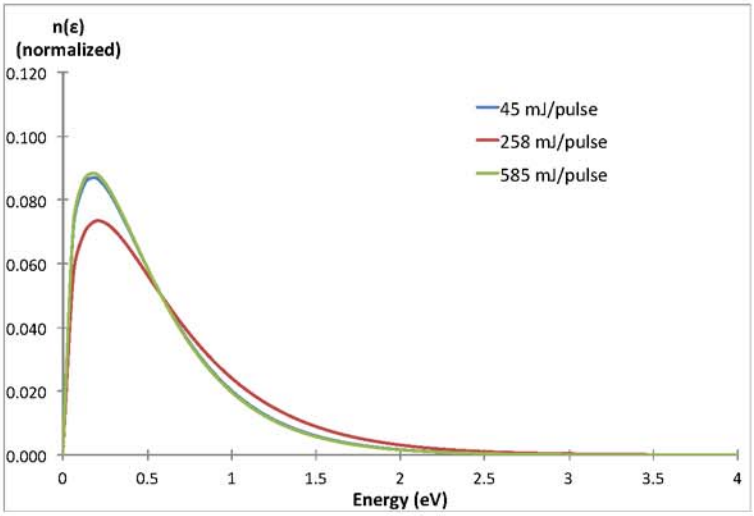

Figure 4.9: Laser-energy resolved EEDFs (assumed to be Maxwellian) for laser pulse energy of 45 mJ/pulse, 258 mJ/pulse and 585 mJ/pulse in a nanosecond pulse discharge in helium (P=200 torr, ≈15 mJ/pulse, t = 125 ns after beginning of discharge current pulse).

Chapter 5: Measurements of Electron Density, Electron Temperature and Inference of Electron Energy Distribution Function

This chapter details the background and results of the time-resolved Thomson scattering experiments that have been conducted. These measurements have been completed in a sphere-to-sphere, single filament discharge as well as a near surface discharge, both of which are sustained by high-voltage, nanosecond duration pulses. Sphere-to-sphere, filament discharge experiments have been conducted in helium, H_2-He, and O_2-He gas mixtures. The near surface discharge has been studied in helium only. Measurements inferred from the Thomson spectra include electron density and electron temperature. Furthermore, electron energy distribution function (EEDF), which is assumed as Maxwellian, has been calculated from the inferred electron density and electron temperature. The chapter begins with a brief summary of the Thomson scattering diagnostic apparatus used in the experiments (section 5.1). Next, the spectral fitting (section 5.2) and data reduction procedures for determining the electron temperature (section 5.3), electron density (section 5.4) and EEDF (section 5.5) are presented. The remainder of the chapter discusses the characteristization, kinetic modeling predictions and results obtained in the two different experiments that were conducted: a diffuse filament, nanosecond pulse discharge sustained between

two spherical electrodes (sections 5.6, 5.7, 5.8) and a near-surface, nanosecond pulse discharge (sections 5.9, 5.10).

5.1 Experimental Apparatus

The Thomson scattering diagnostic used in these experiments utilizes the same, 1.75 m long glass test cell described previously (section 3.3, figure 3.2). Briefly, the cell utilizes Brewster angle, fused silica windows to provide optical access for a vertically polarized, Nd:YAG laser beam, which minimizes stray light generation. The extended length of the cell, combined with a long focal length lens (f=950 mm), which focuses the laser beam at the center of the cell where the discharge is sustained, allows for a high laser pulse energy beam to enter and exit the cell without damaging the windows.

A set of MKS mass flow controllers are used to deliver gas flow to the back end of the cell (with respect to the laser beam direction). Gases are premixed in a plastic delivery line, ≈2 meters long and 1/4" diameter, before entering the cell. The gas mixture composition, as well as the total flow rate, are controlled by the individual mass flow controllers. The flow exhausts from the front end of the cell (with respect to the laser beam direction) to a vacuum pump system. Pressure in the cell is controlled by a ball valve located in the exhaust line leading to the vacuum pump, which effectively controls the pumping capacity. Total pressure in the cell is monitored below the discharge in the center of the cell by an Omega digital pressure gauge.

Figure 5.1 shows a schematic of the entire Thomson scattering experimental apparatus used in the present experiments. The experiment uses a frequency doubled (532 nm, 30 Hz, 10 ns FWHM) Nd:YAG laser as the pump source. A laser energy of ≈600

mJ is used in the present experiments. The laser is focused into the glass test cell, to a beam waist of ≈60 μm, at a point centrally located within the discharge, which is sustained between two electrodes in the center of the glass cell. An achromatic doublet lens (D = 31.5 mm, f = 200 mm) is used to collect the scattered light at a 90 degree scattering angle from the direction of laser beam propagation. The collected image is then sent through an image rotator (a series of three silver protected mirrors), which rotates the collected light from a vertically polarized, horizontal image, to a horizontally polarized, vertical image. The horizontal polarization maximizes the light collection efficiency of the diagnostic based on the efficiencies of the diffraction gratings in the triple-grating spectrometer. The rotated image is then focused down onto a vertical entrance slit (≈40 μm) of the triple-grating spectrometer with a second achromatic doublet lens (D = 31.5 mm, f = 200 mm). The triple grating spectrometer then diffracts the collected image into a Thomson scattering spectrum, while also filtering out interference from elastic Rayleigh scattering (through the use of a spectral mask), as well as stray light. This process is described in greater detail in section 4.4. Collection of the filtered Thomson scattering spectrum is done by a PI-MAX 3 ICCD camera at the end of the spectrometer.

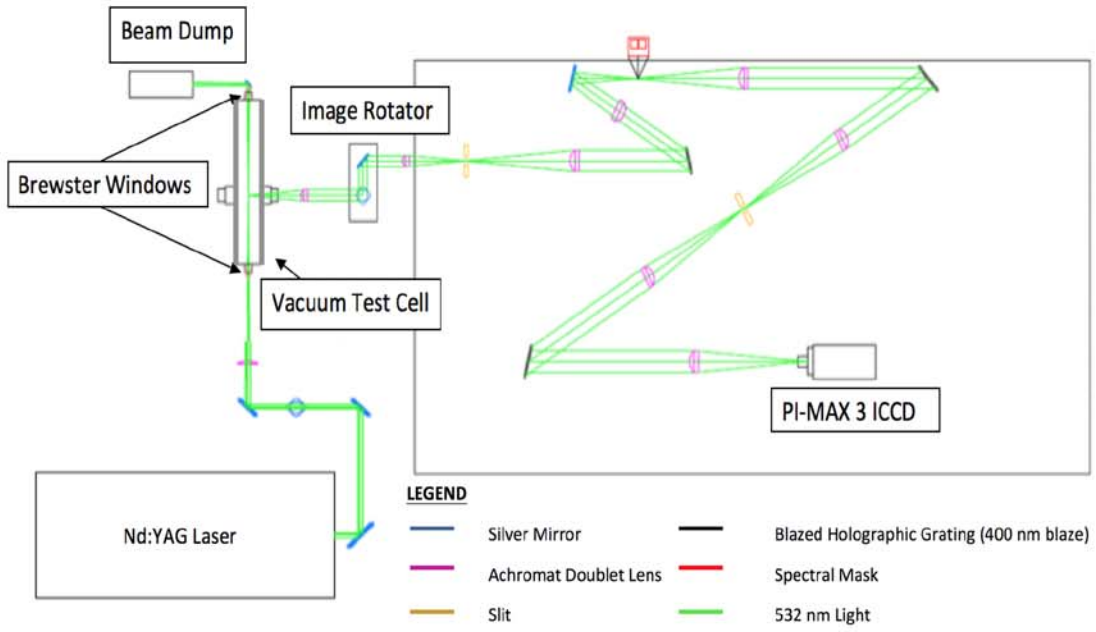

Figure 5.1: A schematic of the Thomson scattering experimental apparatus, with triple-grating spectrometer. From reference [48].

5.2 Fitting the Raw Thomson Scattering Spectra

Figure 5.2 shows a sample Thomson scattering spectrum (blue), collected using the diagnostic described previously (section 5.1). Similar to the collection of the vibrational Raman spectra in section 3.5, the Thomson spectra are collected through a two-stage process, with additional background subtraction due to plasma emission. First, a single 'exposure' is created by collecting Thomson scattering signal from a large number of individual laser shots and summing them together (i.e. accumulating them on an ICCD camera chip). Next, several of these 'exposures' are collected in succession and then averaged. Both processes improve the signal-to-noise ratio (S/N), with the former increasing it linearly with number of laser shots and the latter

increasing it proportional to the square-root of the number of exposures. The averaging process is done in addition to the laser shot accumulation process to further improve S/N without saturating the camera during collection of a single 'exposure'. In the end, both S/N and signal collection time need be taken into account, and a reasonable trade-off between the two parameters determined. For these experiments, the number of laser shots collected per 'exposure' varied between 9,000 and 45,000, and was chosen individually for each spectrum collection point (i.e. delay time after the pulse) to maximize S/N without saturating the detector. The number of 'exposures' averaged together was four, and was chosen as a trade-off between further S/N improvement and overall signal collection time. For more details on the data collection values used in the experiments, see tables 5.2 and 5.3 in section 5.6 for the sphere-to-sphere filament discharge experiments in H_2-He and O_2-He, respectively, and section 5.9 for the near surface discharge experiment in helium.

Similar to the vibrational spectra collection in section 3.5, all of the Thomson scattering spectra were collected from a 2.75 mm long, ≈60 μm diameter volume of the discharge. Camera pixels for this interrogation region were binned together before reading out the spectrum, thus the data are spatially averaged over this region. Once the raw Thomson scattering spectrum has been collected (through the procedure described above), a previously taken background spectrum of the broadband plasma emission is subtracted from it, yielding the background-corrected Thomson scattering spectrum, like the one shown in blue in figure 5.2. Note the missing, central portion of the spectrum; due to the masking procedure used in the triple grating spectrometer to filter interference from Rayleigh scattering (see section 4.4).

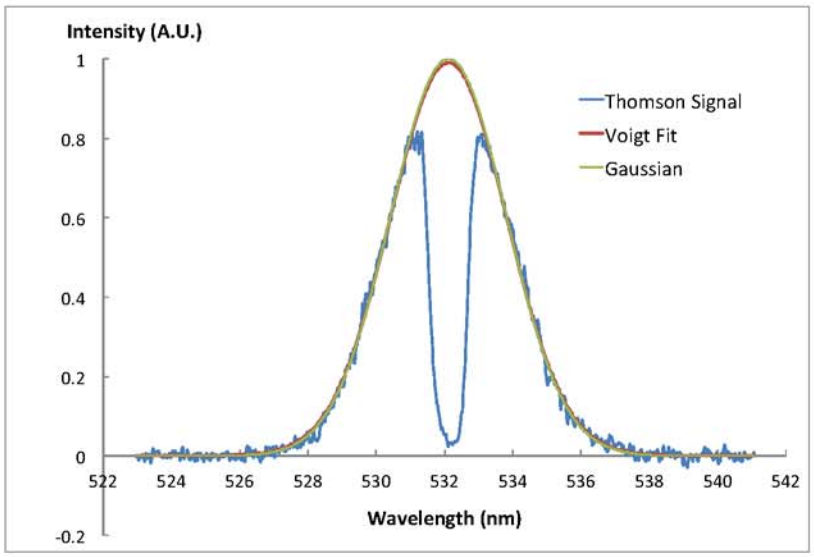

Figure 5.2: Sample Thomson scaterring spectrum (He, P=200 torr, 80 ns after start of discharge current pulse), shown with least-squares Voigt fit and inferred Gaussian profile. From reference [49].

Once the Thomson scattering spectrum has been collected, it is used as input data by a set of custom-written, MATLAB data reduction computer codes. The first stage of the data reduction is to fit the Thomson scattering spectrum with a Voigt profile, using a least-squares fitting procedure, shown in red in figure 5.2. The Voigt profile is a convolution of the Lorentzian instrument function (collected using a neon lamp source) and an adjustable parameter Gaussian function, representing the Thomson contribution to the lineshape broadening. The use of a Gaussian distribution for the Thomson scattering spectrum is valid only in plasmas where electrons have a Maxwellian velocity distribution, as is the case in the present experiments (see discussion in sections 4.2, 5.5). Once the experimental spectrum has been fit by the Voigt profile, the Gaussian (i.e. Thomson scattering) contribution can be isolated from the convolved lineshape; this is shown in green in figure 5.2. From figure 5.2 it

can be seen that the Gaussian (Thomson) and the Voigt fits are nearly identical, indicating that the instrument function accounts for a very small fraction of the observed spectral broadening.

5.3 Electron Temperature Inference

The electron temperature is determined directly from the half-width at half-maximum (HWHM) of the Thomson scattering (Gaussian) spectral profile. Since in the case of a Maxwellian electron velocity distribution, the Thomson spectrum is Doppler broadened, electron temperature is calculated from the Doppler HWHM, evaluated from the overwhelmingly dominant Gaussian contribution of the least-squares Voigt profile fitting procedure. The Doppler HWHM is given by,

$$\Delta\nu_D^{'} = \frac{2\nu_0}{c_0}\sqrt{\frac{2ln(2)k_BT_e}{m_e}}sin\left(\frac{\theta}{2}\right) \tag{5.1}$$

where ν_0 is the frequency of the incident laser radiation, T_e is electron temperature, m_e is the electron mass, and θ is the scattering angle (90^o). The uncertainty of the electron temperature measurements, arising from uncertainty of the FWHM ($\delta\Delta\nu_D^{'}$) of the Thomson scattering spectrum can be calculated as follows,

$$\delta T_e = \frac{m_e}{2ln(2)k_B}\left(\frac{c_0}{\nu_0}\right)^2\left(\delta\Delta\nu_D^{'}\right)^2 \tag{5.2}$$

Since the signal-to-noise for the Thomson scattering spectrum is a direct function of the electron number density, the electron density value for a given spectrum dictates the uncertainty of the measurement, with lower electron densities yielding higher uncertainties. In general electron temperature uncertainty ranged from 0.01% to 8%. For $n_e \approx 10^{15} - 10^{16}$ cm^{-3}, $\delta T_e/T_e = \pm$0.01-0.2%. For $n_e \approx 10^{14} - 10^{15}$ cm^{-3}, $\delta T_e/T_e = \pm$0.1-1.5%. For $n_e \approx 10^{13} - 10^{14}$ cm^{-3}, $\delta T_e/T_e = \pm$1-8%.

It should be noted that statistical uncertainty (i.e. precision) of the electron temperature measurement is not analyzed here. Taking repeated measurements, required for this analysis, is not feasible, since signal collection time for a single spectrum may exceed 4 hours.

5.4 Electron Number Density Inference

The electron density is inferred from the integrated intensity of the collected scattering spectrum (i.e. from the fitted Voigt profile). However, the absolute scattering intensity must be calibrated by the scattering intensity from a spectrum with a known population and scattering cross-section. For this work, the $J = 6 \rightarrow 8$, pure rotational Raman transition of nitrogen at 532 nm is used. The absolute electron number density is then obtained as,

$$n_e = \frac{A_e}{A_{N_2}} \frac{\left(\frac{d\sigma_{N_2}}{d\Omega}\right)_{532nm}}{\left(\frac{d\sigma_e}{d\Omega}\right)} n_{N_2} f_{J=6} \tag{5.3}$$

where A_e is the integrated Thomson scattering intensity, A_{N_2} is the integrated $J = 6 \rightarrow 8$ pure rotational Raman scattering intensity, $\left(\frac{d\sigma_{N_2}}{d\Omega}\right)_{532nm}$ is the known differential rotational Raman cross section for N_2 at 532 nm (3.82×10^{-30} cm^2/sr), $\left(\frac{d\sigma_e}{d\Omega}\right)$ is the differential Thomson scattering cross section (7.94×10^{-26} cm^2/sr for vertically polarized light at θ=90^o), n_{N_2} is the number density of nitrogen as determined from the equation of state for an ideal gas at T=300 K, and $f_{J=6}$ is the fraction of the N_2 molecules residing in the $J = 6$ rotational state (from the Boltzmann rotational distribution, using a rigid-rotor approximation).

A_{N_2} is obtained by integrating a pure rotational Raman spectrum collected in N_2, using the same diagnostic setup as described in chapter 4 and section 5.1. The same

pressure as in the Thomson scattering experiments is used, and a correction factor is used in the data reduction code to account for the difference in signal collection time used for Raman scattering vs. Thomson scattering. Figure 5.3 shows a typical, pure rotational Raman spectrum collected in 100 torr of N_2, over a 5 minute signal collection time. To obtain the integrated Raman scattering intensity from the spectrum, a similar, least-squares fitting procedure to that used in the Thomson spectra fitting was used for the $J = 6 \rightarrow 8$ transition.

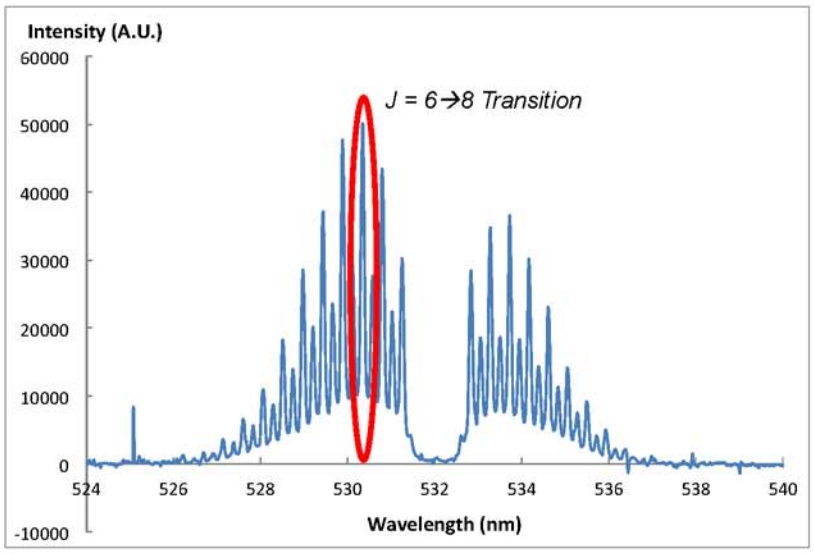

Figure 5.3: A pure rotational Raman scattering spectrum used for Thomson scattering intensity calibration (N_2, P=100 torr, 5 minute accumulation time).

The uncertainty of the electron number density arising from the uncertainty of the integrated intensity of the Thomson scattering spectrum (δA_e) can be calculated

as follows,

$$\delta n_e = \frac{1}{A_{N2}} \frac{\left(\frac{d\sigma_{N2}}{d\Omega}\right)_{532nm}}{\left(\frac{d\sigma_e}{d\Omega}\right)} n_{N_2} f_{J=6} \delta A_e \tag{5.4}$$

Note that the uncertainty arising from A_{N_2} and $\left(\frac{d\sigma_{N2}}{d\Omega}\right)_{532nm}$ are neglected since they are small compared to δA_e. Since the signal-to-noise is a direct function of the electron number density, the electron density value for a given spectrum dictates the uncertainty of the measurement, with lower electron densities yielding higher uncertainties. In general, electron number density uncertainty, $\delta n_e/n_e$ ranged from 2% to 30%. For $n_e \approx 10^{15} - 10^{16}$ cm^{-3}, $\delta n_e/n_e = \pm$2-4%. For $n_e \approx 10^{14} - 10^{15}$ cm^{-3}, $\delta n_e/n_e = \pm$5-12%. For $n_e \approx 10^{13} - 10^{14}$ cm^{-3}, $\delta n_e/n_e = \pm$15-30%.

It should be noted that, similar to the electron temperature measurements, statistical uncertainty (i.e. precision) of the electron number density measurements is not analyzed here. This is because the repeated measurements required for this type of analysis would require excessively long collection times (signal collection times in excess of 4 hours per spectrum in some instances).

5.5 Inferring the Electron Energy Distribution Function

As discussed previously in section 4.2, in the limit where the Salpeter parameter (see eqn. 4.5) approaches zero ($\alpha \to 0$), the Thomson scattering is entirely incoherent, and if a Maxwellian velocity distribution for the electrons is realized, a Gaussian Thomson scattering spectrum results. This approach is often valid for $\alpha \ll 1$, or $\alpha \lesssim 0.1$, which roughly corresponds to electron densities in the range of 10^{12} cm$^{-3} \leq n_e \leq 10^{17}$ cm^{-3}. However, it has been shown in the literature that for many gas discharge plasmas, the electron velocity distribution is not Maxwellian [25]. For instance, at

low electron number densities ($n_e < 10^{12}$ cm^{-3}), electron-electron collisions become very rare, and inelastic electron-neutral collisions dominate, such that electron energy distribution function is strongly non-Maxwellian. This has been studied by Thomson scattering in low pressure RF discharges [50].

In molecular gases, cross sections of inelastic electron-neutral collisions may be very large, comparable to the total electron-neutral cross section. To illustrate this, figure 5.4 shows the total electron-neutral scattering cross section in nitrogen. It can be observed that the total cross section is up to $30 \cdot 10^{-16}$ cm^2. Comparing this to figure 5.5, which shows a single vibrational excitation cross section in N_2 ($v = 0 \rightarrow 1$), it can be seen that even for a single vibrational excitation in nitrogen, the cross section is up to $5 \cdot 10^{-16}$ cm^2; or approximately 15% of the total electron-neutral cross section. Furthermore, figure 5.6 shows several electronic excitation cross sections in nitrogen, each of which are up to ≈1% of the total electron-neutral cross section. From an analysis of these figures, it is clear that inelastic electron collisions may be of significant importance.

Figure 5.7 plots the exponential portion ($n(\epsilon)/(n_e\sqrt{\epsilon})$) of the electron energy distribution function (EEDF) in nitrogen, calculated theoretically by solving the Boltzmann equation (which uses experimental electron-neutral collision cross sections as input) for electrons in a DC field plasma over a wide range of reduced electric field (E/N) values. In this semi-log plot, a Maxwellian EEDF would be a straight line. It can be seen, however, that these EEDFs deviate considerably from a Maxwellian distribution. This is primarily due to inelastic e-V collisions, whose cross sections, in the energy range of ≈1-3 eV, are very high (see figure 5.5), resulting in a precipitous drop in the EEDF. At high E/N, this deviation becomes less pronounced since

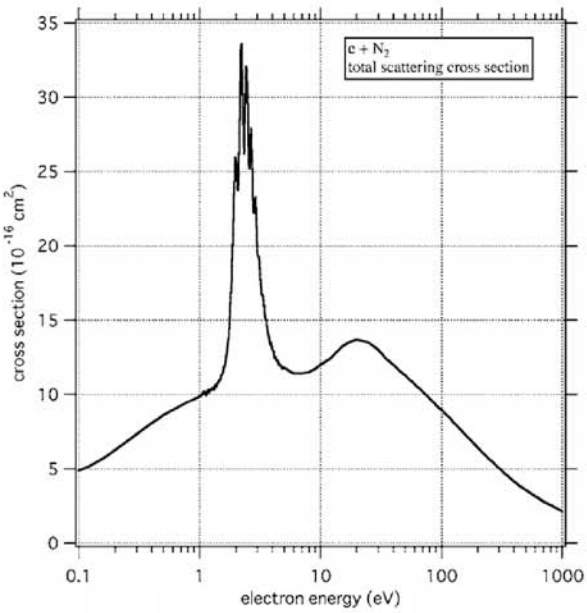

Figure 5.4: Total electron-neutral scattering cross section in N_2. From reference [51]

electrons gain energy from the electric field more rapidly and elastic collisions begin to dominate. In the present experiments, reduced electric field strength during the nanosecond pulse is ≈100-300 Td. At such high E/N values, the EEDF approaches a Maxwellian distribution, even in molecular gases, as can be seen from figure 5.7.

Another kinetic consideration which causes the EEDF to approach a Maxwellian distribution can occur at high electron densities, which causes Coulomb (electron-electron) collisions to become more frequent. Note that even in this case the electron temperature in the plasma exceeds the gas temperature considerably. This occurs because e-e collisions conserve both electron momentum and energy, while electron energy loss in elastic collisions with neutral species is quite inefficient. The ionization fraction at which e-e collisions start to strongly affect the EEDF can be analyzed by

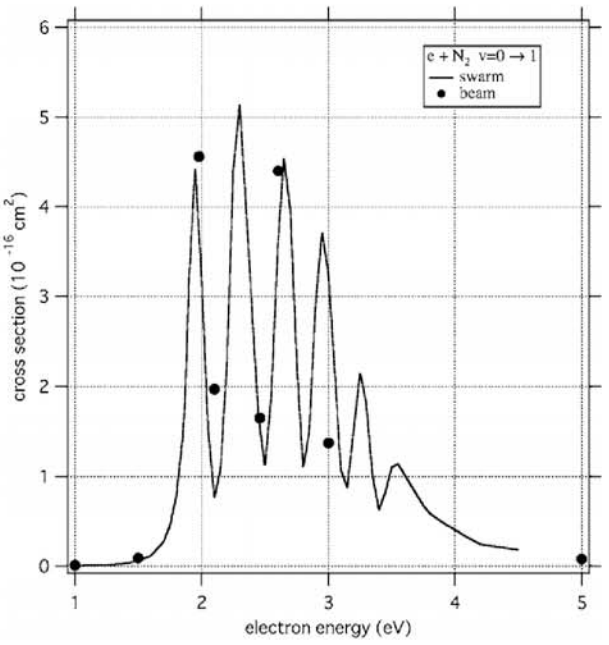

Figure 5.5: Electron impact vibrational excitation cross section ($v = 0 \rightarrow 1$) for N_2. From reference [51]

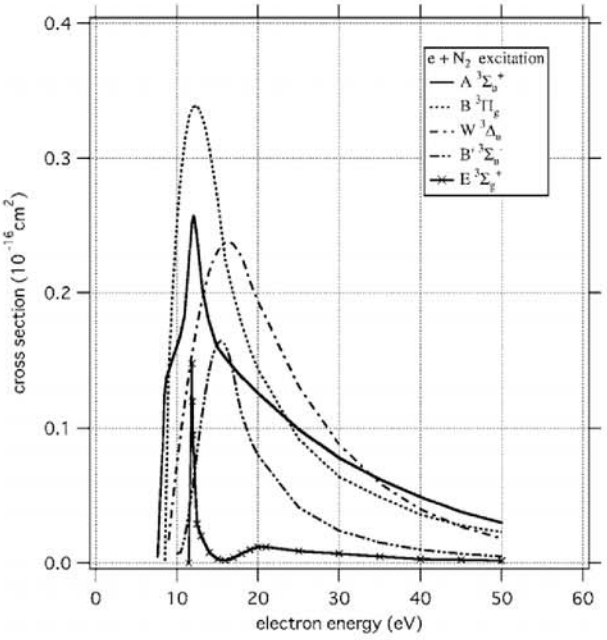

Figure 5.6: Electron impact electronic excitation cross sections for N_2. From reference [51]

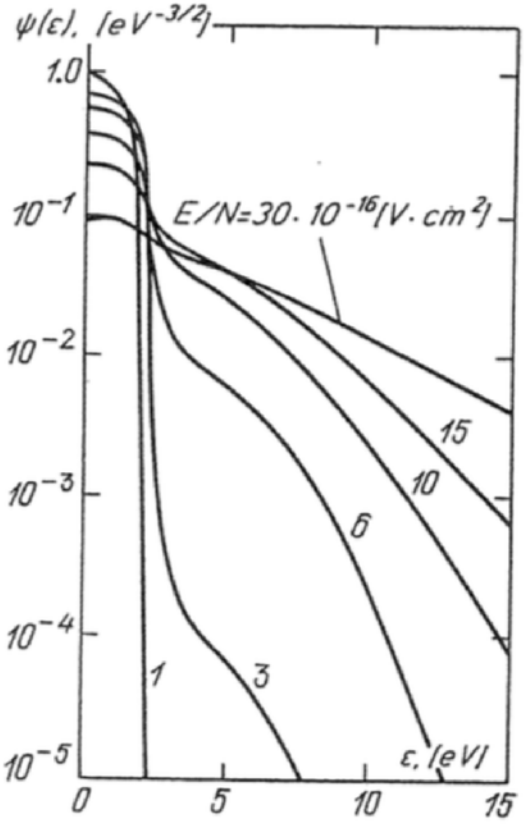

Figure 5.7: Exponential part $(n(\epsilon)/(n_e\sqrt{\epsilon}))$ of the electron energy distribution function (EEDF) in nitrogen in a DC field for several reduced electric field (E/N) values. From reference [25]

comparing the electron-electron (e-e) and electron-neutral (e-N) collision rates,

$$-\sigma_{ee} n_e^2 \sim -\sigma_{eN} n_e N \tag{5.5}$$

where n_e is electron density, N is number density of neutral species, σ_{eN} is the electron-neutral collision cross section and σ_{ee} is the e-e collision cross section, or Coulomb cross section for electron-electron interactions, given as [25],

$$\sigma_{ee} = \sigma_{coul} = \pi r_{coul}^2 = \pi \left(\frac{2}{3} \frac{e^2}{k_B T_e} \right)^2 \tag{5.6}$$

For $T_e = 1$ eV, $\sigma_{ee} \approx 10^{-13}$ cm^2. Canceling electron density on each side of eqn. 5.5 and rearranging yields,

$$\frac{n_e}{N} = \alpha \sim \frac{\sigma_{eN}}{\sigma_{ee}} \sim \frac{\approx 10^{-15} - 10^{-16} cm^2}{\approx 10^{-13} cm^2} \sim \approx 10^{-2} - 10^{-3} \tag{5.7}$$

where σ_{eN} is $\approx 10^{-15}$ cm^2 for molecular neutral species and $\approx 10^{-16}$ cm^2 for atomic neutral species. Thus, at lower ionization fractions ($\alpha < 10^{-2} - 10^{-3}$), inelastic collisions may well distort the shape of the EEDF from Maxwellian significantly.

Another cause of deviation from the Maxwellian velocity distribution can occur when conducting experiments in the coherent Thomson scattering regime ($\alpha \gtrsim 0.1$, $n_e > 10^{17}$ cm^{-3}). At such extremely high electron number densities, which can be achieved in a laser spark plasma, ion contribution to the scattering signal becomes very important, and sidebands appear in the Thomson scattering spectrum (see figure 4.3). The sidebands are a result of strong electron-ion interactions, which cause fluctuations in the charge density of the plasma. However, these high electron densities are not usually achieved in nonequilibrium gas discharge plasmas.

In summary, a wide range of electron velocity distributions can be realized in gas discharge plasmas, based on a variety of factors, resulting in correspondingly different Thomson scattering lineshapes. This has been theoretically studied by Brown and Rose in 1966 [52], where they analyzed relationships between a wide variety of electron velocity distributions and Thomson scattered spectra. Figure 5.8 shows different spectral (Thomson scattering) shape functions calculated for different electron velocity distribution functions. It can be clearly seen that for all spectral distributions shown, only the tail significantly depends on the electron velocity distribution. Thus, only the 'wings' of the Thomson scattering spectrum are expected to be affected by the shape of the EEDF.

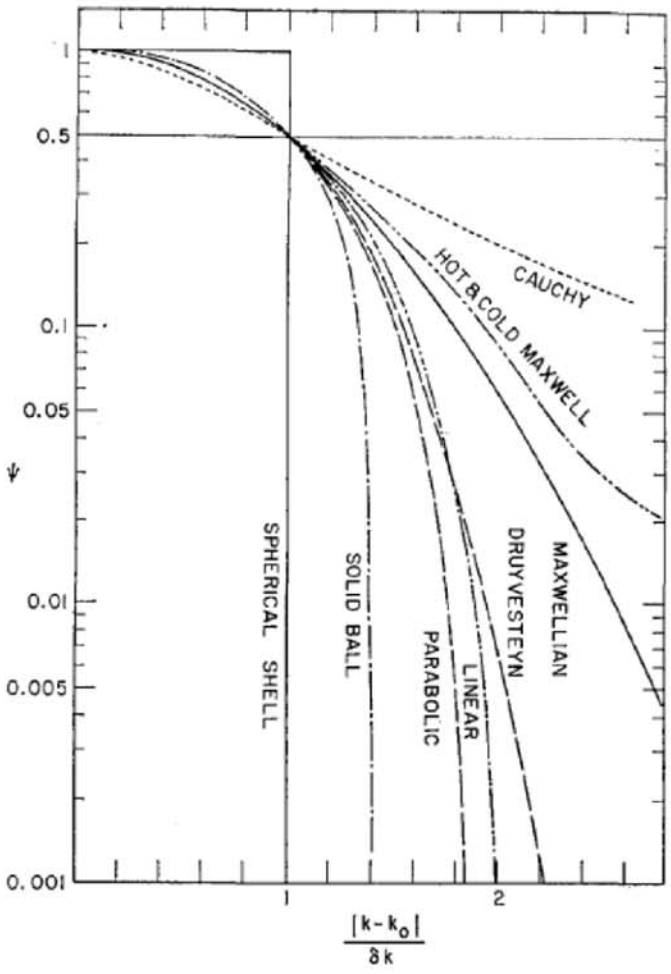

Figure 5.8: Thomson scattering spectral shape functions for several types of electron energy distribution functions. From reference [52]

The studies presented in this dissertation all correspond to low values of the Salpeter parameter, $\alpha \leq 0.08$ and fairly high electron densities ($n_e \geq 10^{13}$ cm^{-3}). As a result, it is expected that deviation from Maxwellian electron velocity distribution would not be significant. In inert gases, experimental EEDFs, if not Maxwellian, often closely resemble a Druyvesteyn distribution [25]. The difference between these two theoretical distributions is due to one underlying assumption. In the Maxwellian distribution, it is assumed that the electron collision frequency is independent of electron energy, whereas in the Druyvesteyn distribution, it is assumed that the mean free path length of the electrons is independent of energy. This difference causes an error function type Thomson scattering spectrum to occur of the following form [52],

$$a\left(1 - erf\left[0.474\left(\frac{\mathbf{k}_s - \mathbf{k}_0}{\Delta\nu'}\right)^2\right]\right) \tag{5.8}$$

where a is the peak height, $\mathbf{k}_s$ is the scattered wave vector, $\mathbf{k}_0$ is the incident wave vector, and $\Delta\nu'$ is the half-width at half-maximum (HWHM). This function for the scattering spectrum is in contrast to the Maxwellian case, which produces a Gaussian lineshape of the following form [52],

$$a\exp\left[-ln(2)\left(\frac{\mathbf{k}_s - \mathbf{k}_0}{\Delta\nu'}\right)^2\right] \tag{5.9}$$

The resulting difference in the electron energy distribution (EEDF) is shown in figure 5.9.

The procedure for inferring the EEDF from the Thomson scattering spectrum is outlined in the following sections.

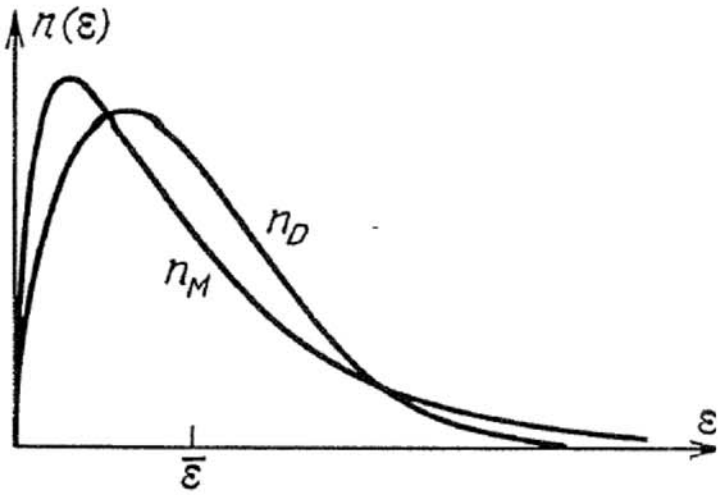

Figure 5.9: Maxwell (n_M) and Druyvesteyn (n_D) energy distribution functions for same mean energy $\bar{\epsilon}$. From reference [25].

5.5.1 Maxwellian Distribution

If a Thomson scattering spectrum is accurately represented by a Gaussian distribution, a Maxwellian electron velocity distribution is present [52]. Then, using the electron temperature inferred from the FWHM of the Thomson scattering spectrum (see section 5.3), the exponential portion of the EEDF can be calculated from the following equation [25],

$$f_0 = C \exp\left[-\frac{3m_e^2(\omega^2+\nu_m^2)}{Me^2E^2}\frac{m_e v^2}{2}\right] = C\exp\left[-\frac{\epsilon}{k_B T_e}\right] \tag{5.10}$$

where T_e is electron temperature, given as,

$$T_e = \frac{Me^2E^2}{3m_e^2(\omega^2+\nu_m^2)} \tag{5.11}$$

where ϵ is electron energy, ω is the electric field frequency, ν_m is the electron-neutral collision frequency, M is the neutral species mass, e is electron charge, E is the

electric field ($E = E_0 sin(\omega t)$), and v is the electron velocity. Equation 5.10 gives the exponential portion of the Maxwellian velocity and energy distribution.

C in equation 5.10 is an integration constant, which is determined from the following normalization condition,

$$2\pi \left(\frac{2}{m_e}\right)^{3/2} \int_0^\infty \sqrt{\epsilon} f_0(\epsilon) d\epsilon = n_e \tag{5.12}$$

where n_e is the electron number density inferred from the integrated Thomson scattering intensity (see section 5.4). The full EEDF, including the pre-exponential factor, is given by,

$$n(\epsilon) = 2\pi \left(\frac{2}{m_e}\right)^{3/2} \sqrt{\epsilon} f_0(\epsilon) \tag{5.13}$$

5.5.2 Druyvesteyn Distribution

If the Thomson scattering spectrum is accurately represented by an error function, a Druyvesteyn electron-velocity distribution is present [52]. Inferring the EEDF in this case would be identical to the procedure outlined for inferring a Maxwellian EEDF, with the exception that the exponential portion of the EEDF would be calculated from the following expression [25],

$$f_0 = C \exp\left[-\frac{3m_e^3}{4Me^2E^2l^2}(v^4 + 2v^2\omega^2 l^2)\right] = C \exp\left[-\frac{3m_e}{M}\frac{\epsilon^2}{\epsilon_0^2}\right] \tag{5.14}$$

where l is the electron mean free path length, and $\epsilon_0 = eEl$ is the energy gained by an electron over one free path length. After the distribution function is inferred from the Thomson scattering spectrum, the normalization condition (equation 5.12) can be applied to obtain the integration constant. The full EEDF, with the pre-exponential factor, is then given by equation 5.13.

To verify that the electron energy distribution function at the present conditions is Maxwellian, a representative Thomson spectrum, taken in a nanosecond pulse discharge in helium (P=200 torr), was fitted with a least-squares fitting procedure with both a Gaussian lineshape (Maxwellian EEDF) and error function lineshape (Druyvesteyn EEDF). The result is shown in figure 5.10. It is clear from the figure that the Thomson scattering spectrum is represented more accurately with a Gaussian lineshape, indicating that a Maxwellian electron velocity distribution is indeed present in the plasma. All of the EEDFs obtained in the present experiments were inferred from Thomson scattering spectra using the procedure outlined above.

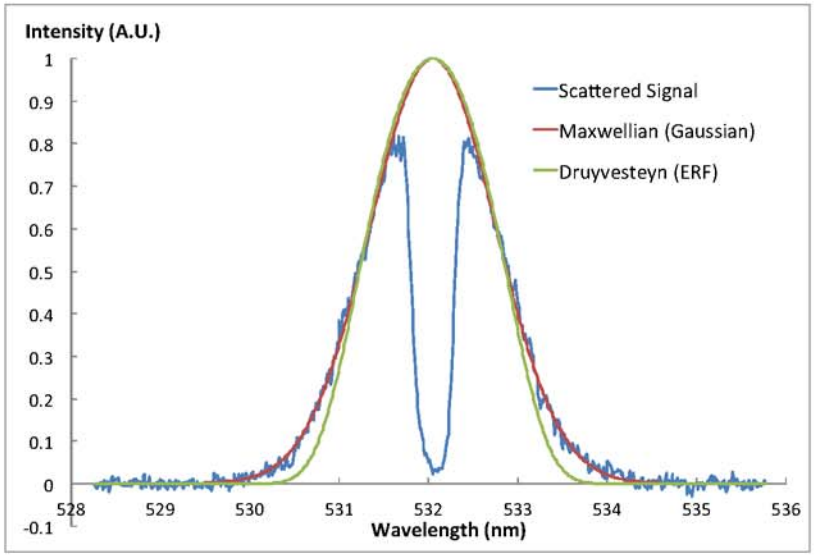

Figure 5.10: Gaussian fit (Maxwellian EEDF) and error function fit (Druyvesteyn EEDF) of experimental Thomson scattering spectrum taken in a sphere-to-sphere, nanosecond pulse discharge in helium (P=200 torr, $n_e \approx 3 \cdot 10^{15}$ cm^{-3}).

Assessing this fit in more detail, it can be shown that approximately 99.9% (.999) of the area under the Thomson scattering spectrum is accurately represented by

a Gaussian fit. This result is consistent for all data sets presented in this work (area represented accurately by Gaussian fits ranged from 99.6 to 99.9%). Since the central portion of the Thomson scattering spectrum corresponds to the lower energy electrons in the EEDF, and the wings of the Thomson spectrum correspond to the higher-energy tail of the EEDF, it can be concluded from this analysis that a Maxwellian electron energy distribution is present down to a relative population of approximately 10^{-3}. Due to uncertainty of the measurements, the present results do not provide information on EEDF behavior at relative populations below $\approx 10^{-3}$.

5.6 Nanosecond Pulse Discharge Sustained Between Spherical Electrodes: Experimental Conditions

The first set of Thomson scattering experiments was conducted in a diffuse, single-filament, nanosecond pulse discharge sustained between two spherical copper electrodes. Studies were conducted in a discharge with high coupled pulse energy (≈17 mJ/pulse) in helium, as well as in discharges with moderate coupled pulse energy (≈4-5 mJ/pulse) in H_2-He and O_2-He mixtures.

5.6.1 Nanosecond Pulse Discharge Sustained Between Spherical Electrodes: Pulse Characteristics

Figure 5.11 shows a photograph of the sphere-to-sphere electrode setup used in these studies. This is essentially the same setup as used in the previous spontaneous Raman scattering, N_2 vibrational level population studies (chapter 3). The electrodes are made of copper, with spherical tips, 7.5 mm diameter with a 1 cm gap between the electrodes. All Thomson scattering measurements were taken on the discharge centerline, midway between the electrodes. All of the following studies utilized the

same magnetic compression, high-voltage, nanosecond pulse generator as described previously (section 3.3). The pulser is capable of producing pulses with ≈18 kV peak voltage and ≈125 ns duration, at repetition rates of up to 10 kHz. In the following experiments, the pulser was operated at 90 Hz in order to produce a stable, reproducible, single diffuse filament discharge.

Figure 5.11: Photograph of sphere-to-sphere, copper electrode setup (electrode diameter = 7.5 mm, discharge gap = 1 cm)

Helium

Figure 5.12 shows voltage, current and coupled energy waveforms of the discharge used in the high coupled energy (17 mJ/pulse) measurements in helium. Peak voltage is ≈10 kV, while peak current is ≈50 A, achieved approximately 60 ns after the start of the current rise. Current pulse duration is ≈125 ns. An important feature

to note about these waveforms is the presence of a second (weaker) pulse starting approximately 600 ns after the beginning of the primary pulse. This is a feature of the high-voltage pulser, and is consistently reproducible. As a result of this 'secondary' pulse, a small amount of additional energy is coupled to the plasma after the 'primary' pulse. The total energy coupled to the discharge is ≈17 mJ/pulse, with 15 mJ coupled by the primary pulse, and 2 mJ coupled by the secondary pulse.

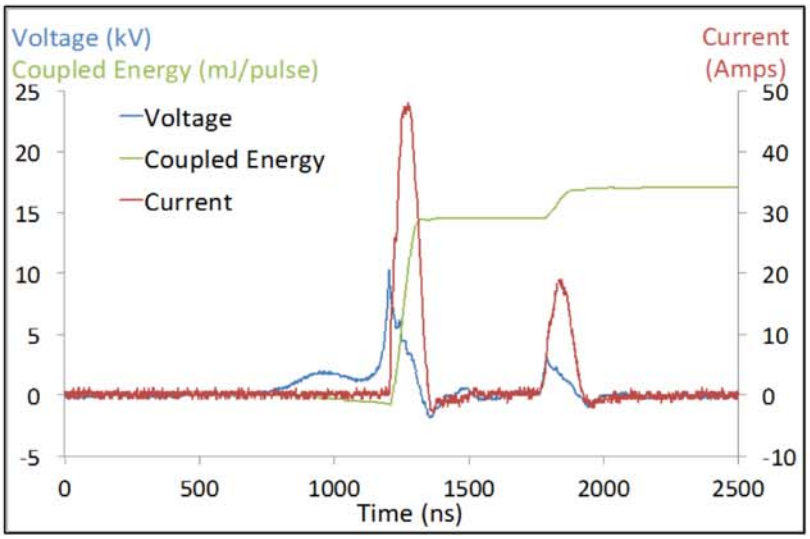

Figure 5.12: Voltage, current and coupled energy waveforms for pure helium study (P=200 torr). From reference [49].

Figure 5.13 shows an ICCD camera image of the broadband plasma emission in helium (at the conditions of figure 5.12), with emission during the primary pulse shown on the left and during the secondary pulse on the right. Both images are 100-pulse averages, illustrating the production of a stable, diffuse, single filament discharge. The primary pulse filament is ≈3 mm in diameter (FWHM) midway between the electrodes, while the secondary pulse produces a somewhat more constricted filament

of ≈2 mm diameter midway between the electrodes (likely due to residual ionization remaining in the discharge gap from the primary pulse).

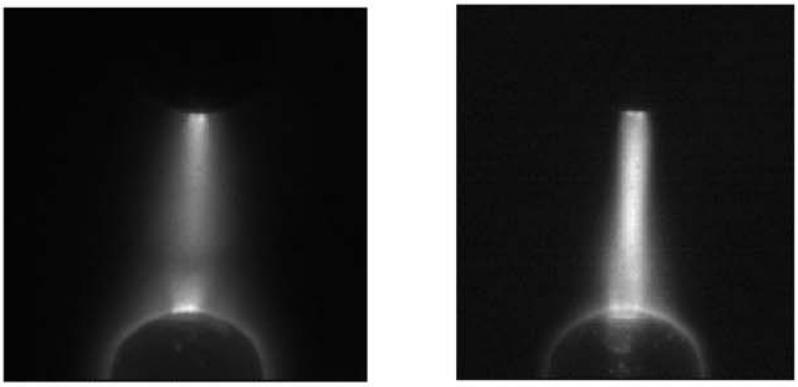

Figure 5.13: Broadband plasma emission images in helium at the conditions of figure 5.12 (P=200 torr, 100-pulse average, 150 ns ICCD camera gate). Primary pulse (left) and secondary pulse (right). From reference [49].

H_2-He and O_2-He

The H_2-He and O_2-He studies were conducted using the same high-voltage pulser as in the helium study using a high coupled pulse energy discharge. However, these experiments were conducted at a lower pressure (100 torr) and a lower coupled pulse energy (4-5 mJ/pulse). Data sets were collected for 1%, 2% and 5% H_2 in helium and 1%, 2%, 5% and 10% O_2 in helium. The discharge conditions in these experiments are summarized in table 5.1.

Figure 5.14 shows the discharge pulse voltage waveforms in H_2-He mixtures. Time values are referenced relative to the start of the primary current pulse, defined as $t = 0$. Peak voltage varies from 4.7 kV (0% H_2) to 3.4 kV (5% H_2), with voltage values decreasing with increasing hydrogen mole fraction. Peak voltage is reached just

Table 5.1: H_2-He and O_2-He Thomson Scattering Experimental Conditions.

Gas Mixture	Peak Voltage (kV)	Peak Current (A)	Coupled Energy (mJ/pulse)	Pressure (torr)
He	4.7	13	5	100
H_2-He	3.4-3.6	16-17	4	100
O_2-He	3.5-3.7	15.5-16.5	4	100

after the start of the primary current pulse, at $t \approx$5-10 ns, with the secondary pulse voltage peak following $\approx$300 ns later. The general structure of the voltage waveform does not change significantly with increasing H_2 fraction, with the exception of the secondary pulse moving somewhat closer to the primary pulse in time, occurring about 75 ns earlier (i.e. 225 ns after main pulse).

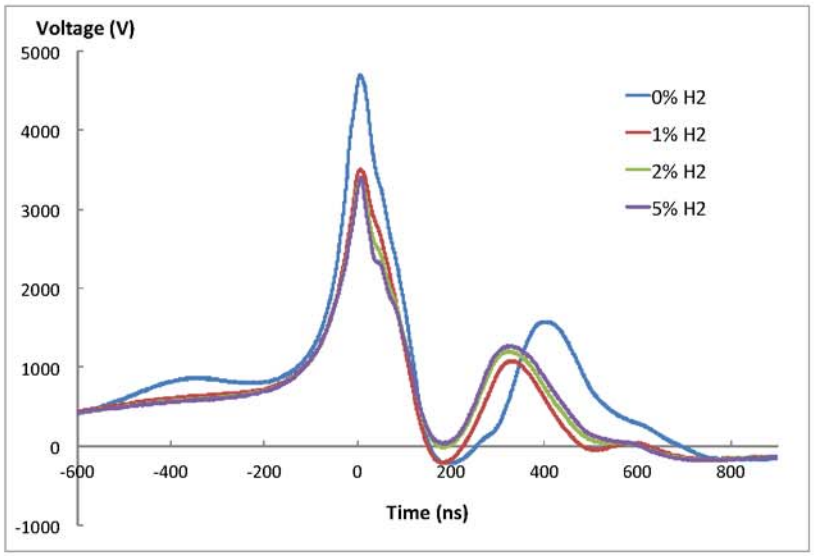

Figure 5.14: Pulse voltage waveforms in H_2-He mixtures at the conditions of table 5.1. From reference [53].

Figure 5.15 shows discharge pulse current waveforms in H_2-He at the conditions of figure 5.14. Time values are again referenced from the start of the primary current pulse, defined as $t = 0$. Peak current values vary from 13 A (0% H_2) to 17 A (1% H_2). Peak current is reached at ≈100 ns, with the secondary pulse current peak following ≈300 ns later. Once again, the secondary pulse occurs somewhat sooner when hydrogen is added to the mixture.

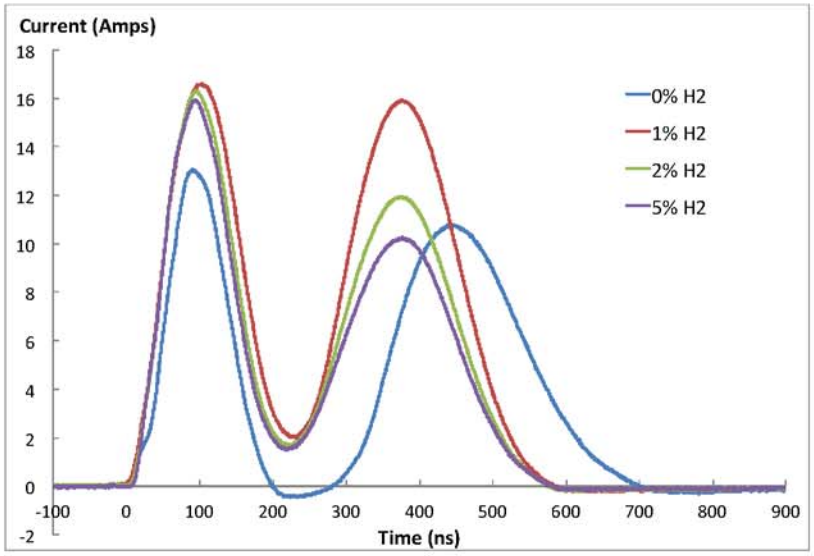

Figure 5.15: Pulse current waveforms in H_2-He mixtures at the conditions of table 5.1. From reference [53].

Figure 5.16 shows the pulse coupled energy waveforms in H_2-He mixtures at these conditions. Coupled energy in helium is ≈5 mJ/pulse, with 3 mJ coupled during the primary, and 2 mJ during the secondary pulse, while in H_2-He mixtures pulse coupled energy is ≈4 mJ/pulse, with 2 mJ coupled during the primary, and 2 mJ during the secondary pulse.

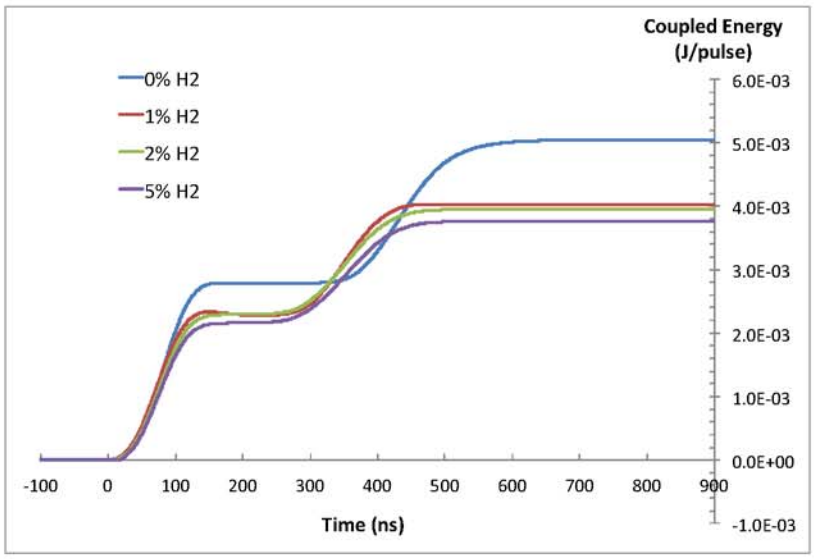

Figure 5.16: Pulse coupled energy waveforms in H_2-He mixtures at the conditions of table 5.1. From reference [53].

Figure 5.17 shows ICCD images of the broadband plasma emission in helium (at a moderate coupled pulse energy of 5 mJ/pulse), with the primary pulse image shown on the left and the secondary pulse image on the right. Both images are 100-pulse averages, and illustrate the production of a stable, diffuse, single filament discharge. Figure 5.18 shows single-shot (i.e. single pulse) ICCD images in helium at the same conditions as figure 5.17. It can be seen that the single-shot images do not differ significantly from the 100-pulse averaged images, justifying the claim of producing a stable, diffuse single filament discharge. The primary pulse filament is $\approx$3.5 mm in diameter midway between the electrodes, while the secondary pulse filament is $\approx$4 mm in diameter. Comparing these plasma filament images to those taken in helium at high coupled pulse energy (figure 5.13), it can be seen that at these conditions

the filament diameter is somewhat larger, most likely due to a lower pressure in the present study (100 torr instead of 200 torr).

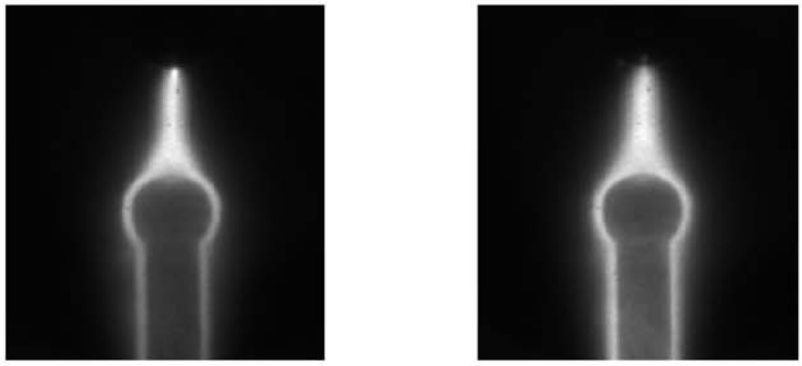

Figure 5.17: Broadband plasma emission ICCD images in helium (P=100 torr, 100-pulse average, 200 ns ICCD camera gate). Left: Primary pulse, Right: Secondary pulse. From reference [53].

Figure 5.19 shows ICCD images of the broadband plasma emission in H_2-He mixtures, including both the primary and secondary pulses. All images are 100-pulse averages, and illustrate sustaining of a stable, diffuse, single filament discharge at all sets of conditions. The filament diameter at these conditions is ≈2.5-3.5 mm, with the primary pulse generating a more diffuse filament compared to the secondary pulse.

Figure 5.20 shows the pulse voltage waveforms in O_2-He mixtures. Once again, time values are referenced from the start of the primary current pulse, defined at $t = 0$. Peak voltage at these conditions varies from 4.7 kV (0% O_2) to 3.5 kV (1% O_2). Similar to the H_2-He mixtures, peak voltage is reached just after the start of the primary current pulse, at t ≈5-10 ns, with the secondary pulse voltage peak following ≈300 ns later. Once again, the only noticeable change in the voltage waveform when

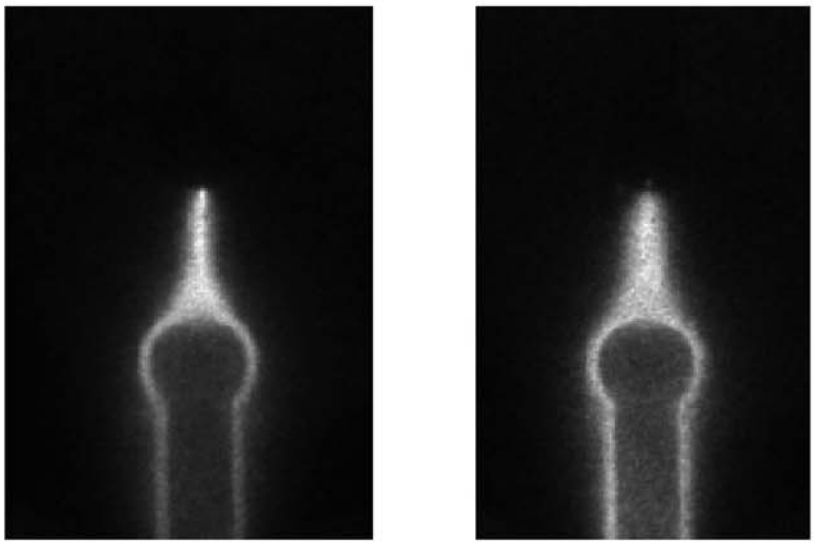

Figure 5.18: Broadband plasma emission ICCD images in helium (P=100 torr, single-shot, i.e. single pulse, 200 ns ICCD camera gate). Left: Primary pulse, Right: Secondary pulse.

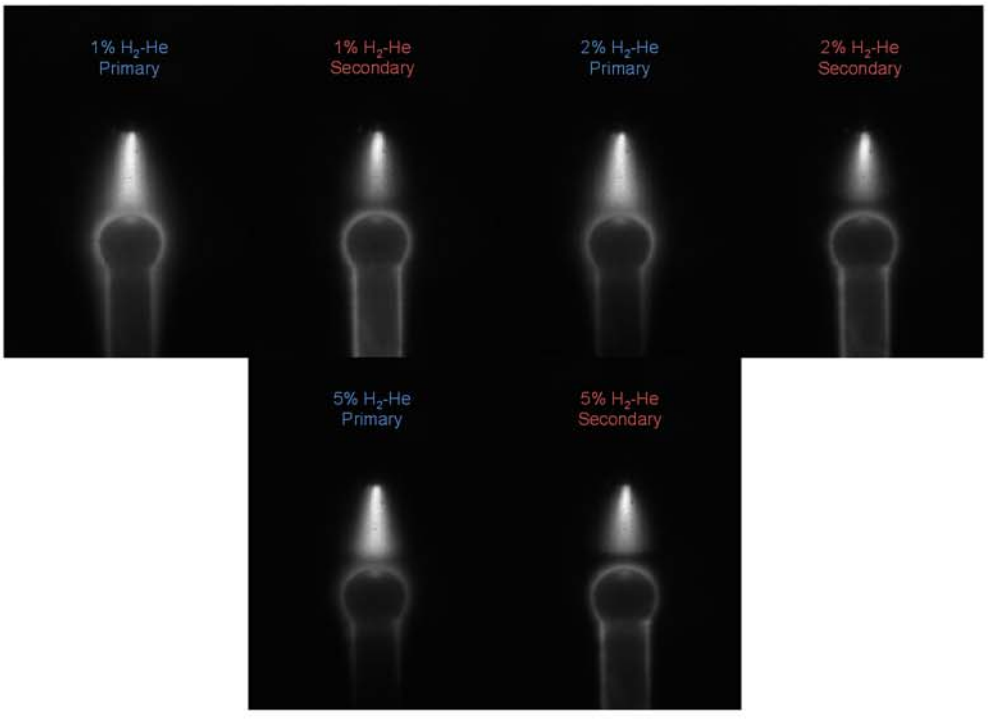

Figure 5.19: Broadband plasma emission ICCD images in H_2-He mixtures (P=100 torr, 100-pulse average, 200 ns gate). From reference [53].

oxygen is added to the mixture is that the secondary pulse occurs somewhat earlier in time (by about 75 ns).

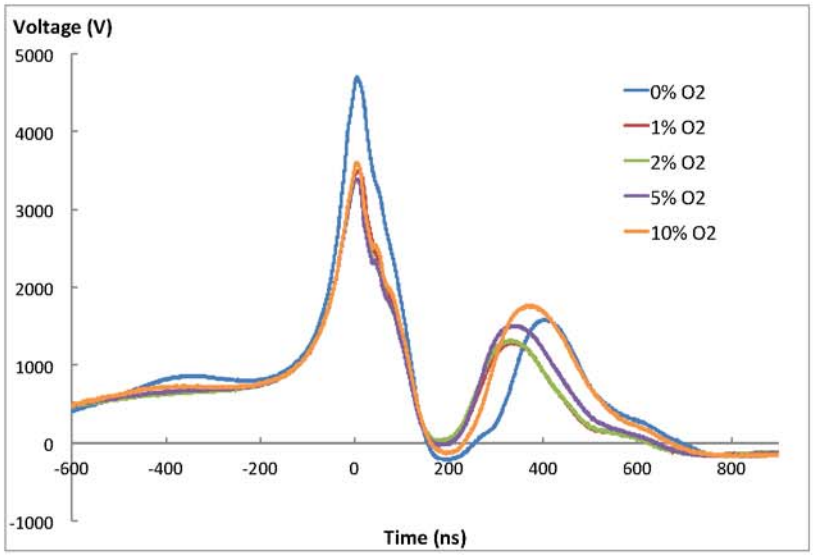

Figure 5.20: Pulse voltage waveforms in O_2-He mixtures at the conditions of table 5.1. From reference [53].

Figure 5.21 shows pulse current waveforms in O_2-He mixtures. Peak current values vary from 13 A (0% H_2) to 16.5 A (5% H_2). Peak current is reached at $t \approx 90$ ns, with the secondary pulse current peak following ≈300 ns later. Similar to the results in H_2-He mixtures, the secondary current pulse occurs earlier in time (by about 75 ns).

Figure 5.22 plots pulse coupled energy waveforms in O_2-He mixtures. Similar to H_2 and H_2-He mixtures, coupled energy in helium is ≈5 mJ/pulse, with 3 mJ coupled during the primary pulse, and 2 mJ during the secondary pulse, and ≈4 mJ/pulse in O_2-He mixtures, with 2 mJ coupled during the primary pulse, and 2 mJ during the secondary pulse.

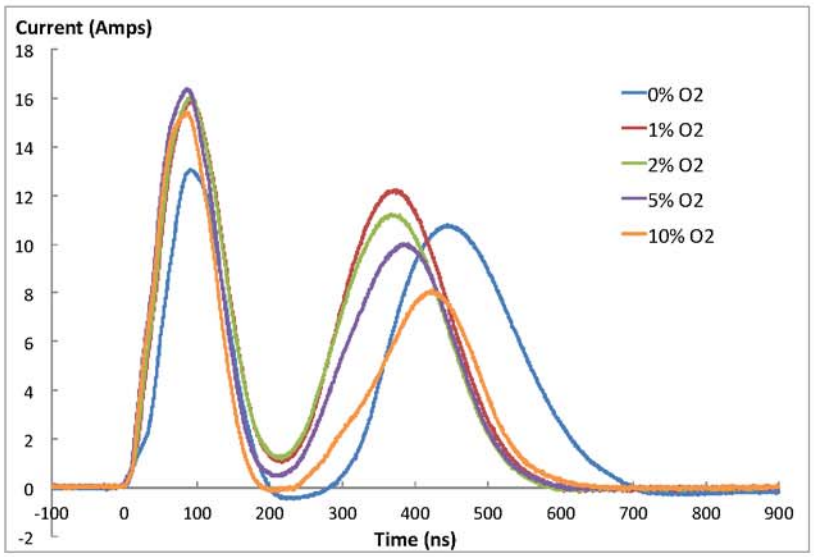

Figure 5.21: Pulse current waveforms in O_2-He mixtures at the conditions of table 5.1. From reference [53].

Figure 5.23 shows broadband plasma emission ICCD images in O_2-He mixtures, including both the primary and secondary pulses. All images are 100-pulse averages. A stable, diffuse, single filament discharge can be observed in all cases. The filament is $\approx$2.0-3.5 mm in diameter in all cases, with the filament produced by the primary pulse being somewhat larger than the one produced by the secondary pulse. Furthermore, there is noticeable constriction of the filament with increasing O_2 mole fraction.

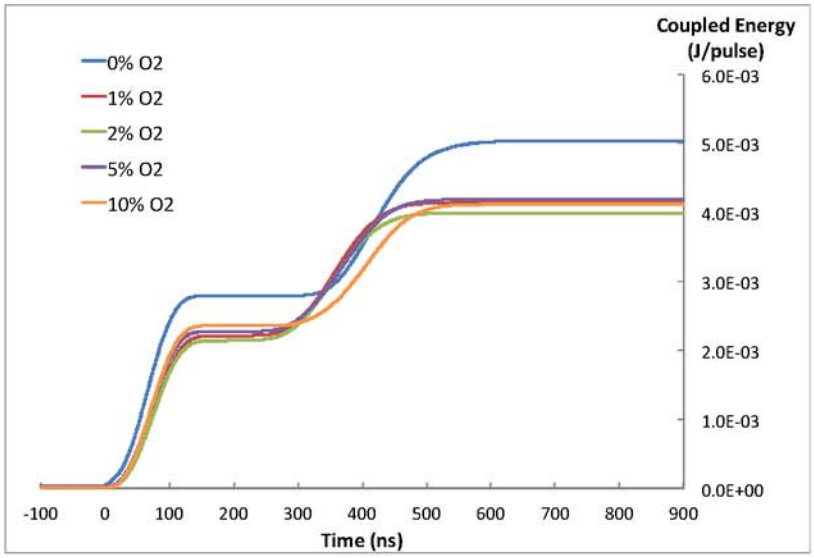

Figure 5.22: Pulse coupled energy waveforms in O_2-He mixtures at the conditions of table 5.1. From reference [53].

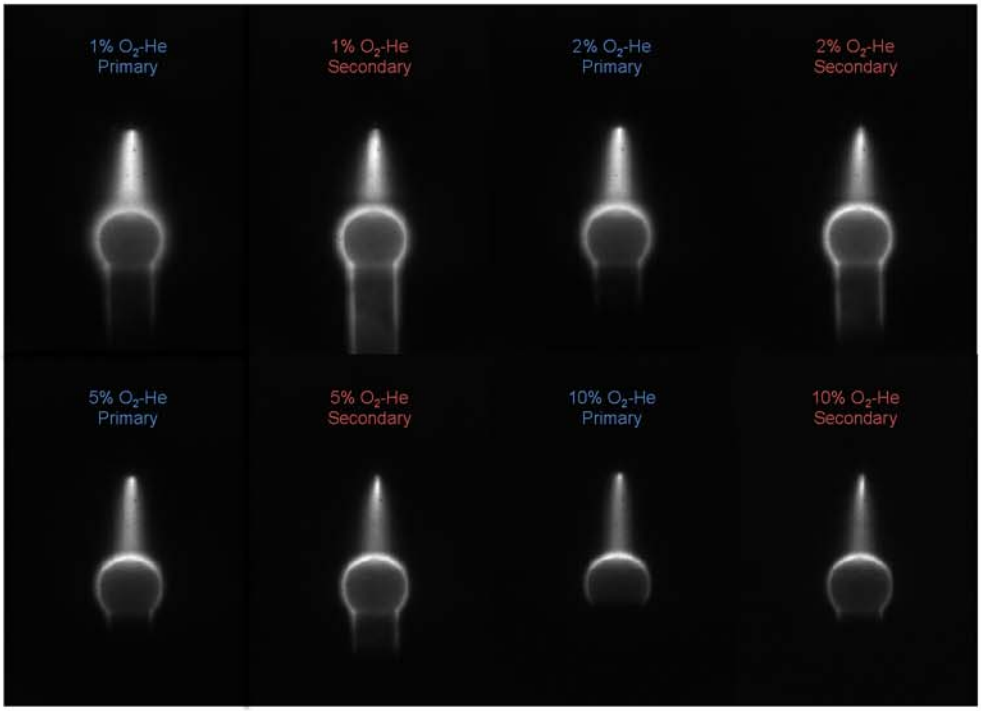

Figure 5.23: Broadband plasma emission ICCD images in O_2-He mixtures (P=100 torr, 100-pulse average, 200 ns ICCD camera gate). From reference [53].

5.6.2 Nanosecond Pulse Discharge Sustained Between Spherical Electrodes: Filtered Thomson Spectra

This section discusses the acquisition of the filtered Thomson spectra, with sample fitted spectra in helium (at high coupled pulse energy), and in H_2-He and O_2-He mixtures (at moderate coupled pulse energy) in a nanosecond pulse discharge sustained between two spherical electrodes. In all studies, Thomson scattering signal is collected from a 2.75 mm long, ≈60 μm diameter region, which approximately spans the overlap of the laser beam with the discharge filament. This signal collection cylinder is centered midway between the electrodes. ICCD camera pixels corresponding to the measurement region were binned together before reading out the spectrum, and thus the data are inherently spatially averaged over this region.

Helium

In helium, at high coupled pulse energy, the data were taken at a pressure of 200 torr. Spectra were collected with 2200 individual laser shots per 'exposure' (1.25 minute collection time), with four exposures averaged. The ICCD camera gate used was 50 ns. A sample collected Thomson scattering spectrum, along with the spectral fit is shown in figure 5.24. At these conditions, signal-to-noise (S/N), defined as (S/S_{avg}), where S_{avg} is the mean deviation in the baseline, is approximately 80. The entire spectral fitting procedure is described in section 5.2. Data points were collected for time delays ranging from 20 ns to 3 μs after the start of the primary current pulse.

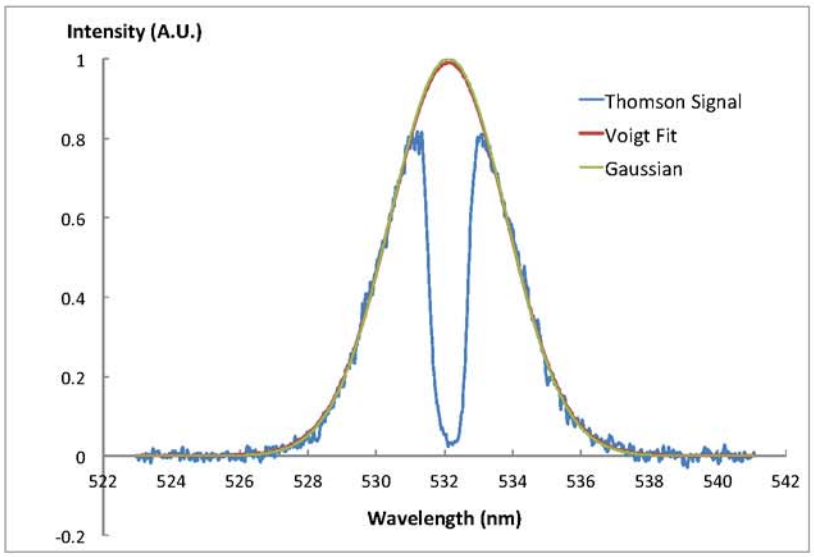

Figure 5.24: A typical Thomson scaterring spectrum in helium (P=200 torr, 80 ns after start of discharge current pulse), shown with least-squares Voigt fit and inferred Gaussian profile. From reference [49].

H_2-He

In H_2-He mixtures, the experiments were conducted for 1%, 2% and 5% H_2 in helium, all at a total pressure of P=100 torr. The data collection conditions are summarized in table 5.2. 9000 individual laser shots per 'exposure' were used, with 4-exposure averages, to collect the Thomson scattering spectra. Data points (i.e. Thomson scattering spectra) were collected starting 15 ns after the start of the primary current pulse for all gas mixtures. Thomson scattering spectra were collected out to 3 μs, 850 ns, 750 ns and 600 ns for 0%, 1%, 2% and 5% H_2 cases, respectively. Time ranges were shortened with increasing H_2 fraction due to lower Thomson scattering signal levels (i.e. lower electron densities).

Table 5.2: H_2-He Thomson Scattering Data Collection Conditions.

Mixture	Laser Shots per Exposure	Accumulation Time (min.)	Averaged Exposures	Camera Gate (ns)	Time Delay Range
Pure He	9000	5	4	20	15 ns-3 μs
1% H_2	9000	5	4	20	15 ns-850 ns
2% H_2	9000	5	4	20	15 ns-750 ns
5% H_2	9000	5	4	20	15 ns-600 ns

Figure 5.25 shows a sample Thomson scattering spectrum in a 5% H_2-He mixture, 100 ns after the start of the primary discharge current pulse, along with a spectral fit. S/N for this spectrum is approximately 20. The spectral fitting procedure is discussed in section 5.2.

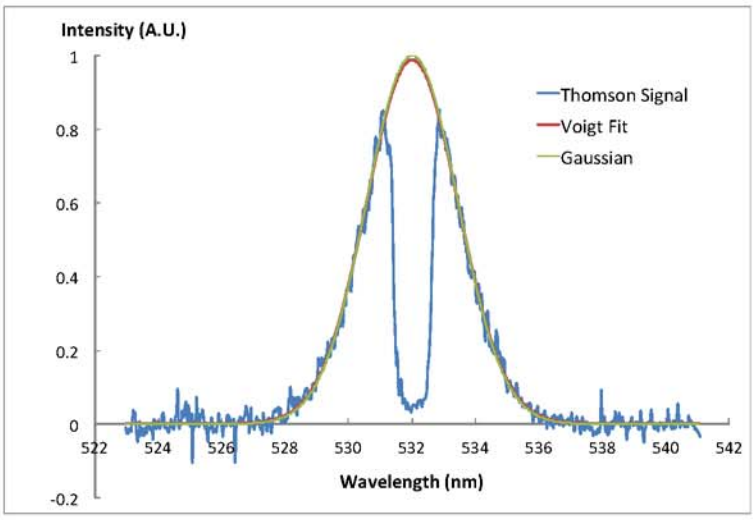

Figure 5.25: A typical Thomson scaterring spectrum in a H_2-He mixture (5% H_2-He, P=100 torr, 100 ns after start of discharge current pulse), shown with least-squares Voigt fit and inferred Gaussian profile. From reference [53].

Table 5.3: O_2-He Thomson Scattering Data Collection Conditions.

Mixture	Laser Shots per Exposure	Accumulation Time (min.)	Averaged Exposures	Camera Gate (ns)	Delay Range
Pure He	9000	5	4	20	15 ns-3 μs
1% O_2	12600	7	4	20	10 ns-1.5 μs
2% O_2	12600	7	4	20	10 ns-1.5 μs
5% O_2	12600	7	4	20	10 ns-650 ns
10% O_2	12600	7	4	20	10 ns-650 ns

O_2-He

In O_2-He mixtures, the experiments were conducted for 1%, 2%, 5% and 10% O_2 in helium, all at a total pressure of P=100 torr. The collection conditions are summarized in table 5.3. In helium, 9000 individual laser shots were collected per exposure, while in O_2-He mixtures, 12,600 laser shots were used. Additionaly, four exposures were collected and averaged for all data points (i.e. delay time after the start of the discharge current pulse). Data points were collected starting at $t = 15$ ns after the start of the primary current pulse in helium, and at $t = 20$ ns for all other gas mixtures. Thomson scattering spectra were collected for time delays out to 3 μs, 1.5 μs, 1.5 μs, 650 ns and 650 ns for 0%, 1%, 2%, 5% and 10% O_2-He mixture cases, respectively. Time ranges were shortened with increasing O_2 fraction due to lower Thomson scattering signal levels (i.e. lower electron densities).

In addition to the standard collection procedure described in section 5.2, oxygen-containing gas mixtures require one additional step. In general, linear diatomic molecules add additional interference to the Thomson scattering spectrum in the form of pure rotational Raman scattering. Since Raman scattering is inelastic, the

rotational lines will have a wavelength shift, and will not be spectrally centered at the same wavelength as the incident radiation. As a result, the spectral masking procedure, which filters out Rayleigh scattering and the central portion of the Thomson scattering, will have no effect in filtering this interference.

This interference is not a factor in the case of helium or H_2 containing mixtures. Helium is not a concern since it is a monatomic gas and therefore does not have a rotational Raman spectrum. In H_2 mixtures, the Raman shift is sufficiently large that rotational lines are shifted outside of the Thomson scattering spectral region (i.e. B, the rotational constant, is relatively large, $B_{H_2} = 60.853$ cm^{-1} from NIST Chemistry WebBook, corresponds to ≈1.72 nm for 532 nm incident light), and thus do not interfere with Thomson spectra collection. However, this is not the case for O_2 molecules, which have a much smaller rotational constant ($B_{O_2} = 1.438$ cm^{-1} from NIST Chemistry WebBook, corresponds to ≈0.04 nm for 532 nm incident light), and therefore much smaller rotational energy spacing. For comparison, typical spectral width for Thomson scattering spectra at the present conditions is ≈106 cm^{-1}. Figure 5.26 shows a typical Thomson/Raman scattering spectrum collected through the triple-grating spectrometer in a 10% O_2-He mixture, 100 ns after the start of the discharge current pulse. Fairly well resolved rotational structure of the O_2 Raman scattering spectrum, overlapped with the Thomson scattering spectrum, can be observed.

In order to remove the O_2 rotational Raman spectra from the Thomson spectra, a background subtraction method was employed. Since rotational/translational temperature is not expected to change significantly in nanosecond pulse discharge afterglow plasmas over the timescale of ≈10 μs [13], the structure of the pure rotational spectrum would not change significantly over this time delay. On the other

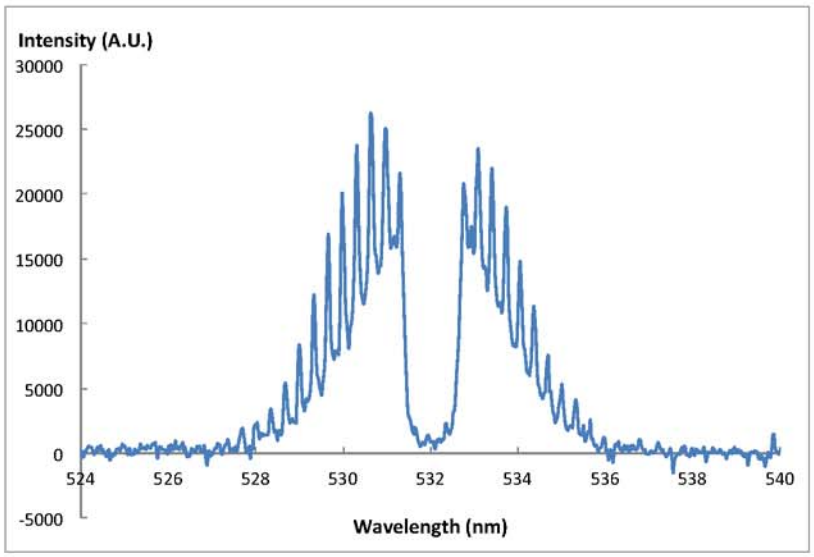

Figure 5.26: A typical Thomson scaterring spectrum in an O_2-He mixture (10% O_2-He, P=100 torr, 100 ns after start of discharge current pulse), with O_2 rotational Raman structure overlapping with Thomson scattering signal. From reference [53].

hand, electron density in the afterglow is expected to change significantly on this time scale, due to both electron-ion recombination and electron attachment to O_2 molecules. This is evident by considering simple estimates of characteristic electron recombination time and electron attachment time.

Characteristic electron recombination time ("$1/e$" decay time) can be estimated as follows. Electron density decay rate is given as,

$$\frac{dn_e}{dt} = \beta_{rec} n_e n_i = \beta_{rec} n_e^2 \tag{5.15}$$

where β_{rec} is the recombination rate coefficient, given as,

$$\beta_{rec} \approx c\,[T_e(eV)]^{-1/2} \tag{5.16}$$

where c is $\approx 10^{-8}$ cm^3/s for electron recombination with He_2^+, and $\approx 10^{-7}$ cm^3/s for electron recombination with H_2^+ and O_2^+. Canceling n_e from both sides of eqn. 5.15

and rearranging yields the following expression for characteristic recombination time of electrons,

$$\tau_{rec} \approx \frac{1}{\beta n_{e_{t=0}}} \tag{5.17}$$

This is the "$1/e$" decay time. For $n_{e_{t=0}} = 3 \cdot 10^{14}$ cm^{-3} and $T_e \approx 2$ eV (typical conditions in the present experiments) in helium, $\tau_{rec} \approx 1$ μs. At the same conditions in H_2 or O_2, $\tau_{rec} \approx 100$ ns. This indicates significant decay (by an order of magnitude) of n_e will likely occur within $\approx$1 μs or less in the present experiments, resulting in the Thomson scattering spectrum disappearing into the noise of the diagnostic at these timescales.

The characteristic time for electron attachment can be estimated by,

$$\tau_{O_2-attachment} \approx \frac{1}{\nu_{O_2-attachment}} \tag{5.18}$$

where $\nu_{O_2-attachment}$ is the collision frequency for the electron attachment process, given as,

$$\nu_{O_2-attachment} = k_{O_2-attachment} N_{O_2}^2 \tag{5.19}$$

where $k_{O_2-attachment} \approx 2.5 \cdot 10^{-30}$ cm^6/s (taken from the literature [25]) is the O_2 attachment rate coefficient, and N_{O_2} is O_2 number density ($\approx 3.22 \cdot 10^{17}$ cm^{-3} at partial pressure of oxygen P_{O_2}=10 torr and T=300 K; approximately present experimental conditions). Substituting, the characteristic timescale for electron attachment at these conditions is $\approx$3-4 μs.

Consistent with the above analysis, time-resolved electron density measurements in the present work show significant decay of electron density (by an order of magnitude) within $\approx$200 ns to 500 ns after the secondary pulse in O_2-He mixtures (see section 5.8 for O_2-He mixtures).

Based on the above analysis, a background, pure rotational O_2 Raman spectrum was taken 5 μs after the start of the discharge current pulse, allowing sufficient time for significant electron recombination and attachment to take place (such that Thomson scattering signal would completely decay), but not enough time for the rotational Raman spectrum to be affected by temperature change in the afterglow. This spectrum is shown in figure 5.27.

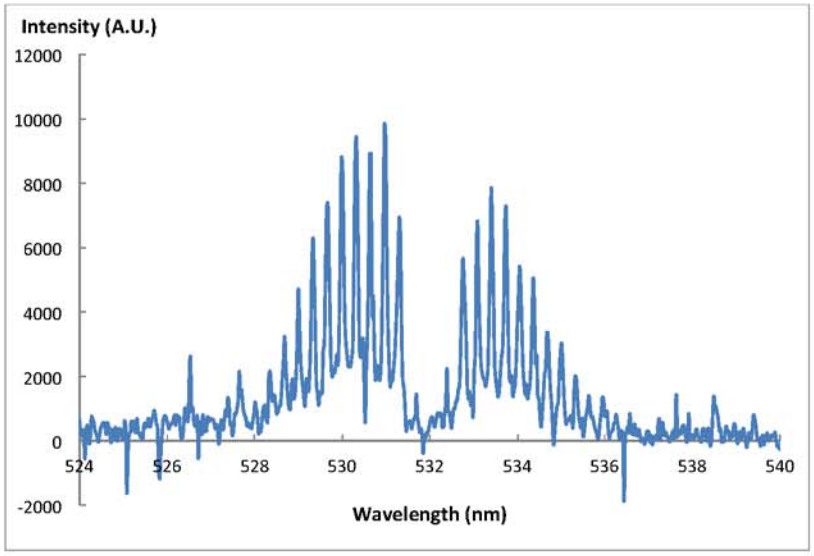

Figure 5.27: O_2 'pure' rotational Raman spectrum at the discharge conditions of figure 5.14 (10% O_2-He, P=100 torr, 5 μs after start of discharge current pulse). From reference [53].

The background spectrum (plotted in figure 5.27) is then subtracted from the raw spectrum (plotted in figure 5.26), to isolate the final Thomson scattering spectrum. This spectrum, plotted together with the least-squares Voigt fit and inferred Gaussian profile is shown in figure 5.28. As can be observed, the Raman spectrum subtraction

procedure works quite well, removing the rotational Raman structure almost completely without significantly affecting the Thomson scattering spectrum. S/N for this spectrum is approximately 20. Once again, the detailed spectral fitting procedure is presented in section 5.2.

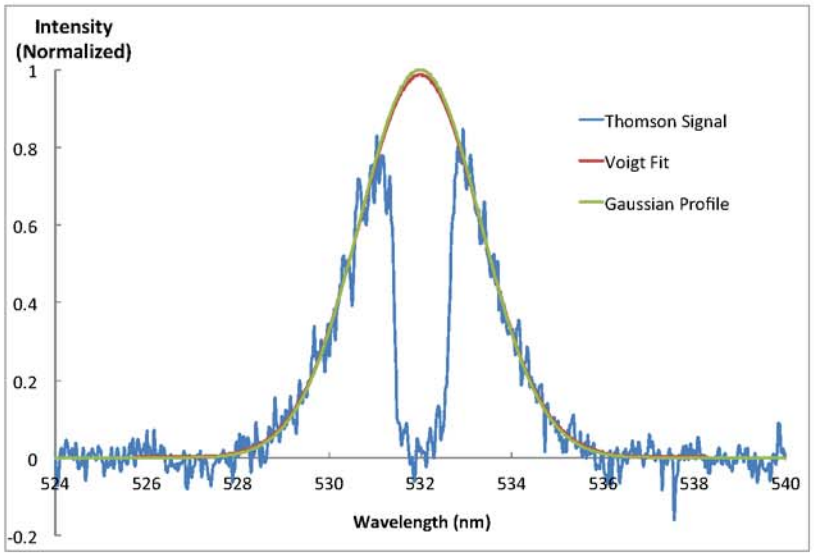

Figure 5.28: Thomson scaterring spectrum, at the discharge conditions of figure 5.14, after O_2 rotational Raman spectrum subtraction (10% O_2-He, P=100 torr, 100 ns after start of discharge current pulse), shown with least-squares Voigt fit and inferred Gaussian profile. From reference [53].

5.7 2-D Kinetic Model

A two-dimensional kinetic model was used to predict the electron density and electron temperature in a nanosecond pulse discharge in helium. A brief summary of the model is given here. For a more detailed description of the model, see reference [49].

The 2-D kinetic model used includes time-dependent conservation equations for the number densities of electrons, ionic (He^+, He_2^+, H^+, H_2^+, and H_3^+), and neutral

species (including rotationally, vibrationally, and electronically excited H_2 molecules as well as ground state and electronically excited He species). These equations are coupled with a two-term expansion Boltzmann equation solver for determination of the electron energy distribution function (EEDF) and electron swarm parameters (as well as electron impact rate coefficients), an equation for the electron temperature, the Poisson equation for determination of the electric field, and the Navier-Stokes equations for heavy species, including the energy equation predicting gas temperature. Superelastic electron-neutral collisions, which are an important source of electron heating during the afterglow, are incorporated as well.

The simulations for this work were done only in helium, for the high coupled pulse energy conditions. The experimental voltage waveform (figure 5.12) was used as an input parameter to the model. The model assumes a two-dimensional, axisymmetric Cartesian geometry, simulating the discharge filament between two plane electrodes. The computational domain is shown in figure 5.29, and incorporates a 9 mm diameter cylinder, with two plane, copper electrodes at the ends, separated by a 1 cm gap. In the experiment, spherical, rather than plane, electrodes were utilized. However, due to a relatively small diameter discharge filament ($\approx$3 mm, as determined from ICCD imaging) compared to the electrode diameter (7.5 mm), the electrode curvature effect was neglected in the model. The high-voltage pulse was applied to the top electrode, based on the measured voltage and current waveforms (see figure 5.12), while the bottom electrode was grounded. The discharge filament is located centrally within the computational domain, along the axis of symmetry of the spherical electrodes. The simulations were carried out in helium gas at a pressure of P=200 torr, with initial

temperature T=300 K; i.e. at the same conditions as in the experiment illustrated in figure 5.12.

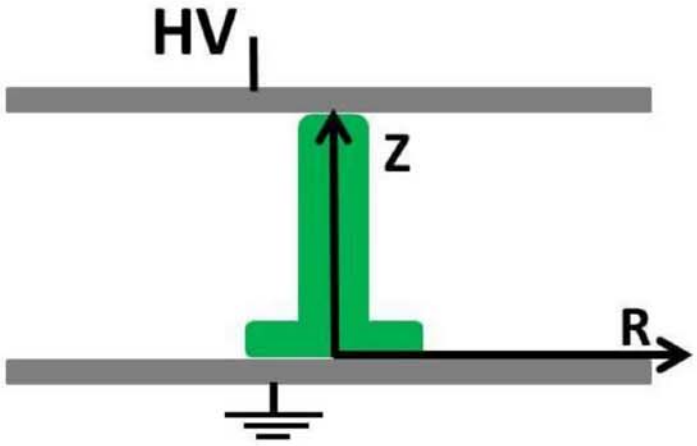

Figure 5.29: Schematic of the 2-D kinetic model computational domain. From reference [49].

5.8 Nanosecond Pulse Discharge Sustained Between Spherical Electrodes: Electron Temperature, Electron Density and EEDF Results

This section presents the results obtained in nanosecond pulse discharges in helium at high coupled pulse energy (17 mJ/pulse), as well as H_2-He mixtures, and O_2-He mixtures at moderate coupled pulse energy (4-5 mJ/pulse) in a single filament discharge sustained between two spherical electrodes. Results for time-resolved electron temperature, electron number density and electron energy distribution function (EEDF) are compared with 2-D kinetic modeling predictions in helium at high coupled pulse energy.

5.8.1 Helium

Portions of this discussion are taken from reference [49]. All results presented here were taken at P=200 torr in helium at high coupled pulse energy (17 mJ/pulse). Voltage, current and coupled energy waveforms at these conditions are plotted in figure 5.12. Figure 5.30 plots the experimental, time-resolved electron number density in the discharge and in the afterglow. The results show an initial, fairly rapid increase in electron number density over the first 100 ns (i.e. during the discharge pulse; see figure 5.12). The peak measured electron density is $n_e \approx 3.4 \cdot 10^{15}$ cm^{-3}. After this, the electron density decays during the afterglow over 3 μs. One noticeable feature is an increase in electron number density at $t \approx$600 ns. This is a result of the secondary discharge pulse (see figure 5.12), which results in additional energy coupling and a transient rise in electron density.

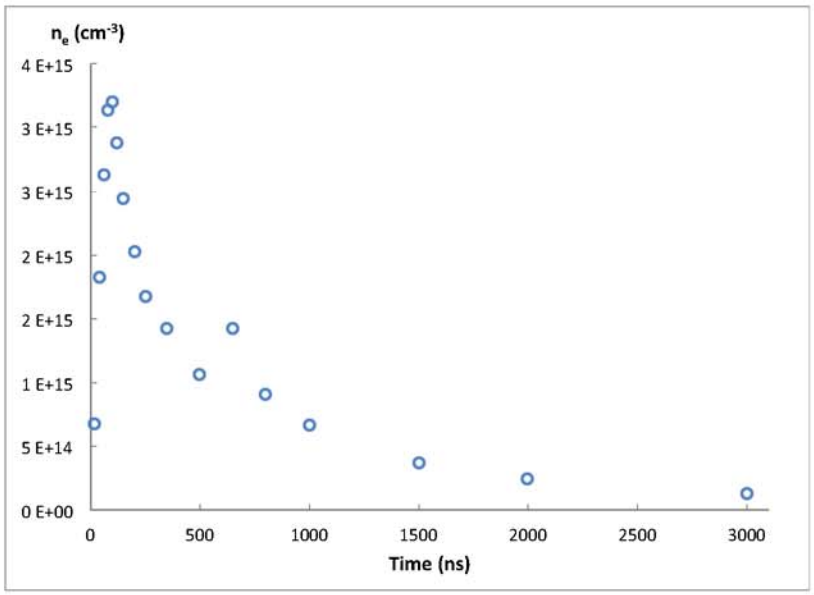

Figure 5.30: Time-resolved electron number density in a nanosecond pulse discharge and afterglow in helium (P=200 torr, 17 mJ/pulse).

Figure 5.31 compares the experimental electron density with kinetic modeling predictions. Symbols represent the experimental data, while the solid line represents the 2-D kinetic model prediction. Error bars are representative of the temporal uncertainty of the data due to the high voltage pulse generator jitter and the inherent linewidth of the laser pulse (±15 ns for all data points shown). It can be seen that the modeling calculations reproduce the trends of rapid electron density increase, followed by near-exponential decay, quite well. However, the model overpredicts the rate of the initial rise, as well as the peak electron number density (by approximately a factor of 2). Temporal uncertainty of the data is likely a significant factor in the discrepancy of the initial electron density rise rate (during the first 100 ns) between the experiment and the model. Note that the secondary discharge pulse is not incorporated in the model.

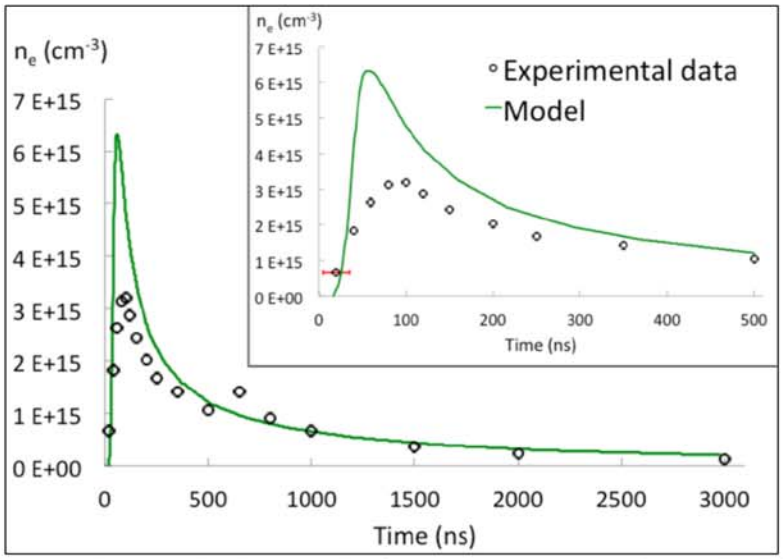

Figure 5.31: Comparison of time-resolved electron number density measured at the conditions of figure 5.12 with modeling calculations (helium, P=200 torr, 17 mJ/pulse). From reference [49].

Figure 5.32 presents the experimental data for the time-resolved electron temperature at the conditions of figure 5.12. Similar to the electron density, there is an apparent initial rapid electron temperature rise during the discharge pulse followed by decay in the afterglow. However, the initial rise in electron temperature occurs too rapidly to be resolved by the present diagnostic. Peak electron temperature measured was approximately 4 eV. However, the electron temperature at the early stages of the discharge pulse (t<20 ns), when electron density is still too low to be detected, may well be higher. It is also notable that the electron temperature decay occurs more rapidly compared to that of the electron number density. This is expected, since the timescale for energy loss in elastic and inelastic collisions is much shorter compared to the timescale for two-body and three-body recombination, which are the dominant mechanisms of electron number density decay at the present conditions.

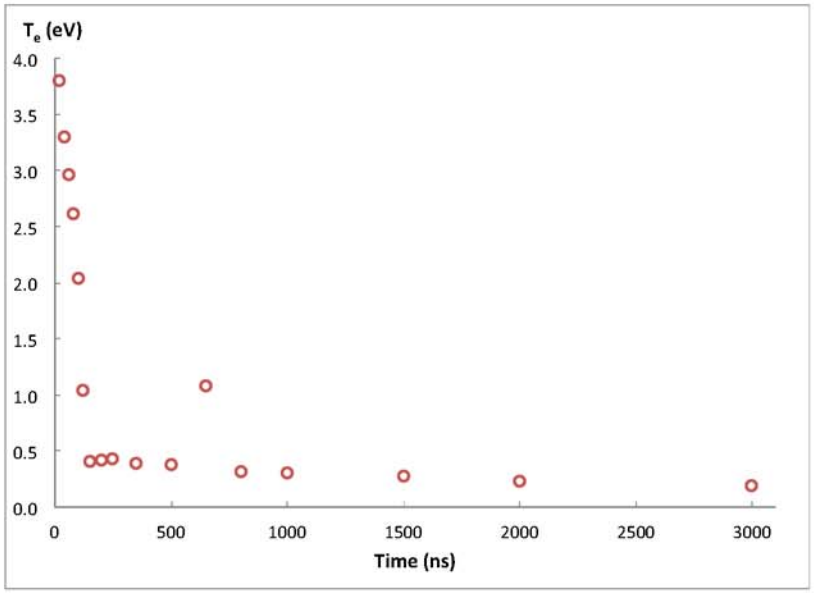

Figure 5.32: Time-resolved electron temperature measured at the conditions of figure 5.12 (helium, P=200 torr, 17 mJ/pulse).

The characteristic time for electron recombination in helium was estimated earlier in section 5.6 (see equations 5.15-5.17 and surrounding discussion) to be $\tau_{rec} \approx 1$ μs. The characteristic time for electron cooling can be estimated by considering the electron energy balance [25],

$$\frac{d\epsilon}{dt} = \left[\frac{e^2E^2}{m_e(\omega^2 + \nu_m^2)} - \frac{2m_e}{M}\epsilon\right]\nu_m \tag{5.20}$$

where, the right-most term represents electron energy loss due to collisions, where M is neutral/ion mass, ϵ is electron energy, and ν_m is the electron collision frequency. Considering only the collision (right-most) term in equation 5.20 and canceling ϵ on both sides, the characteristic time for electron cooling is given as,

$$\tau_{e-cooling} \approx \frac{M}{2m_e\nu_m} \tag{5.21}$$

Equation 5.21 represents an upper bound estimate for $\tau_{e-cooling}$, since it takes into account only elastic collisions, in which the electron energy loss is very inefficient. Noting that collision frequency is,

$$\nu_m = v_e N \sigma_m \tag{5.22}$$

where $v_e \approx 10^8$ cm/s is electron velocity, N is neutral species number density and σ_m is the cross section for electron-neutral collisions. $N \approx 10^{18}$ cm^{-3} at P=100 torr. $\sigma_m \approx 6.8 \cdot 10^{-16}$ cm^2 for electron temperature of 1 eV in helium (typical conditions for the present work) as taken from the literature [54]. This yields a collision frequency of $\nu_m \approx 6.8 \cdot 10^{10}$ 1/s. Substituting this into eqn. 5.21, and taking the electron and He masses into account, the characteristic time for electron cooling in helium becomes $\tau_{e-cooling} \approx 100$ ns. This estimate is consistent with the data, since the electron temperature decays from ≈4.0 eV to ≈0.4 eV (an order of magnitude decrease) within approximately 150 ns (see inset of figure 5.33).

Figure 5.33 shows a comparison of the experimental electron temperature with the modeling predictions. It can be seen that the model reproduces the trends of electron temperature rise and decay quite well, although it overpredicts peak electron temperature value at the early stage of the pulse (up to $T_e \approx 10$ eV at $t \approx 20$ ns after breakdown).

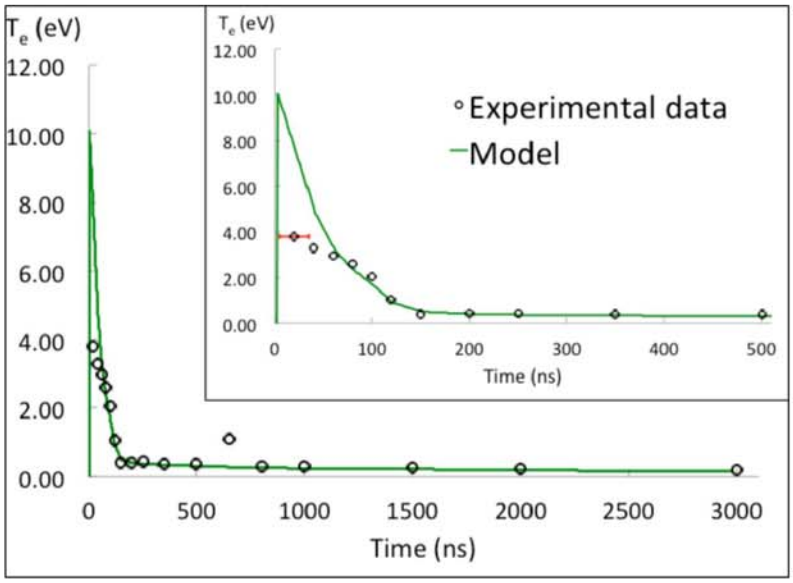

Figure 5.33: Comparison of time-resolved average electron temperature with modeling calculations (helium, P=200 torr, 17 mJ/pulse). From reference [49].

One more item to note is that the electron temperature in the afterglow does not decrease all the way to the gas temperature, but stabilizes around $T_e = 0.3$ eV ($\approx$3000 K). This is mainly due to superelastic collsions between electrons and metastable excited helium atoms and excimers,

$$He^* + e^- \rightarrow He + e^- \tag{5.23}$$

Figure 5.34 shows a comparison between the experimental data and two modeling predictions, one with superelastic collisions included in the calculations (left), and the other without superelastic collisions (right). This illustrates that ignoring superelastic collisions results in a significant under-prediction of the electron temperature in the afterglow, which decays down to room temperature. Thus, electron heating by superelastic collisions is an important process in the afterglow of a nanosecond pulse discharge in helium.

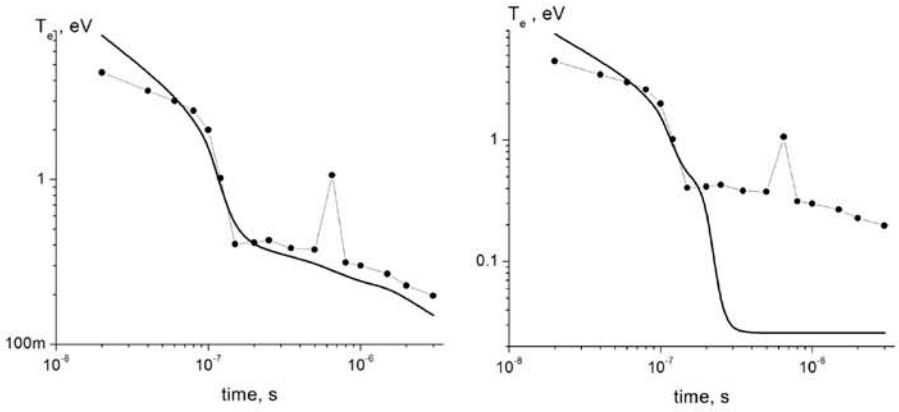

Figure 5.34: Comparison of time-resolved electron temperature with modeling predictions showing the effect of superelastic collisions. Left: superelastic collisions included in modeling calculations. Right: superelastic collisions neglected in modeling calculations.

Figures 5.35 and 5.36 show contour plots of electron number density and electron temperature predicted by the kinetic model, at two different points in time during the discharge pulse. At the early stage of the breakdown process, shortly after the high voltage pulse is applied, but before the electric field in the gap is sufficiently high for ionization, initial "seed" electrons move toward the anode, leaving an electron-free

region near the cathode, generating a high electron concentration region behind the wave front. Thus, when the electric field in the gap reaches breakdown threshold, ionization initially occurs near the anode, and an ionization wave propagates towards the cathode, generating a high electron concentration region behind the wavefront. During this stage, the voltage drop across the region with high electron concentration (behind the wave) is relatively low compared to the rest of the discharge gap (ahead of the wave). As the ionization wave moves closer to the cathode, the voltage drop across the cathode layer increases.

Figure 5.35 plots the predicted electron number density distribution at the moment when the ionization wave reaches the cathode (left), and immediately after the wave has reached the cathode (right). It is at this latter point when secondary emission from the cathode becomes significant. It can be seen that the discharge filament has a cylindrical shape before it reaches the cathode, but its head spreads considerably after reaching the cathode. Spreading of the filament head produces much higher secondary electron emission from the cathode, which is necessary to maintain the current in the rest of the discharge. The predicted filament diameter near the cathode is approximately a factor of two larger than the rest of the discharge filament. Expansion of the discharge filament over the cathode surface predicted by the model is qualitatively consistent with ICCD images of plasma emission shown in figure 5.13. Note that the model significantly underpredicts the size of the 'cathode spot' observed in the experiments.

Electron temperature distributions, at the same moments in time, are shown in figure 5.36. It can be observed that electron temperature in the cathode layer, where

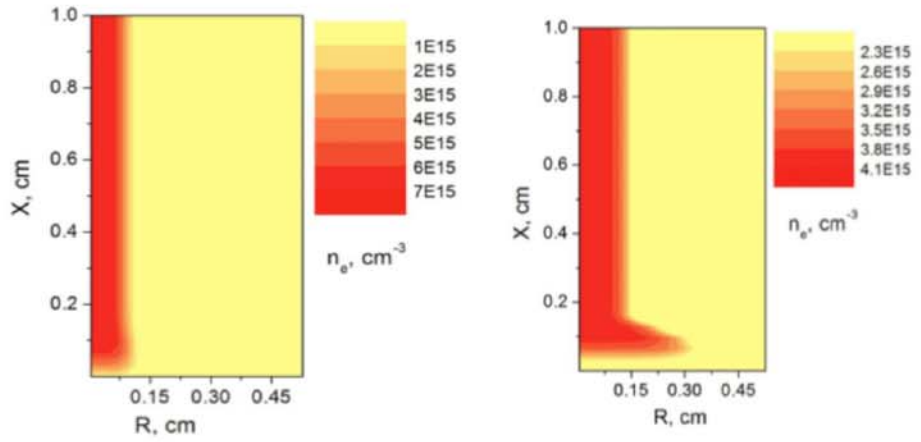

Figure 5.35: Predicted electron density distribution at two moments in time (helium, P=200 torr, ≈17 mJ/pulse). Left: moment when ionization wave reaches cathode (t≈0 ns). Right: Immediately after ionization wave reaches cathode (t≈1 ns). From reference [49].

the electric field peaks, is very high (up to T_e ≈25 eV), although the electron density in the cathode layer is very low.

Figures 5.37-5.39 show time-resolved electron energy distribution functions (EEDFs) in helium at high coupled energy (17 mJ/pulse). All EEDFs plotted are Maxwellian EEDFs, inferred from the electron number density and electron temperature values for each temporal data point (see section 5.5 for data reduction details). Figure 5.37 plots the EEDFs during the discharge pulse at 10 ns to 120 ns. It can be observed that initially (t<100 ns), the electron energy distribution function has a well-pronounced, high-energy tail, extending up to ≈20 eV. During this period of time, a major fraction of the pulse energy (≈70%) is coupled to the plasma. Shortly after this (t=120 ns), the electrons begin to lose energy by collisions, with the tail rapidly vanishing.

This trend continues in the afterglow between the pulses (150 ns-3 μs), as shown in figure 5.38. It can be seen that in the afterglow, as time elapses, the electron

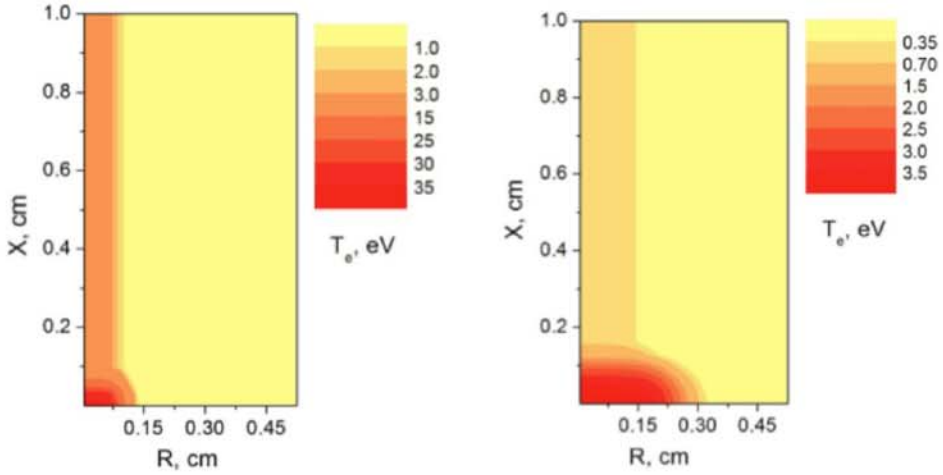

Figure 5.36: Predicted electron temperature distribution at two moments in time (helium, P=200 torr, ≈17 mJ/pulse). Left: moment when ionization wave reaches cathode (t≈0 ns). Right: Immediately after ionization wave reaches cathode (t≈1 ns). From reference [49].

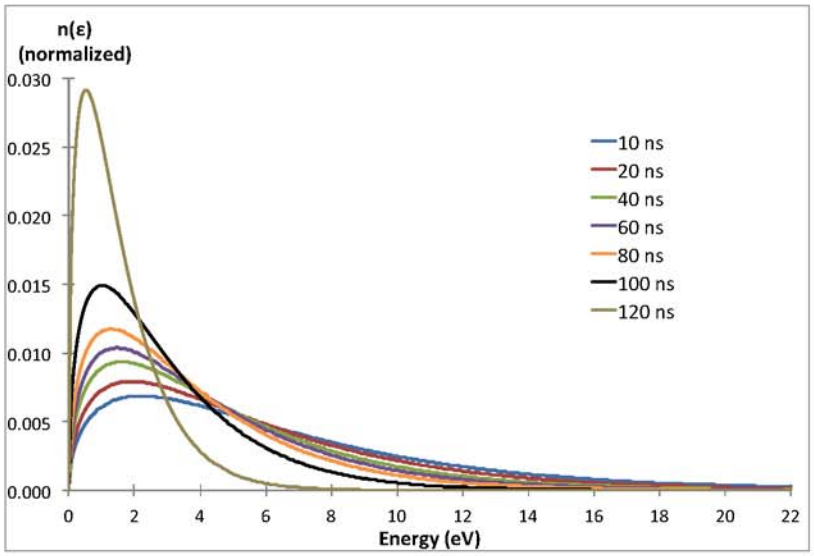

Figure 5.37: Time-resolved Maxwellian EEDFs from 0-120 ns at the conditions of figure 5.12 (helium, P=200 torr, 17 mJ/pulse).

temperature decays, such that a larger fraction of the electrons have lower energies. The one exception is the data point at 650 ns. Here it can be observed that the electrons are heated by the applied field again. This is a result of the additional energy coupled to the plasma during the secondary pulse (see figure 5.12). Following this, electron temperature and EEDF resume their monotonous decay in the afterglow.

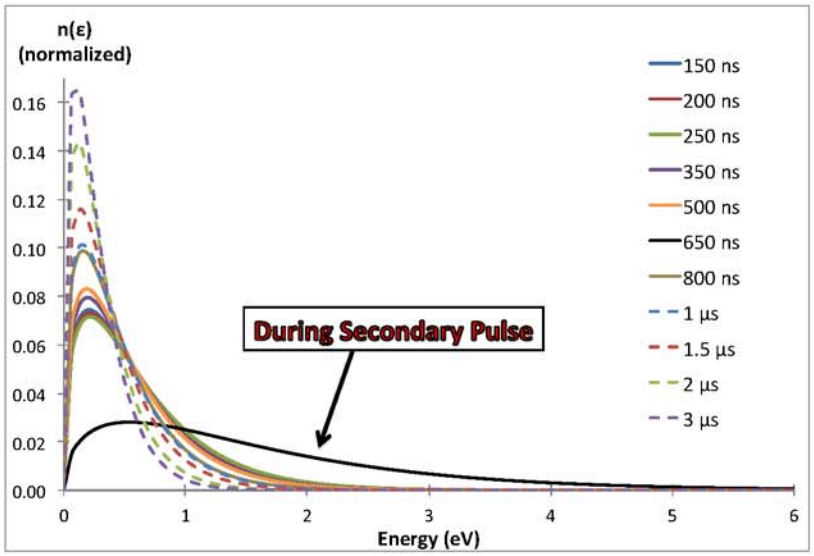

Figure 5.38: Time-resolved Maxwellian EEDFs from 150 ns-3 μs at the conditions of figure 5.12 (helium, P=200 torr, 17 mJ/pulse).

Figure 5.39 shows the part of the EEDFs in figure 5.37. $(n(\epsilon)/\sqrt{\epsilon})$ plotted on a semi-logarithmic scale, which yields a series of straight lines, with the slopes inversely proportional to the electron temperature. Thus, a steeper slope corresponds to a lower electron temperature. The same trends as seen in figure 5.37 can be observed here. Recall that based on the Gaussian fit to the Thomson spectrum (which assumes a Maxwellian EEDF), a Maxwellian EEDF can only be confirmed by the present experiments down to a relative population of 10^{-3} (see section 5.5). For relative

populations below this value (i.e. in the high energy tail of the EEDF), the present results are inconclusive, though in the plot the full EEDFs are shown as Maxwellian.

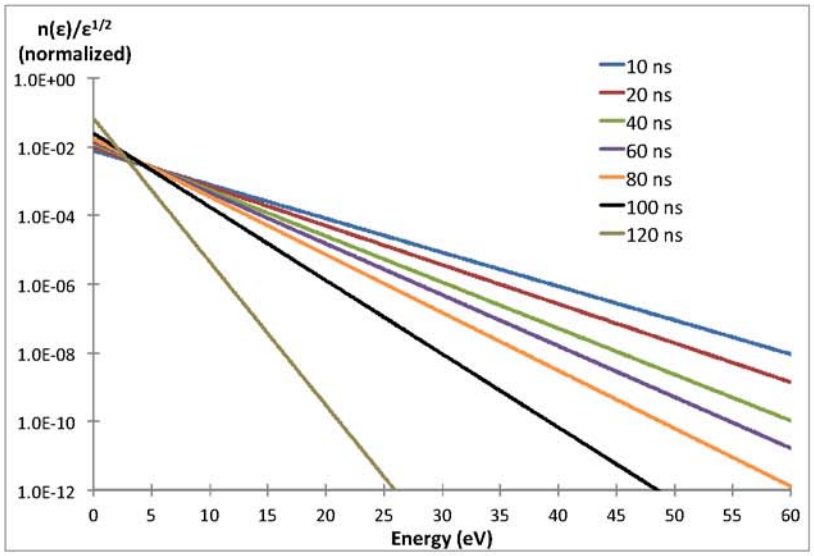

Figure 5.39: Time-resolved exponential part of EEDF ($n(\epsilon)/\sqrt{\epsilon}$) plotted on a semi-logarithmic scale from 0-120 ns at conditions of figure 5.12 (helium, P=200 torr, 17 mJ/pulse).

5.8.2 H_2-He

The following two sections discuss experimental results in H_2-He and O_2-He mixtures, since the model has not been exercised at these conditions. Portions of the discussion on the H_2-He mixtures presented here are taken from reference [53]. All results presented here were taken in P=100 torr gas mixtures. Figure 5.40 shows time-resolved electron density values obtained in H_2-He mixtures at the discharge conditions of figures 5.14-5.16, which plot pulse voltage, current and coupled energy

waveforms at these conditions. Similar trends to the results in helium at higher coupled energy can be observed. An initial, rapid electron density rise over the first 100 ns of the discharge pulse is observed in all cases. This is followed by a partial decay, and then by a second peak, due to the secondary pulse produced by the high-voltage pulse generator, before decaying in the afterglow. Peak electron densities range from $1.8{\cdot}10^{14}$ cm^{-3} (5% H_2 in He) to $3.3{\cdot}10^{14}$ cm^{-3} (He).

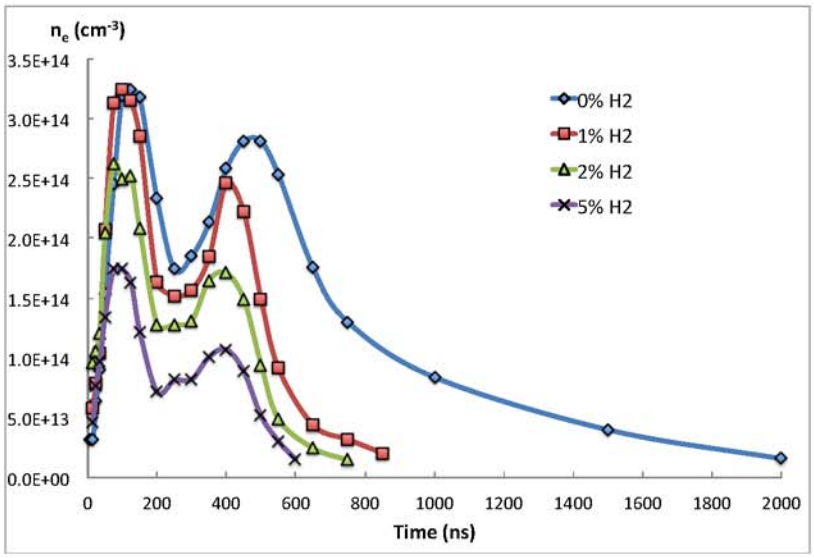

Figure 5.40: Time-resolved electron number density in H_2-He mixtures at the discharge conditions of figures 5.14-5.16 (P=100 torr, ≈4 mJ/pulse). From reference [53].

In helium, the temporal decay is relatively slow, such that the electron density decay time after the discharge pulse (by one order of magnitude) is approximately 2 μs. As the H_2 mole fraction in the mixture is increased, electron density decays consistently more rapidly. The dominant electron-ion recombination processes for the present experimental conditions are shown by eqns. 5.24-5.26. More rapid electron

density decay at higher H_2 mole fractions is likely due to more rapid dissociative recombination of electrons with H_2^+ and H_3^+ ions (eqns. 5.25,5.26) [49]. These processes are significantly faster (by up to an order of magnitude [25]) compared to dissociative recombination of electrons with He_2^+ ions (eqn. 5.24).

$$He_2^+ + e^- \rightarrow He^* + He \tag{5.24}$$

$$H_2^+ + e^- \rightarrow H + H(3) \tag{5.25}$$

$$H_3^+ + e^- \rightarrow H + H + HorH_2 + H(2) \tag{5.26}$$

Figures 5.41 and 5.42 show time-resolved electron temperatures in H_2-He mixtures at the discharge conditions of figures 5.14-5.16. Figure 5.41 plots electron temperature during the first 200 ns after the beginning of the discharge current pulse (i.e. before the secondary pulse), while figure 5.42 shows the full temporal evolution measured (including primary and secondary pulses). In all cases, there is a very rapid initial increase in electron temperature, within several nanoseconds after the start of the current rise, which cannot be resolved with the current diagnostic. Peak electron temperature values range from 2.6 eV (5% H_2 in He) to 7 eV (pure helium).

Between the pulses in the two-pulse waveform, the electron temperature decays rapidly until additional energy is added by the secondary pulse. During the secondary pulse, a second, slower electron temperature rise is observed (due to slower respective increase in pulse voltage), before the electron temperature reduces once again. It can be seen that the electron temperature decays approximately to the same level ($\approx$0.3 eV) after the primary and secondary pulses, roughly 250 ns after the respective voltage peaks. This is significantly higher compared to the initial gas temperature ($\approx$300 K) and suggests that the electrons are heated in superelastic collisions between electrons

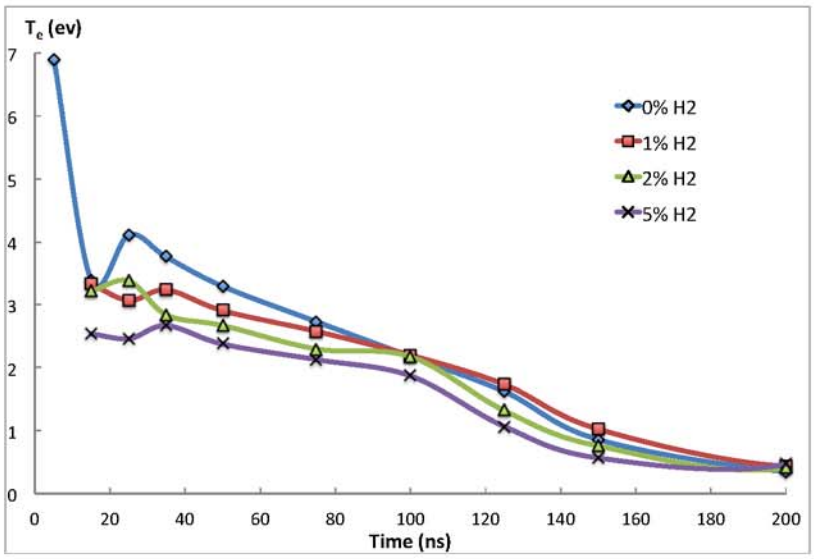

Figure 5.41: Time-resolved (0 ns-200 ns) electron temperature in H_2-He mixtures at the discharge conditions of figures 5.14-5.16 (P=100 torr, ≈4 mJ/pulse). From reference [53].

and metastable excited helium atoms and excimers in the short-term afterglow [49]. Similar to the helium data obtained at higher coupled energy, it can be observed that the electron temperature decays considerably more rapidly than the electron density. This is due to the fact that electrons lose energy more rapidly in every electron-neutral collision, while two-body and three-body recombination (the dominant mechanisms of electron density decay) occur on a significantly longer timescale, as discussed earlier in this section and in section 5.6. Lastly, as H_2 mole fraction is increased, the electron temperature in the plasma becomes somewhat lower (particularly during the primary pulse, when the current and voltage waveforms are comparable in all mixtures). Also, it should be noted that the difference in timing for the electron temperature rise during the secondary pulse is due to the difference between the current and voltage traces for the different mixtures used (see figures 5.14 and 5.15).

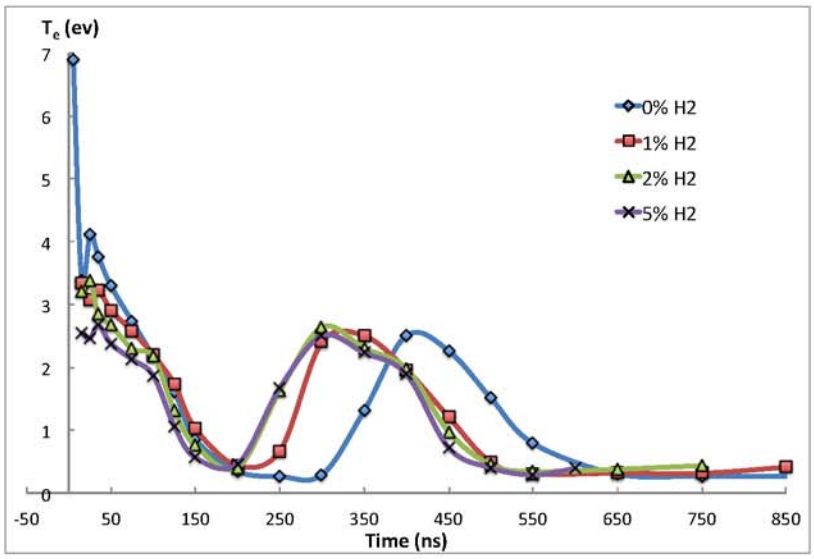

Figure 5.42: Time-resolved (0 ns-1 μs) electron temperature in H_2-He mixtures at the discharge conditions of figures 5.14-5.16 (P=100 torr, $\approx$4 mJ/pulse). From reference [53].

Figures 5.43-5.50 plot the time-resolved Maxwellian EEDFs in H_2-He mixtures, inferred from the electron temperature and number density data plotted in figures 5.42 and 5.40, respectively. Figures 5.43 and 5.44 show the EEDFs in helium, for the early (t = 5 ns - 150 ns) and late (t = 200 ns - 2 μs) timescales, respectively. Similar to the results obtained in helium with high coupled pulse energy, these EEDFs initially have a well-pronounced, high-energy tail, until electron temperature becomes lower as the electrons lose energy in the afterglow. After approximately 750 ns (i.e. shortly after the secondary pulse), the EEDF shape no longer changes significantly. Only the EEDF peak (around 0.3 eV) decreases slightly after this point. These results suggest that very high energy electrons are present very early during the pulse (at $t \approx 5$ ns), with energies up to $\approx$30 eV, with relative population of 10^{-3} in the tail. A significant

shift toward the low-energy part of the EEDF is observed to begin at ≈125 ns, which is the end of the primary pulse.

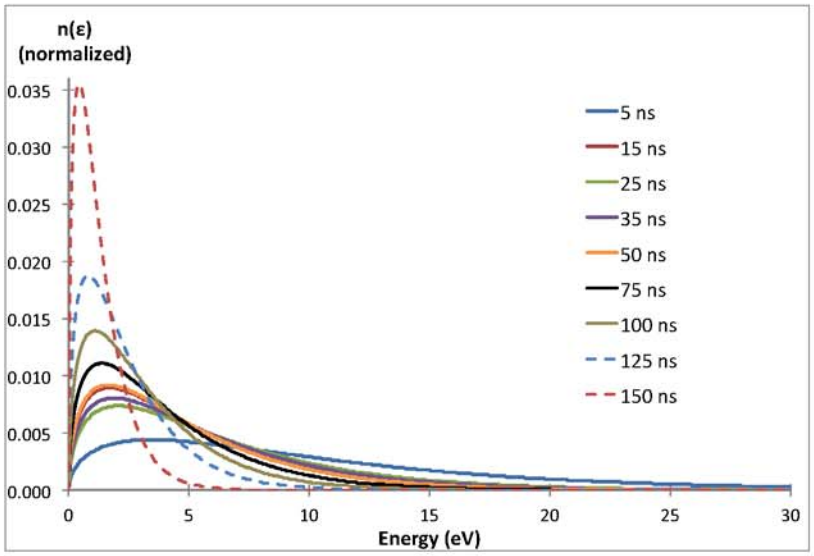

Figure 5.43: Time-resolved Maxwellian EEDFs for t = 5 ns-150 ns in helium at the discharge conditions of figures 5.14-5.16 (P=100 torr, ≈5 mJ/pulse).

In figure 5.44, EEDFs corresponding to the time range from t = 350 ns - 650 ns after the beginning of the discharge pulse regain a high-energy tail, indicating electron heating by the field. This corresponds to the time regime during the secondary pulse, when additional energy is coupled to the plasma. Following this, the electrons begin to cool once more, resulting in progressively sharper and lower energy EEDF peaks.

Figures 5.45 and 5.46 plot the EEDFs for a 1% H_2 in He mixture, for the short time delays (t = 15 ns - 150 ns) and late time delays (t = 200 ns - 850 ns, after the primary current pulse rise), respectively. The same general trend as observed in helium can be seen here as well, with initial, high-energy tail EEDFs becoming progressively more confined to the low-energy region. The results suggest that the most pronounced

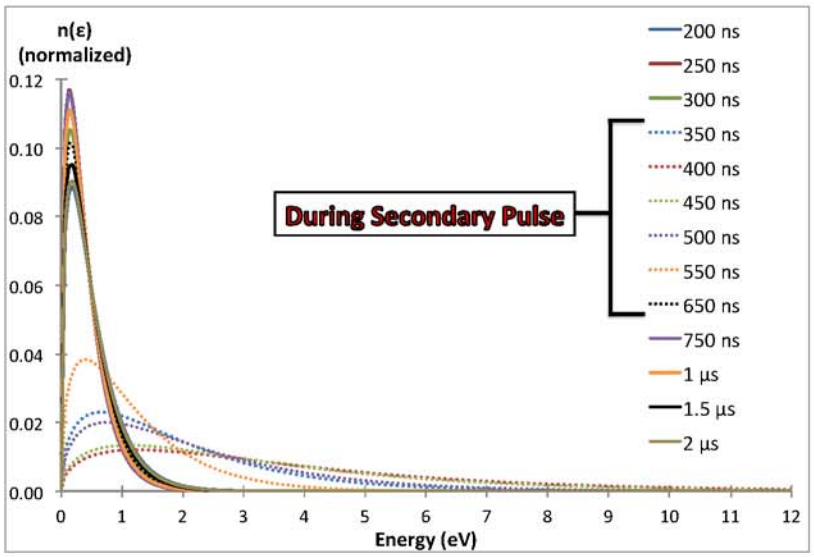

Figure 5.44: Time-resolved Maxwellian EEDFs for t = 200 ns-2 μs in helium at the discharge conditions of figures 5.14-5.16 (P=100 torr, ≈5 mJ/pulse).

high-energy tail, up to ≈20 eV, is formed at t = 15 ns. This is lower than in helium, but it should be noted that measurements in 1% H_2-He mixture started at t = 15 ns after the beginning of the primary current pulse rise in this case, and not t = 5 ns, as was the case in helium. Comparing EEDFs at t=15 ns for these two cases shows that the high-energy tails are comparable. One difference detected in the H_2-He mixture is that the electron temperature is higher (i.e. peak EEDF value is lower) at the same moments in time. This is discussed in greater detail later (see figures 5.51-5.54 and related discussion).

The secondary pulse in the 1%H_2-He mixture occurs at t = 250 ns-500 ns. The additional energy coupling, which increases electron temperature, causes the high-energy tail in the EEDF to reappear with electrons gaining higher energies, up to ≈12 eV (see figure 5.46) at these conditions. Measurements were obtained up to

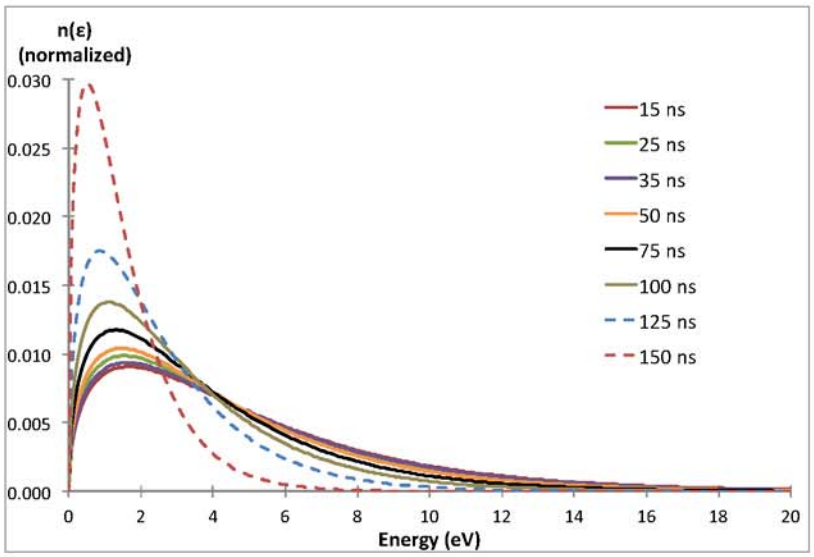

Figure 5.45: Time-resolved Maxwellian EEDFs for t = 15 ns-150 ns in 1% H_2-He mixture at the discharge conditions of figures 5.14-5.16 (P=100 torr, ≈4 mJ/pulse).

t = 850 ns after the start of the primary discharge current pulse. This time delay is significantly shorter than the longest time dealy used in helium, $t = 2$ μs due to lower electron densities in the H_2-He mixtures (i.e. lower Thomson scattering signal levels, below the detection limit of the present diagnostic). See figure 5.40 for the results of time-resolved density measurements at these conditions.

Figures 5.47 and 5.48 show EEDFs for 2% H_2 in He mixture, for the short (t = 15 ns - 150 ns) and long (t = 200 ns - 700 ns) delay times after the pulse current rise, respectively. Very similar trends to the results in helium and 1% H_2-He are observed. The results suggest that peak electron energies, up to $\epsilon \approx 20$ eV are present at t=15 ns. Notably, the results indicate that somewhat higher peak value EEDFs, compared to the 1% H_2-He mixture for short time delays (t = 15 ns - 200 ns), while the opposite trend is suggested (lower peak value, higher T_e EEDFs) at longer delay

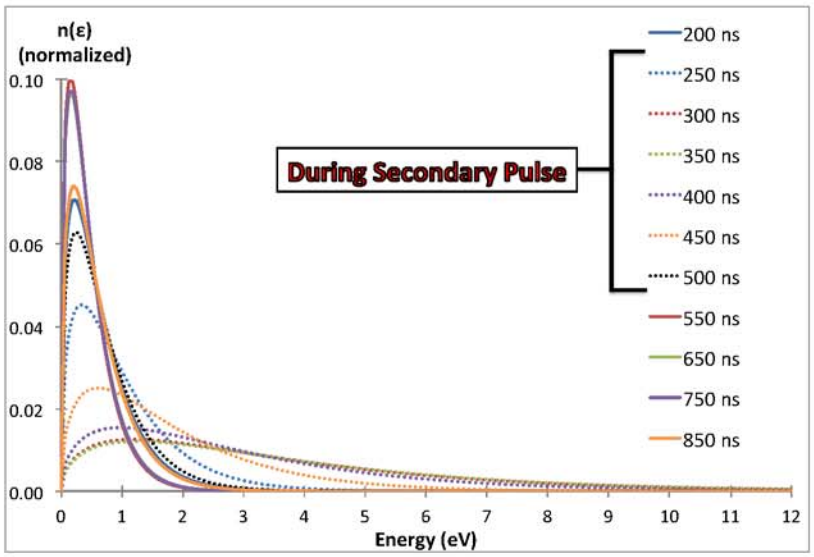

Figure 5.46: Time-resolved Maxwellian EEDFs for t = 200 ns-850 ns in 1% H_2-He mixture at the discharge conditions of figures 5.14-5.16 (P=100 torr, ≈4 mJ/pulse).

times, after the secondary pulse (t > 500 ns). This is explored further in the discussion of figures 5.51-5.54.

Figures 5.49 and 5.50 show the EEDFs for 5% H_2 in He mixture, for the short delays (t = 15 ns - 150 ns) and long delays (t = 200 ns - 600 ns) after the primary pulse current rise, respectively. Very similar trends to the mixtures with lower H_2 concentrations are observed. The results suggest that the highest electron energies, up to $\epsilon \approx 14$ eV, are significantly lower than at lower concentrations of H_2. Again, for short time delays (t = 15 ns - 200 ns) EEDFs have slightly higher peak values compared to the 2% H_2-He mixture, while for longer time delays (t > 500 ns) more pronounced, high-energy tail EEDFs are present.

Figures 5.51-5.54 compare EEDFs in different H_2-He mixtures for select time delays after the primary pulse current rise. Figure 5.51 shows the EEDFs for t=35,

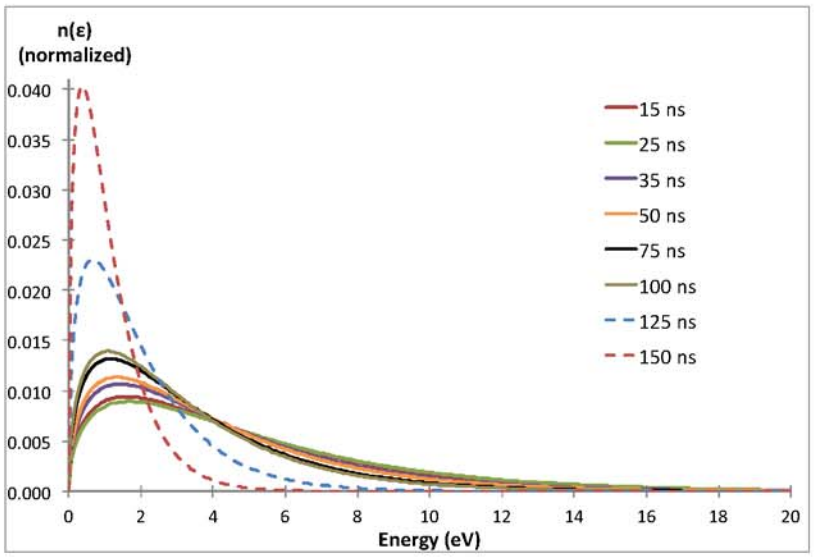

Figure 5.47: Time-resolved Maxwellian EEDFs for 15 ns-150 ns in 2% H_2-He mixture at the discharge conditions of figures 5.14-5.16 (P=100 torr, ≈4 mJ/pulse).

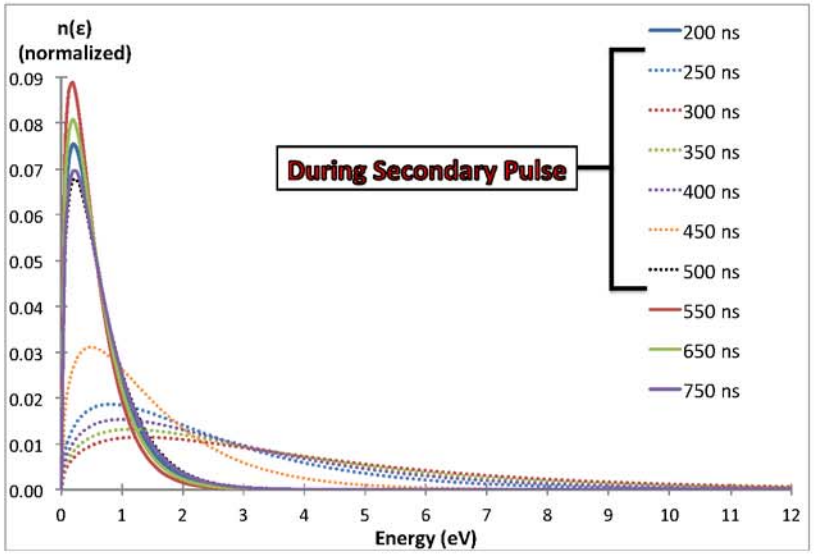

Figure 5.48: Time-resolved Maxwellian EEDFs for 200 ns-750 ns in 2% H_2-He mixture at the discharge conditions of figures 5.14-5.16 (P=100 torr, ≈4 mJ/pulse).

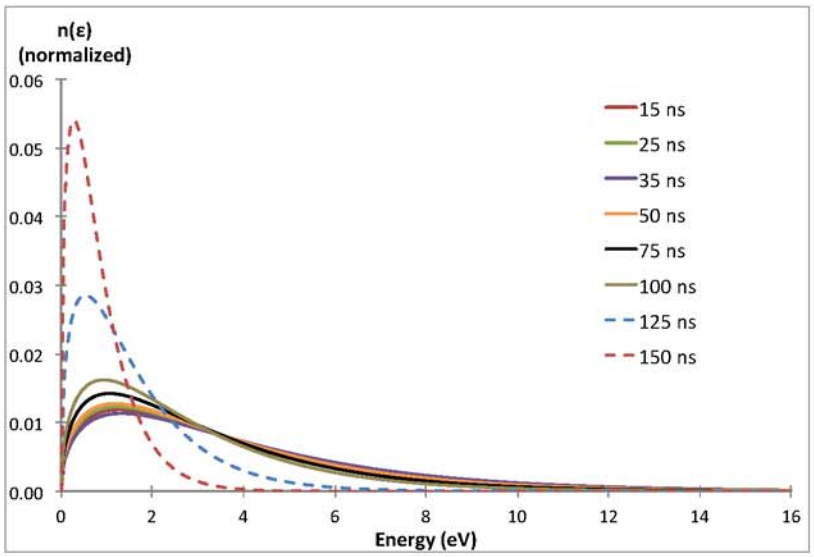

Figure 5.49: Time-resolved Maxwellian EEDFs for t = 15 ns-150 ns in 5% H_2-He mixture at the discharge conditions of figures 5.14-5.16 (P=100 torr, ≈4 mJ/pulse).

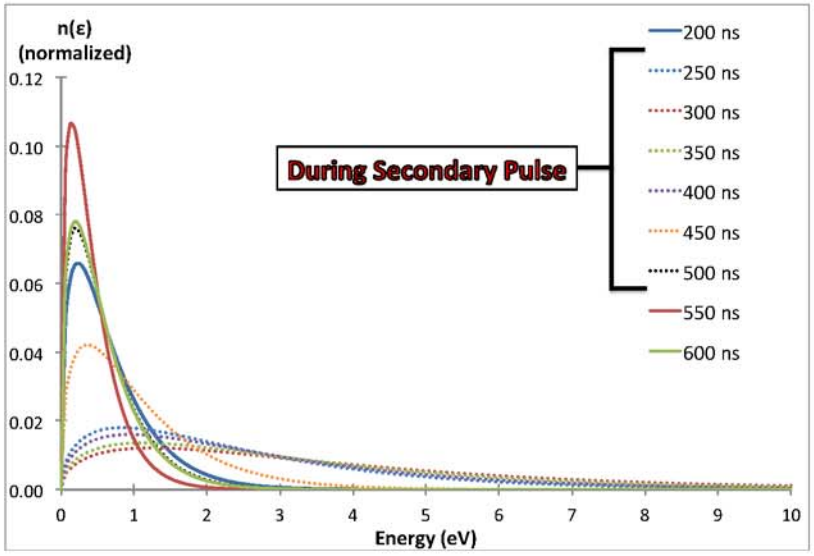

Figure 5.50: Time-resolved Maxwellian EEDFs for 200 ns-600 ns in 5% H_2-He mixture at the discharge conditions of figures 5.14-5.16 (P=100 torr, ≈4 mJ/pulse).

75, 125 ns, while figure 5.52 plots the EEDFs for t=200 ns and the time delay corresponding to the end of the secondary current pulse (which differs slightly for each gas mixture; see figure 5.15). Analyzing figure 5.51, for t=35 ns and t=75 ns, it can be concluded that with increasing H_2 fraction in the mixture, the electron temperature is decreasing such that the EEDF peaks at lower electron energies. However, at t=125 ns, in a 1% H_2 mixture, the electron temperature is higher than in He at the same time delay, such that the electron energy distribution spreads out further toward higher energies. In mixtures with 2% and 5% H_2, the trend is reversed.

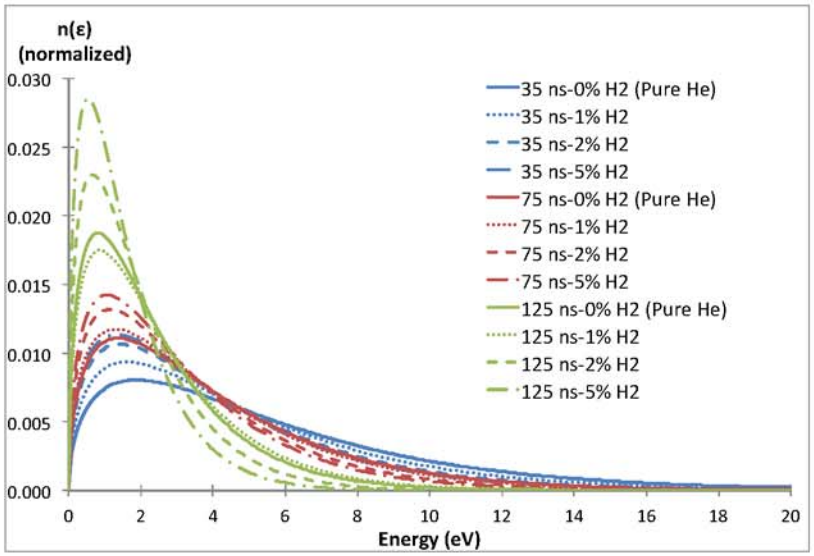

Figure 5.51: Maxwellian EEDFs at 35 ns, 75 ns and 125 ns (P=100 torr, ≈4-5 mJ/pulse) in different % H_2-He mixtures at the discharge conditions of figures 5.14-5.16.

Analyzing figure 5.52, it is concluded that at t=200 ns, the electron temperature increases as hydrogen is added to the mixture, such that the EEDF spreads out toward higher energies. At the moment in time immediately following the secondary pulse,

with the introduction of up to 2% H_2 the electron temperature increases causing the EEDF to spread further to higher energies. However, at higher concentration (5%), the EEDF tail begins to disappear since the electron temperature is lower.

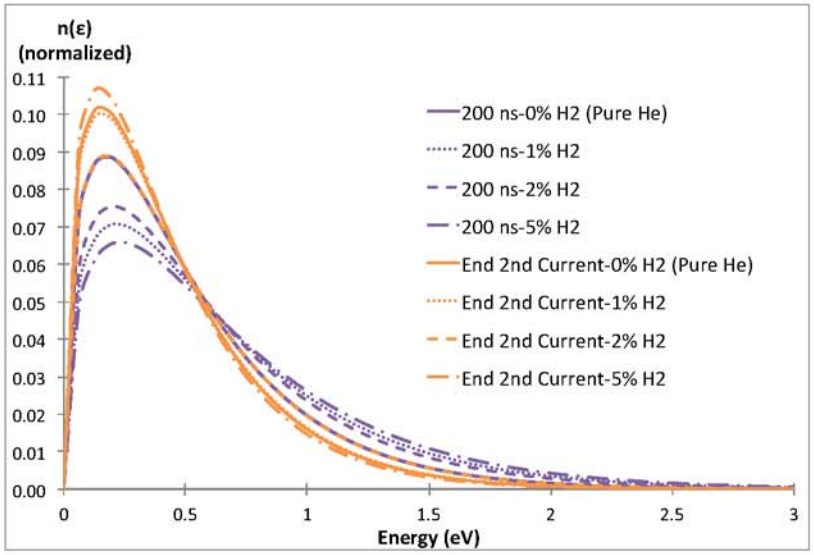

Figure 5.52: Maxwellian EEDFs for 200 ns and immediately following the secondary current pulse (P=100 torr, ≈4-5 mJ/pulse) in different H_2-He mixtures at the discharge conditions of figures 5.14-5.16.

Figures 5.53 and 5.54 plot the same EEDFs as in figures 5.51 and 5.52, but with the electron energy distribution divided by the square-root of the energy ($n(\epsilon)/\sqrt{\epsilon}$) and plotted on a semi-log scale. Plotting the exponential part of the EEDF on a semi-log scale illustrates a simple-to-analyze linear trend of the electron energy behavior. The same trends as discussed above can be observed here. Recall that based on the Gaussian fit to the Thomson spectrum (which assumes a Maxwellian EEDF), a Maxwellian EEDF can only be confirmed by the present experiments down to a relative population of 10^{-3} (see section 5.5). For relative populations below this

value (i.e. in the high energy tail of the EEDF), the present results are inconclusive, though in the plot the full EEDFs are shown as Maxwellian.

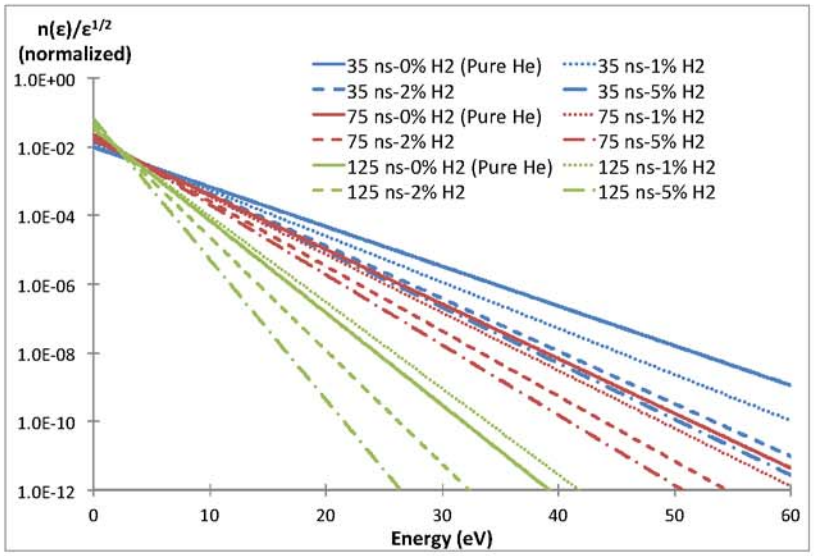

Figure 5.53: Exponential part of the Maxwellian EEDFs, $n(\epsilon)/\sqrt{\epsilon}$, plotted on a semi-logarithmic scale for t=35 ns, 75 ns and 125 ns in % H_2-He mixtures at the discharge conditions of figures 5.14-5.16 (P=100 torr, ≈4-5 mJ/pulse).

As a reminder, note that the EEDFs plotted in figures 5.43-5.54 are based on the following two assumptions: (1) the shape of the EEDF is Maxwellian, which is consistent with the spectral shape of the Thomson scattering spectra measured (i.e. they are accurately represented by a Gaussian spectral lineshape) at the present conditions (see figure 5.25), and (2) Maxwellian EEDF is maintained up to high electron energies ($\epsilon \gg T_e$). The present experiments do not provide direct evidence for this second assumption, due to limited signal-to-noise. Further kinetic modeling calculations, predicting EEDF by solving the Boltzmann equation for the plasma electrons would help to clarify the validity of this assumption.

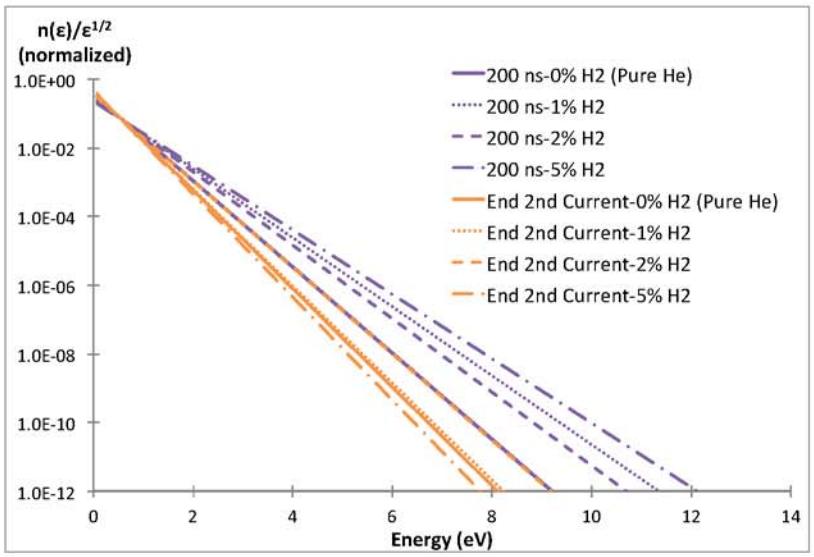

Figure 5.54: Exponential part of the Maxwellian EEDFs, $n(\epsilon)/\sqrt{\epsilon}$, plotted on a semi-logarithmic scale for t=200 ns and immediately following the secondary current pulse in % H_2-He mixtures at the discharge conditions of figures 5.14-5.16 (P=100 torr, ≈4-5 mJ/pulse).

5.8.3 O_2-He

Portions of the discussion presented here on the results obtained in O_2-He mixtures is taken from reference [53]. Figure 5.55 shows time-resolved electron density measured in O_2-He gas mixtures at the discharge conditions shown in figures 5.20-5.22, which plot discharge pulse voltage, current and coupled energy waveforms. Similar temporal trends to the H_2-He mixtures are observed. Peak electron density values range from $1.7{\cdot}10^{14}$ cm^{-3} (10% O_2 in He) to $3.5{\cdot}10^{14}$ cm^{-3} (helium and 1% O_2 in He). Similar to H_2-He mixtures, as the O_2 mole fraction in the mixtures is increased, the electron density decays more rapidly. However, in this case, it is likely that three-body electron attachment to oxygen plays a primary role in electron decay,

$$e^- + O_2 + M \rightarrow O_2^- + M \tag{5.27}$$

since it is a known rapid electron removal process in oxygen-containing plasmas at low to moderate (T<500 K) translational/rotational temperatures, as is likely the case here. The characteristic time for O_2 attachment was calculated earlier in section 5.6 as $\tau_{O_2-attachment} \approx 3-4$ μs (see equations 5.18-5.19).

Three-body attachment, unlike dissociative attachment (eqn. 2.19), which has an electron energy threshold of ≈4.2 eV, does not require high electron energies, and occurs even after the electrons are thermalized. In fact, the rate coefficient of this process increases at low electron temperatures [25].

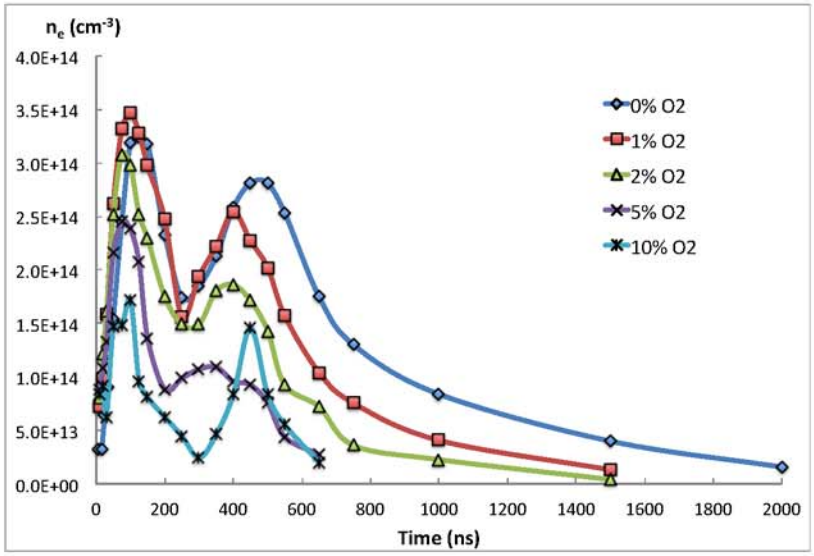

Figure 5.55: Time-resolved electron number density in O_2-He mixtures at the discharge conditions shown in figures 5.20-5.22 (P=100 torr, ≈4 mJ/pulse). From reference [53].

Figures 5.56 and 5.57 show time-resolved electron temperature in O_2-He mixtures. Figure 5.56 shows a zoomed-in plot of electron temperatures during the first 200 ns after the beginning of the current rise (i.e. before the secondary pulse), while

figure 5.57 shows the full temporal evolution (including both primary and secondary pulses). The temporal trends are very similar to those in the H_2-He mixtures (shown in figure 5.42). Peak electron temperature values range from 2.9 eV (10% O_2 in He) to 7.0 eV (pure helium). Electron temperature, once again, decreases to the same level, $\approx$0.3 eV, after both the primary and secondary pulses. Similar to H_2-He mixtures, the difference in timing for the electron temperature rise during the secondary discharge pulse is due to the difference between the current and voltage traces for different mixtures (see figures 5.20 and 5.21).

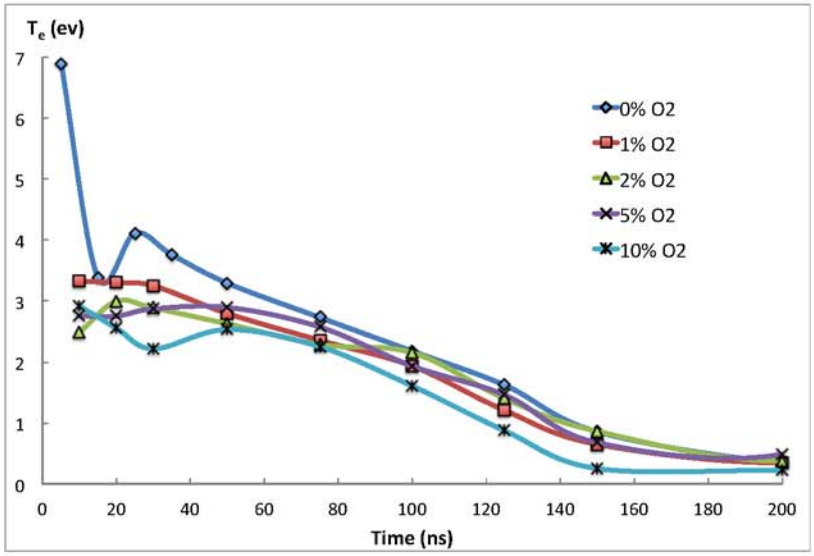

Figure 5.56: Time-resolved (t = 0 ns-200 ns) electron temperature in O_2-He mixtures at the discharge conditions shown in figures 5.20-5.22 (P=100 torr, $\approx$4 mJ/pulse). From reference [53].

Figures 5.58-5.65 plot time-resolved Maxwellian EEDFs in the O_2-He gas mixtures. EEDFs measured in helium at moderate coupled pressure (5 mJ/pulse, P=100 torr) have been previously shown in Figures 5.43 and 5.44. Figures 5.58 and 5.59 plot

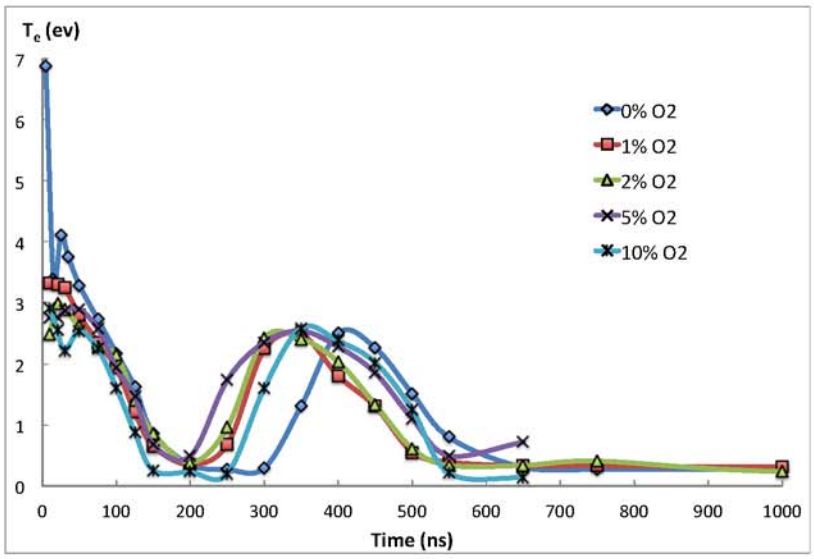

Figure 5.57: Time-resolved electron temperature in O_2-He mixtures at the discharge conditions shown in figures 5.20-5.22 (P=100 torr, ≈4 mJ/pulse). From reference [53].

EEDFs in 1% O_2-He mixture for the short (t = 10 ns - 150 ns) and long (t = 200 ns - 1.5 μs) time delays, respectively. Similar to the results in the H_2-He mixtures, these EEDFs exhibit initially high-energy tails, before becoming more concentrated at lower energies, as the electrons cool in the afterglow between the pulses. The results suggest that the highest energy electrons are present at the shortest time delay (t=10 ns), with energies up to ≈16 eV. This is somewhat lower than in the comparable case in hydrogen (1% H_2-He mixture), which indicates electron energies of up to ≈20 eV (see figure 5.45). A significant electron temperature reduction, indicating a shift toward an EEDF with a less pronounced high-energy tail, is observed at t ≈125 ns, which is the end of the primary pulse.

In figure 5.59, the results suggest that a number of EEDFs (corresponding to the time delays ranging from t=250 ns-500 ns after the start of the primary discharge

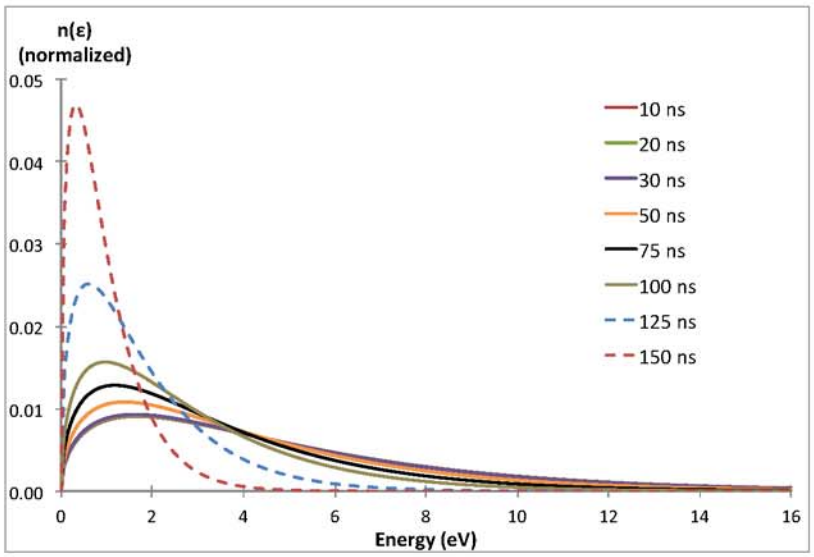

Figure 5.58: Time-resolved Maxwellian EEDFs for t=10 ns-150 ns in 1% O_2-He mixture at the discharge conditions shown in figures 5.20-5.22 (P=100 torr, ≈4 mJ/pulse).

current pulse) exhibit high-energy tails, up to ≈12 eV, indicating significant electron heating. This corresponds to the time regime during the secondary discharge pulse, when additional energy is coupled to the plasma. Following this, the electrons begin to cool once again in the afterglow, resulting in progressively higher peak, lower energy EEDFs.

Figures 5.60 and 5.61 show EEDFs in the 2% O_2 in He mixture, for the short (t=10 ns - 150 ns) and late (t=200 ns - 1.5 μs) time delays after the primary current pulse, respectively. Very similar trends to the results in the 1% O_2-He mixture are observed. The results suggest that the highest energy electrons, up to $\epsilon \approx 16$ eV, are present at t=10 ns. Notably, lower peak value EEDFs corresponding to higher electron temperatures than in the 1% O_2-He mixture are present for the short time delays (t=15 ns - 200 ns), while the opposite effect occurs (higher peak value, lower

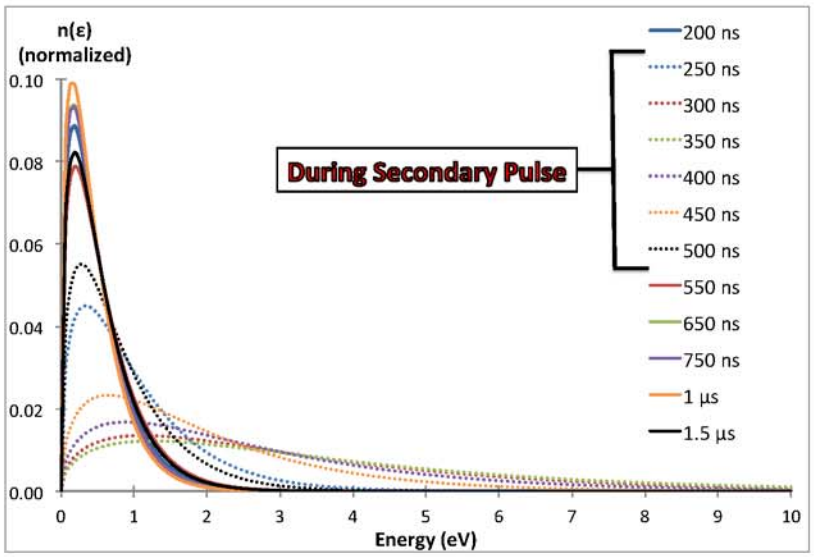

Figure 5.59: Time-resolved Maxwellian EEDFs for t=200 ns-1.5 μs in 1% O_2-He mixture at the discharge conditions shown in figures 5.20-5.22 (P=100 torr, $\approx$4 mJ/pulse).

electron temperature EEDFs) for longer time delays, after the secondary pulse (t > 500 ns). This trend is opposite to the one in 1% and 2% H_2-He mixtures, and indicates that the presence of oxygen results in higher electron temperatures at shorter timescales (t<200 ns), while the presence of hydrogen seems to have a similar effect, but on longer timescales (t>500 ns). EEDF trends in O_2-He mixtures are analyzed further in the discussion of figures 5.66-5.69.

Figures 5.62 and 5.63 show EEDFs in the 5% O_2 in He mixture, for the short (t=10 ns - 150 ns) and long (t=200 ns - 650 ns) time delays after the primary pulse current rise, respectively. Similar trends as in the lower O_2 concentration mixtures are observed. The results suggest that the highest energy electrons are present at t=10ns, up to $\epsilon \approx 14$ eV. At short delay time (t=15 ns - 200 ns), EEDF peak values are slightly higher compared to the 2% O_2 mixture (i.e. lower electron temperatures), while at

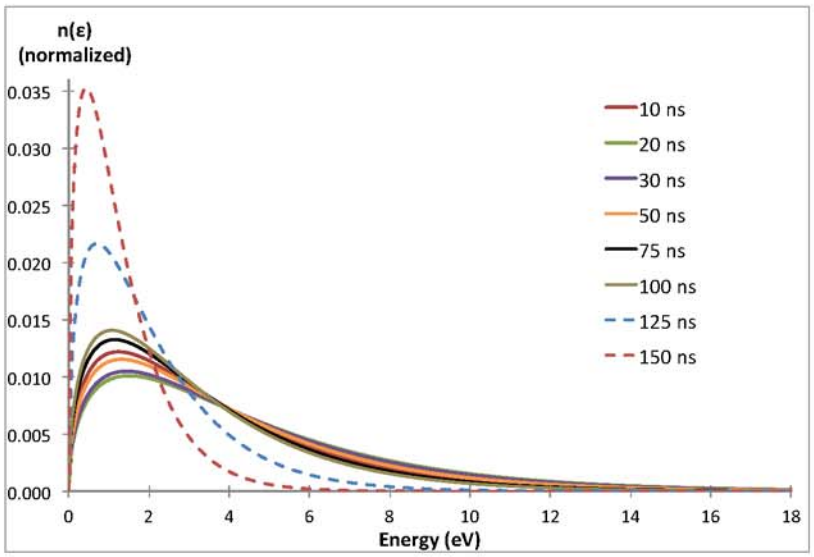

Figure 5.60: Time-resolved Maxwellian EEDFs for 10 ns-150 ns in 2% O_2-He mixture at the discharge conditions shown in figures 5.20-5.22 (P=100 torr, ≈4 mJ/pulse).

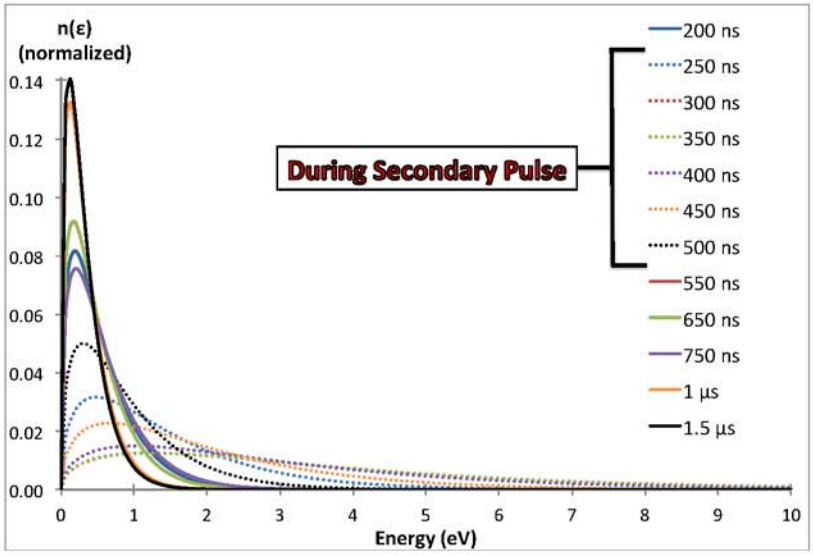

Figure 5.61: Time-resolved Maxwellian EEDFs for 200 ns-1.5 μs in 2% O_2-He mixture at the discharge conditions shown in figures 5.20-5.22 (P=100 torr, ≈4 mJ/pulse).

long delay times (t > 500 ns), electron temperatures in the 5% O_2-He mixture are higher, resulting in energy distributions exhibiting a more pronounced, high-energy tail. This is a reversal of the trend observed between 1% adn 2% O_2-He mixtures. In the 5% O_2-He mixture, the electron density and electron temperature measurements were conducted only out to t=650 ns, while measurements in 1% and 2% O_2 in He mixtures were done for time delays up to t=1.5 μs. This is due to lower Thomson signal levels in the 5% O_2-He mixture, as a result of lower electron densities.

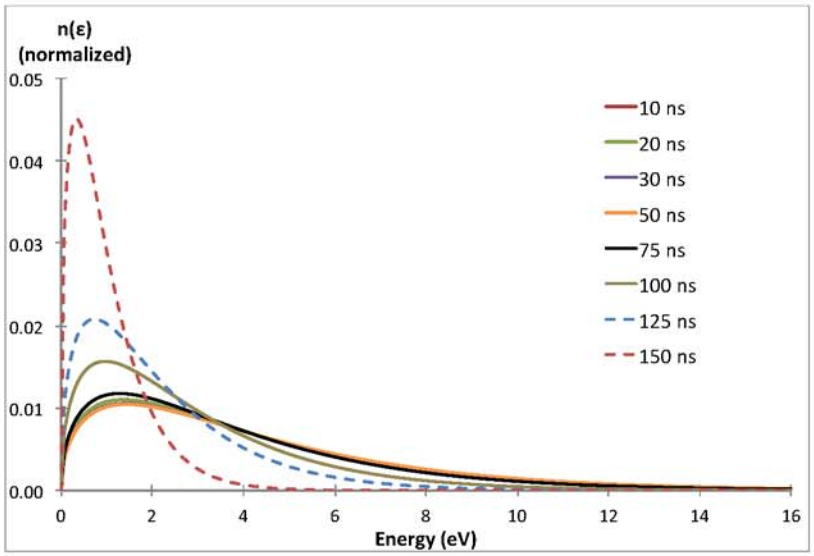

Figure 5.62: Time-resolved Maxwellian EEDFs for 10 ns-150 ns in 5% O_2-He mixture at the discharge conditions shown in figures 5.20-5.22 (P=100 torr, ≈4 mJ/pulse).

Figures 5.64 and 5.65 show EEDFs for the 10% O_2 in He mixture, for the short time (t=10 ns - 150 ns) and long time (t=200 ns - 650 ns) delays, respectively. Very similar trends to the 5% O_2 concentration are observed. The results suggest that high energy electrons, up to $\epsilon \approx 10$ eV, are present in the mixture at t=10 ns. This is significantly lower than with lower O_2 concentrations. For short delays (t=10 ns

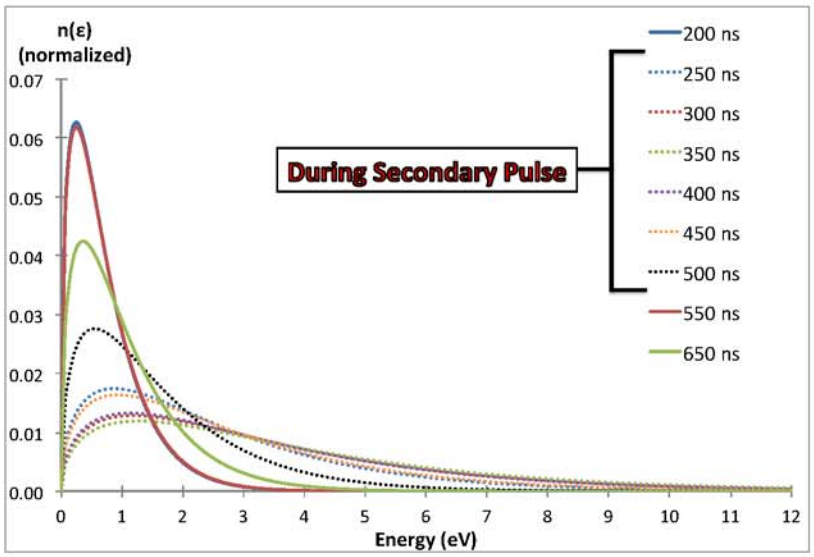

Figure 5.63: Time-resolved Maxwellian EEDFs for 200 ns-650 ns in 5% O_2-He mixture at the discharge conditions shown in figures 5.20-5.22 (P=100 torr, ≈4 mJ/pulse).

- 200 ns), EEDF peak values are slightly higher (i.e. lower electron temperature) compared to the 5% H_2 case, while later (t > 500 ns), energy distributions exhibit higher-energy tails, reversing this trend.

Figures 5.66-5.69 show EEDFs in O_2-He mixtures for select time delays after the primary pulse. Figure 5.66 plots EEDFs for t=35, 75, and 125 ns, while 5.67 plots EEDFs for t=200 ns and the moment in time corresponding to the end of the secondary current pulse (which differs slightly for each gas mixture; see figure 5.21). Analyzing figure 5.66, for t=35 ns, it can be observed that as O_2 fraction in the mixture increases, the EEDF peak value increases, which corresponds to lower electron temperatures. However, for t=75 ns and t=125 ns, while the results in low

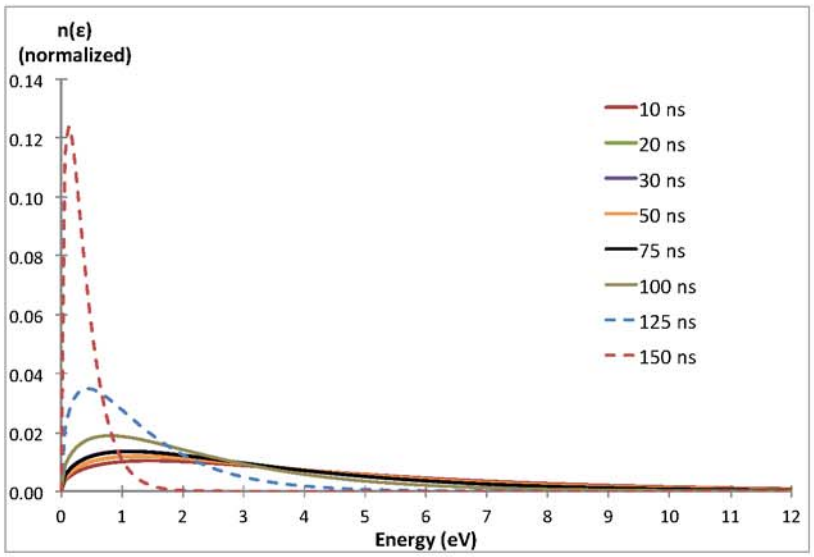

Figure 5.64: Time-resolved Maxwellian EEDFs for 10 ns-150 ns in 10% O_2-He mixture at the discharge conditions shown in figures 5.20-5.22 (P=100 torr, ≈4 mJ/pulse).

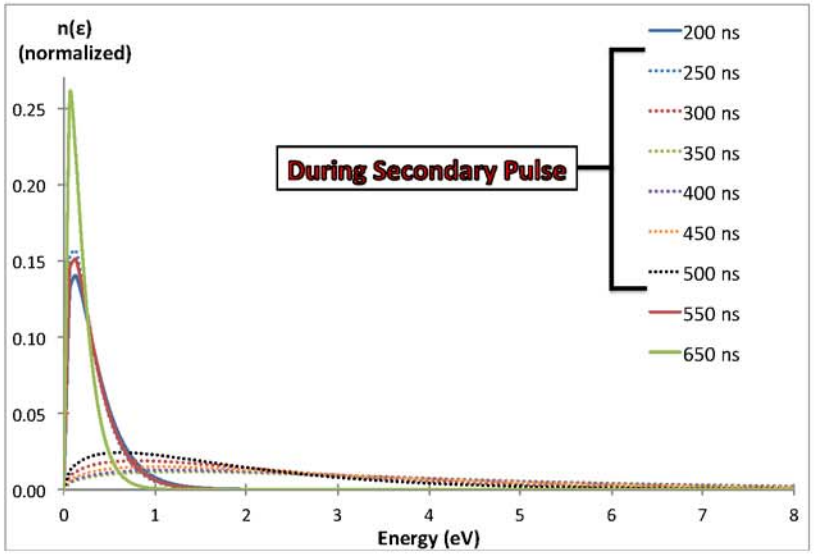

Figure 5.65: Time-resolved Maxwellian EEDFs for 200 ns-650 ns in 10% O_2-He mixture at the discharge conditions shown in figures 5.20-5.22 (P=100 torr, ≈4 mJ/pulse).

oxygen fraction mixtures (1% and 2% O_2) show the same trend of lower average energy EEDFs, at 5% and 10% O_2-He mixtures, this trend is reversed, and the EEDFs exhibit a high-energy tail once again.

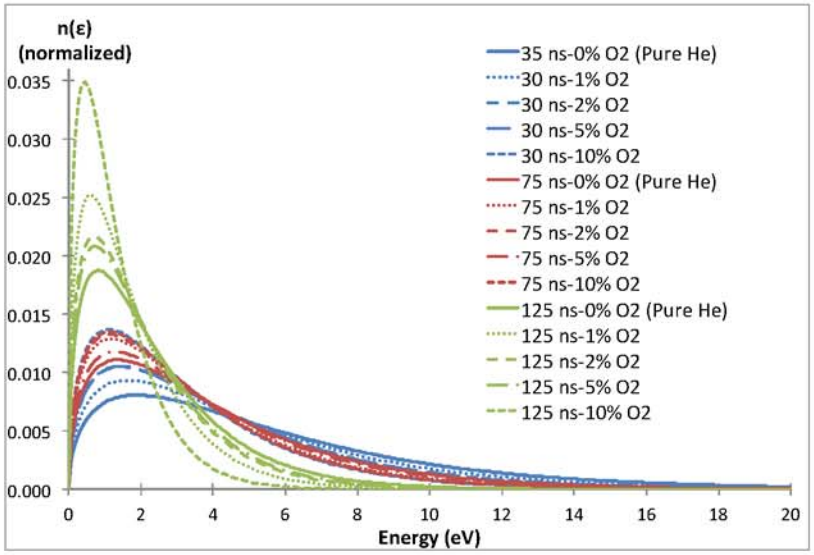

Figure 5.66: Maxwellian EEDFs in % O_2-He mixtures for t=30 ns, 75 ns and 125 ns at the discharge conditions shown in figures 5.20-5.22 (P=100 torr, ≈4-5 mJ/pulse).

Analyzing figure 5.67, at t=200 ns, the EEDF shows essentially no change between helium and 1% O_2-He mixture. However, at 2% and 5% O_2 in He, the EEDF exhibits a more pronounced high-energy tail, before this trend is reversed, and low average energy EEDF is present at 10% O_2 in helium. At the moment immediately following the secondary pulse, a similar trend can be observed, although the EEDF appears to have a higher average energy in a low percentage O_2-He mixture (1% O_2).

Figures 5.68 and 5.69 show the same EEDFs as in figures 5.66 and 5.67, but with the electron energy distribution divided by the square-root of the energy, $(n(\epsilon)/\sqrt{\epsilon})$, and plotted on a semi-log scale, providing simpler-to-analyze linear trends of the

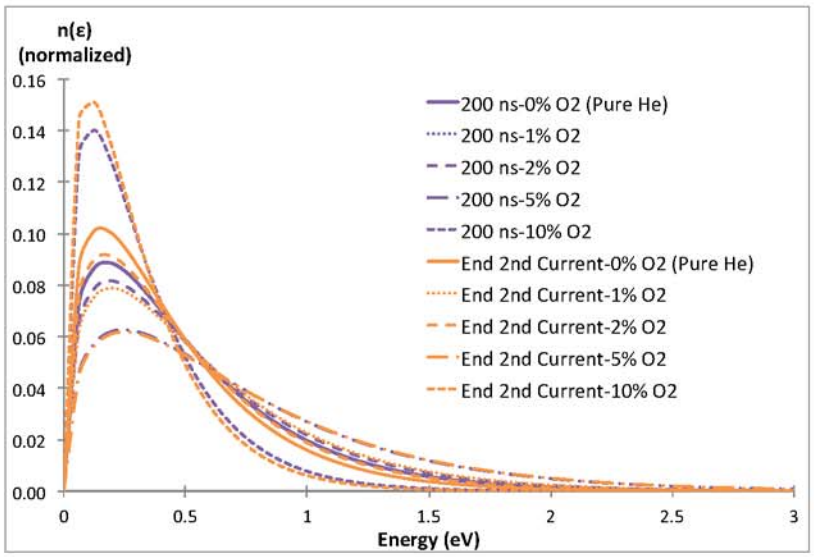

Figure 5.67: Maxwellian EEDFs in % O_2-He for t=200 ns and immediately following the secondary current pulse at the discharge conditions shown in figures 5.20-5.22 (P=100 torr, ≈4-5 mJ/pulse).

electron energy behavior. The same trends as discussed previously can be observed here. Recall that based on the Gaussian fit to the Thomson spectrum (which assumes a Maxwellian EEDF), a Maxwellian EEDF can only be confirmed by the present experiments down to a relative population of 10^{-3} (see section 5.5). For relative populations below this value (i.e. in the high energy tail of the EEDF), the present results are inconclusive, though in the plot the full EEDFs are shown as Maxwellian. It is clear that comparison of the present results with kinetic modeling would yield insight into the shape of the EEDF in O_2-He mixtures (especially in the high-energy tail), and help to clarify the validity of the assumptions made in the present work.

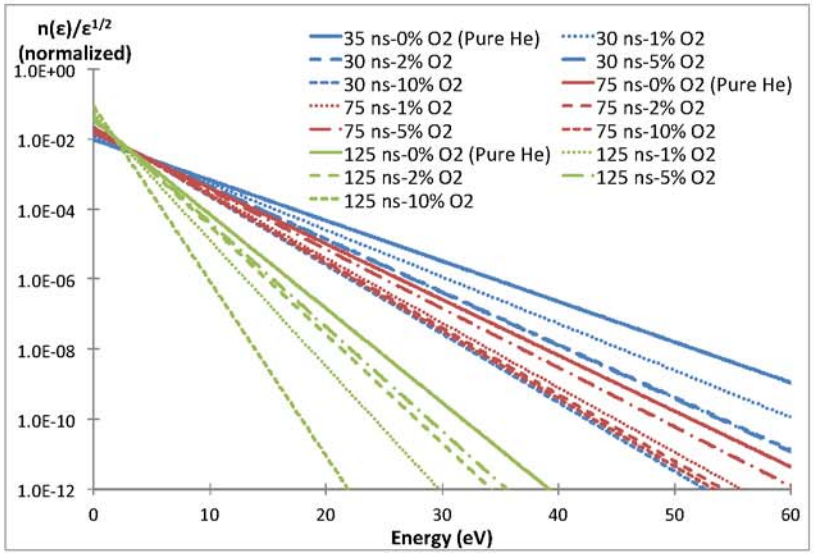

Figure 5.68: Exponential part of the EEDF in % O_2-He mixtures, $n(\epsilon)/\sqrt{\epsilon}$, plotted on a semi-logarithmic scale for t=30 ns, 75 ns and 125 ns at the discharge conditions shown in figures 5.20-5.22 (P=100 torr, ≈4-5 mJ/pulse).

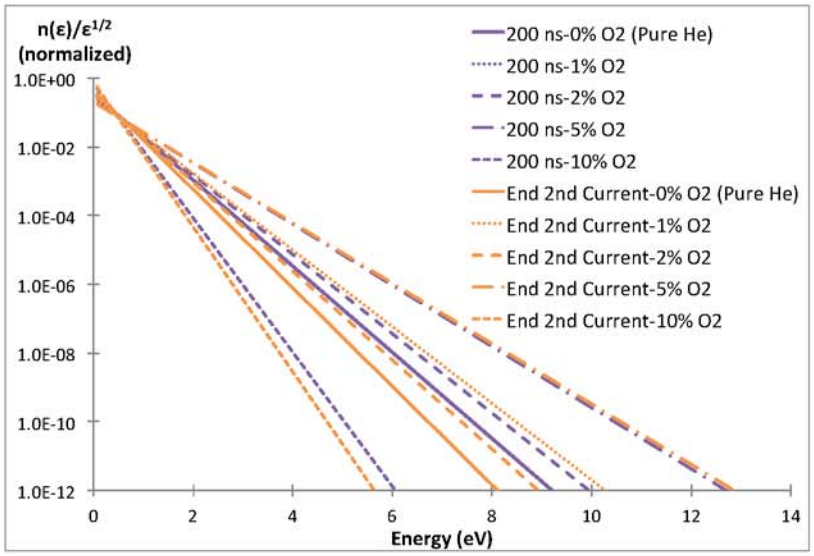

Figure 5.69: Exponential part of the EEDF in % O_2-He mixtures, $n(\epsilon)/\sqrt{\epsilon}$, plotted on a semi-logarithmic scale for 200 ns and immediately following the secondary current pulse at the discharge conditions shown in figures 5.20-5.22 (P=100 torr, ≈4-5 mJ/pulse).

5.9 Near Surface Nanosecond Pulse Discharge: Experimental Conditions

This section outlines the Thomson scattering experiment conducted in a near surface, nanosecond pulse discharge generating a surface ionization wave. These experiments were conducted in pure helium at P=100 torr. Measurements taken include temporally resolved electron number density, electron temperature and electron energy distribution (EEDF).

5.9.1 Near Surface Nanosecond Pulse Discharge: Apparatus

The near surface discharge experiment was conducted in an environment very similar to that outlined in chapter 4 and section 5.1. The only differences are the electrode setup, housed at the center of the glass test cell, and the resulting discharge geometry. Figure 5.70 shows a photograph of the glass test cell, with an inset in the upper-left corner, showing the central part of the glass test cell (six-arm cross), with the surface discharge assembly placed inside.

Figure 5.71 shows a more detailed schematic of the discharge electrode setup. The surface discharge assembly consists of a rectangular quartz channel, held in place by two plastic (Delrin), custom-machined inserts, which hold the assembly inside the glass test cell. Within the quartz channel, the electrodes are attached to the bottom surface of the channel. The electrodes are made of adhesive copper tape (0.1 mm thick) and are positioned 17 mm apart. Adhesive copper tape used for the grounded electrode is also attached to the outside surface of the bottom wall of the quartz channel, which acts as a waveguide for the surface ionization wave which originates at the high-voltage electrode. The left electrode (high-voltage electrode) was powered

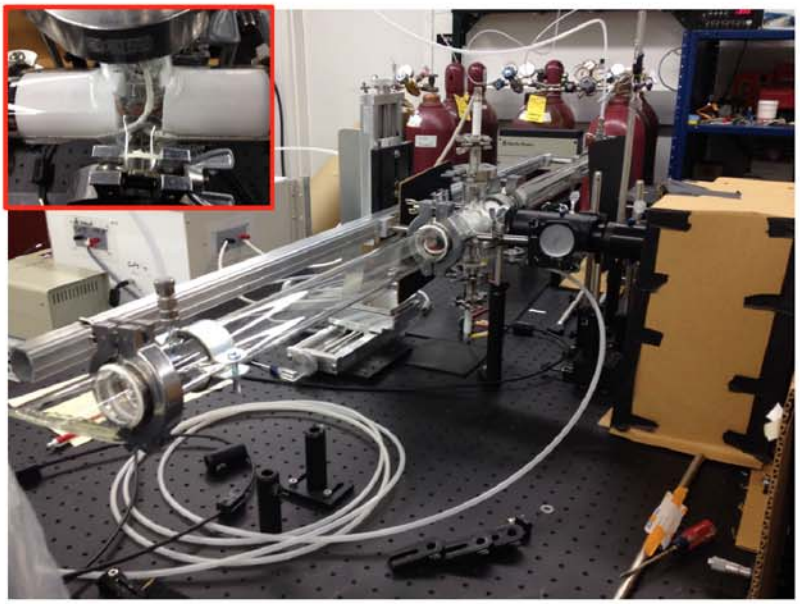

Figure 5.70: Image of experimental apparatus used in near-surface discharge experiment. From reference [48].

by the same, home-built, magnetic compression pulser as described previously (see section 5.1). A positive-polarity, double-pulse voltage waveform is produced, with a peak voltage of ≈6 kV and peak current of ≈80 A. The pulse duration is ≈150 ns; a pulse repetition rate of 120 Hz was used for this study. The resulting electric discharge is initiated as a relatively slow-moving (0.2 mm/ns) surface ionization wave, propagating from the high-voltage electrode (left) to the grounded electrode (right). Once the wave reaches the grounded electrode, a near surface, quasi-DC discharge is formed. Time resolved electron number density, electron temperature and EEDF measurements were obtained in this quasi-DC near surface discharge. Figure 5.71 shows a schematic (not to scale) of the near surface discharge (violet), and the laser

beam used for Thomson scattering measurements, propagating through the discharge (green).

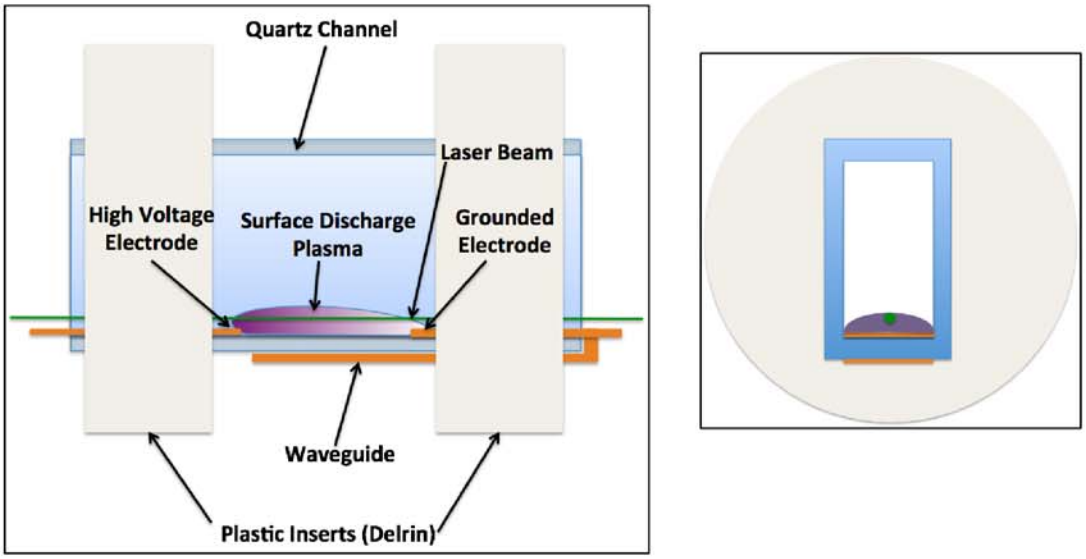

Figure 5.71: Schematic of near-surface discharge electrode setup. From reference [48].

5.9.2 Near Surface Nanosecond Pulse Discharge: Characteristics

Portions of this discussion are taken from reference [48]. Helium is flowed through the discharge test cell in the axial direction, at a pressure of P=100 torr and a flow rate of 1.75 slm, which corresponds to an estimated axial flow velocity of ≈0.5 m/s. This velocity is sufficiently high to ensure that the flow between the electrodes is refreshed between consecutive laser pulses (30 Hz). When the high voltage pulse is applied to the electrodes, a surface ionization wave forms at the high-voltage electrode. This wave then propagates across the gap until it reaches the grounded electrode. At this

point, a quasi-DC, near-surface discharge is generated between the electrodes, over the entire 17 mm gap. Based on ICCD images (see figure 5.73), the surface plasma is approximately 1.3 mm thick and 12 mm wide.

Figure 5.72 shows the pulse voltage, current and coupled energy waveforms at the present conditions. The DC input voltage to the pulse plasma generator was 475 V. Peak output pulse voltage and current are ≈6 kV and ≈80 A, respectively, with the double-pulse structure readily apparent. At the present conditions, the primary pulse couples approximately 80% of the energy to the plasma, 11 mJ, with the remaining ≈3 mJ coupled by the secondary pulse, resulting in a total coupled pulse energy of ≈14 mJ. In figure 5.72, $t = 0$ corresponds to the moment when the surface ionization wave is initiated and begins to propagate at the high-voltage electrode. This phenomenon is well reproduced shot-to-shot.

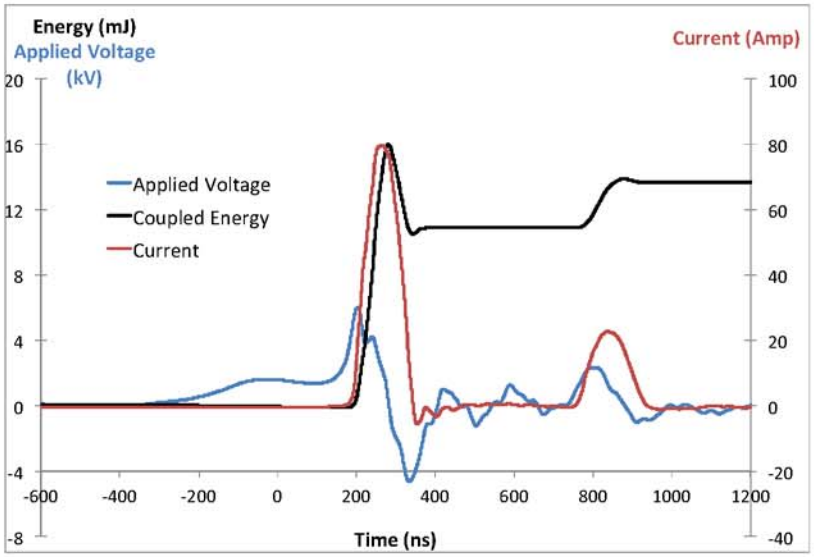

Figure 5.72: Voltage, current and **coupled energy** waveforms in the near surface, nanosecond pulse discharge (helium, P=100 torr). From reference [48].

Figure 5.73 shows a collage of ICCD images showing broadband plasma emission from the near-surface discharge (initiated as a surface ionization wave) and afterglow in helium during and after the high-voltage pulse. All images are accumulations over 5 discharge pulses, with a 2 ns camera gate, and are taken at the conditions of figure 5.72. To reiterate, $t = 0$ corresponds to the moment when the surface ionization wave was initiated at the high-voltage electrode. As can be observed from the images, the ionization wave propagates across the 17 mm gap between the electrodes and reaches the grounded electrode approximately 84 ns after it is initiated. The average wave speed is approximately 0.2 mm/ns. Furthermore, it can be seen that the pulse voltage peaks and begins to fall approximately 185 ns after the wave begins to propagate, i.e. about 100 ns after the wave reaches the grounded electrode. At this moment, the main pulse current begins to rise dramatically (see figure 5.72), indicating breakdown of the discharge gap and formation of a self-sustained discharge between the electrodes. Nearly all energy is coupled to the plasma after this moment. The pulse current peaks about 260 ns after the wave propagation begins. Thus, the surface ionization wave propagates across the entire discharge gap while the applied voltage is still fairly low (below 2 kV; see figure 5.72), and the discharge current at this stage is very low, as expected.

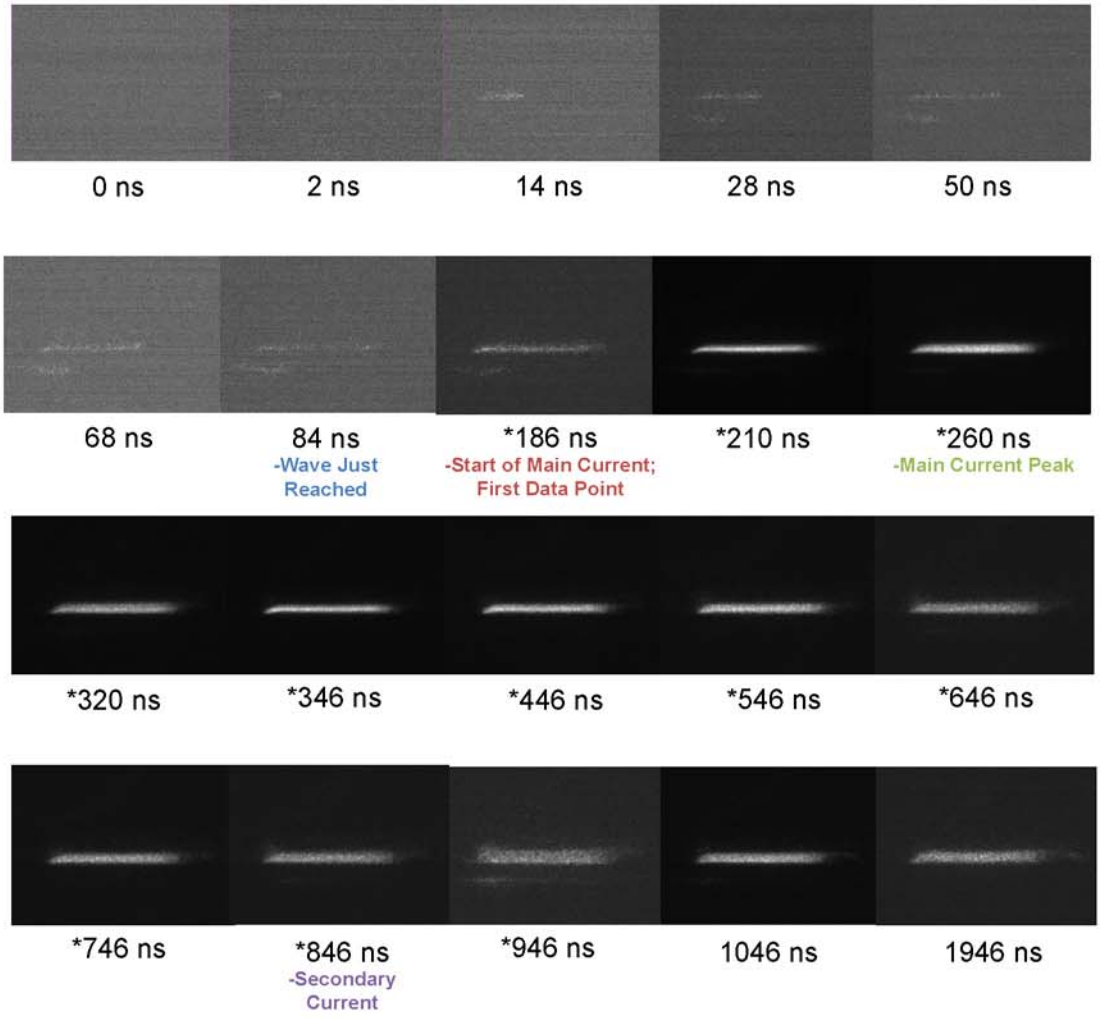

Figure 5.73: Broadband plasma emission for near surface discharge study (helium, P=100 torr, 5-shot average, 2 ns gate). Time delays shown are relative to the start of the surface ionization wave propagation (t=0). *Asterisks represent time delays for which Thomson spectra were collected. From reference [48].

5.9.3 Near Surface Nanosecond Pulse Discharge: Thomson Spectra

Portions of the following discussion are taken from reference [48]. Thomson scattering spectra were obtained for a range of time delays from 185 ns to 950 ns after the start of the surface ionization wave propagation. Accumulating spectra at shorter time delays, i.e. before a self-sustained discharge was established across the electrode gap, was attempted. However, the scattering signal was too weak to produce usable spectra (i.e. electron density in the plasma was too low, or possibly, the plasma was closer to the surface than the laser beam). For all time delays, the ICCD camera was set to collect several thousands of laser shots, in order to achieve signal-to-noise sufficient for data processing and inference of the electron density and electron temperature. For time delays between 185 ns and 240 ns, 45,000 laser shots (25 minute signal collection time) were accumulated and added together to create each 'exposure'. For all other time delays, 14,400 laser shots (8 minute signal collection time) were accumulated. To further improve signal-to-noise, 'exposures' for each time delay were collected 4 times and averaged. Finally, both discharge emission and stray light backgrounds were collected and subtracted from the averaged Thomson scattering spectrum, by turning off the laser and the discharge, respectively. A sample filtered Thomson scattering spectrum, after background subtraction, taken 315 ns after the start of the surface ionization wave propagation, is shown as the blue line in figure 5.74, along with the fitted Voigt lineshape and inferred Gaussian profile. For further information on the spectral fitting procedure, see section 5.2.

The Thomson scattering signal in the plasma was collected from an $\approx$50 μm diameter, 3 mm long volume. The signal collection volume was located halfway between

the electrodes, along the centerline of the plasma (i.e. laterally and longitudinally), approximately 1.1 mm above the dielectric (quartz) surface. This results in collection from a region which is ≈0.2 mm below the apparent upper boundary of the plasma. The camera pixels corresponding to the signal collection region were binned together prior to readout of the spectrum, resulting in spatial averaging over the signal collection volume for all data points taken.

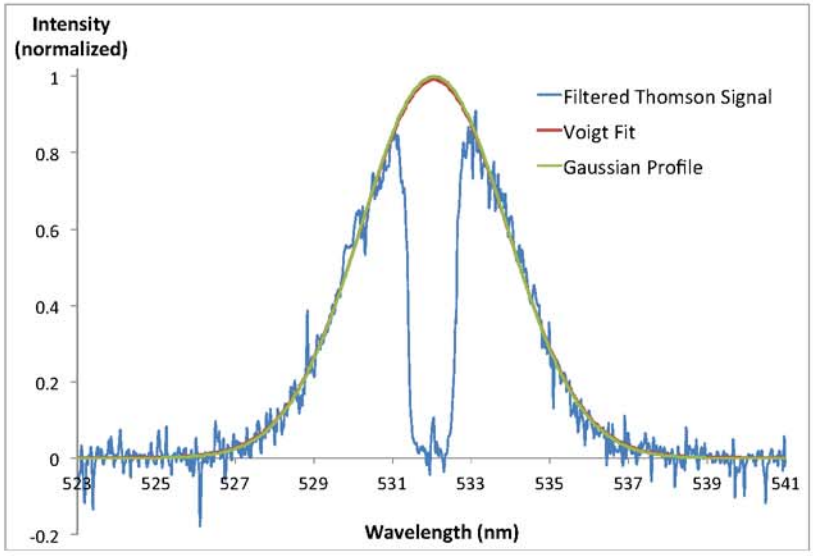

Figure 5.74: Typical Thomson scattering spectrum (helium, P=100 torr, 315 ns after start of surface ionization wave propagation), shown with least-squares Voigt fit and inferred Gaussian profile. From reference [48].

5.10 Near Surface Nanosecond Pulse Discharge: Electron Temperature, Electron Density and EEDF Results

This section presents the results in the near surface discharge Thomson scattering experiment, including time-resolved electron number density and electron temperature measurements, as well as Maxwellian electron energy distribution functions

(EEDFs) inferred from the Thomson scattering spectra. Portions of this discussion are taken from reference [48].

Figure 5.75 shows time-resolved electron density in the near-surface discharge in helium starting from 185 ns after the launch of the surface ionization wave (i.e. the beginning of the primary current pulse) to 945 ns (just after the secondary current pulse), plotted along with the current waveform. As illustrated in figure 5.75, $t = 185$ ns is the beginning of the main current pulse, while the secondary current pulse begins at $t \approx 750$ ns. Initially, the electron density increases rapidly, from approximately $n_e \approx 2 \cdot 10^{13}$ cm^{-3} to the peak value of $n_e \approx 3 \cdot 10^{14}$ cm^{-3}, an increase of over an order of magnitude, over approximately 75 ns. The electron density then begins to decay gradually over the next ≈500 ns. During this period, the electron density decay is likely dominated by dissociative recombination (see equation 5.24), as detected previously in the nanosecond pulse, sphere-to-sphere filament discharge in helium (see section 5.8). Dissociative recombination is a relatively slow process, where the estimated recombination time for $T/T_e \approx 0.1$ is $\tau_{rec} \approx (\beta n_e)^{-1}$ ≈10 μs, where, $\beta \approx 8.9 \cdot 10^{-9}$ $(T/T_e)^{3/2}$ cm^3/s, is the dissociative recombination rate coefficient in helium [55]. Subsequently, a secondary increase in electron density is observed, which is due to the additional energy coupling to the plasma by the secondary discharge pulse. In essence, the electron density follows the discharge current. After the secondary pulse is over, the electron density begins to decay once again.

Figure 5.76 plots time-resolved electron temperature at the conditions of figure 5.75. Peak electron temperature measured was $T_e \approx 4.25$ eV at $t = 185$ ns. It is likely that the electron temperature at shorter delay times (before the surface

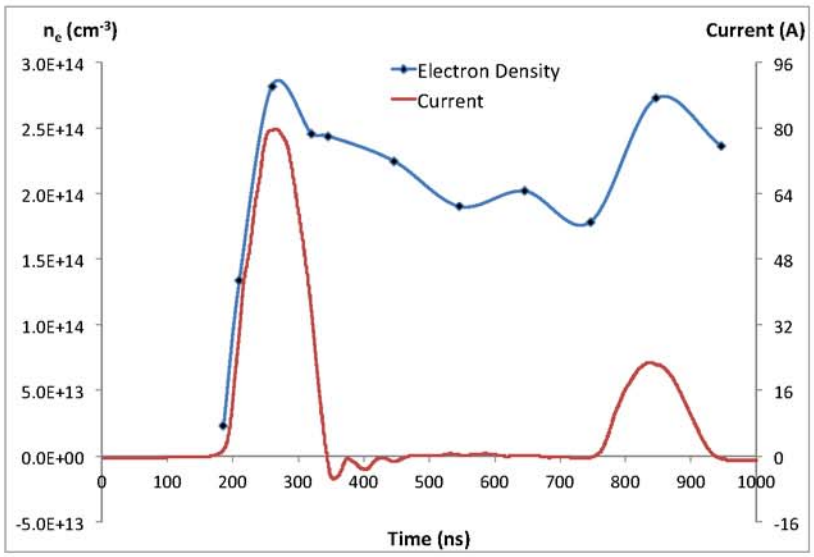

Figure 5.75: Time-resolved electron number density in the near surface, nanosecond pulse discharge experiment (helium, P=100 torr, ≈14 mJ/pulse). From reference [48].

ionization wave reaches the grounded electrode) is higher. However, the present diagnostic is not sufficiently sensitive to take data at shorter delay times, due to relatively low electron density. At $t > 185$ ns, the electron temperature rapidly drops to ≈0.5 eV over ≈150 ns. After this, the electron temperature decreases more slowly. This slower trend is likely due to superelastic collisions (see equation 5.23) becoming significant and providing moderate electron heating in the afterglow [49]. At $t \approx 750$ ns, a brief transient rise of electron temperature occurs, up to $T_e \approx 1.25$ eV. This is caused by the secondary discharge pulse coupling additional energy to the plasma; note that this transient rise coincides in time with the secondary current pulse. After the secondary pulse, the electron temperature rapidly decreases once again.

Figures 5.77 and 5.78 show the time-resolved electron energy distribution functions (EEDFs) for the near surface discharge study in helium. All EEDFs presented

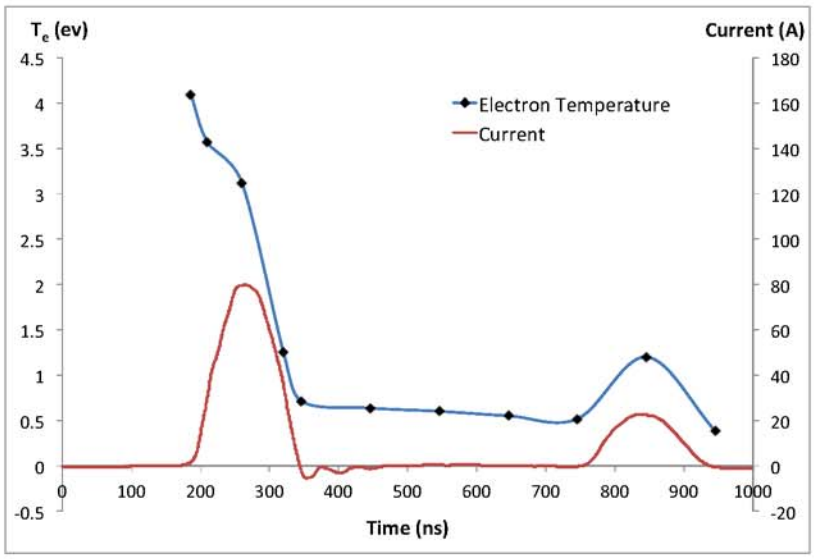

Figure 5.76: Time-resolved electron temperature in the near surface, nanosecond pulse discharge experiment (helium, P=100 torr, ≈14 mJ/pulse). From reference [48].

here are Maxwellian EEDFS, inferred from the electron number density and electron temperature values for each temporal data point (see section 5.5 for data reduction details). Figure 5.77 gives the EEDFs for the short time delays, from t=240 ns - 375 ns after the start of the surface ionization wave propagation. The results suggest that from 240 ns to 315 ns (i.e during the primary discharge pulse), that electrons with high energies are present, with the EEDFs having a well pronounced, high-energy tail, with energies of up to ≈20 eV. Shortly after this (t=375 ns), the electrons begin to cool, such that the EEDF tail rapidly disappears and lower electron energies become prevalent.

Figure 5.78 gives the EEDFs for the long time delays, from t=400 ns - 1 μs after the start of the surface ionization wave propagation. The trend of the EEDFs are seen to be converging toward low electron energies, with electrons losing energy until

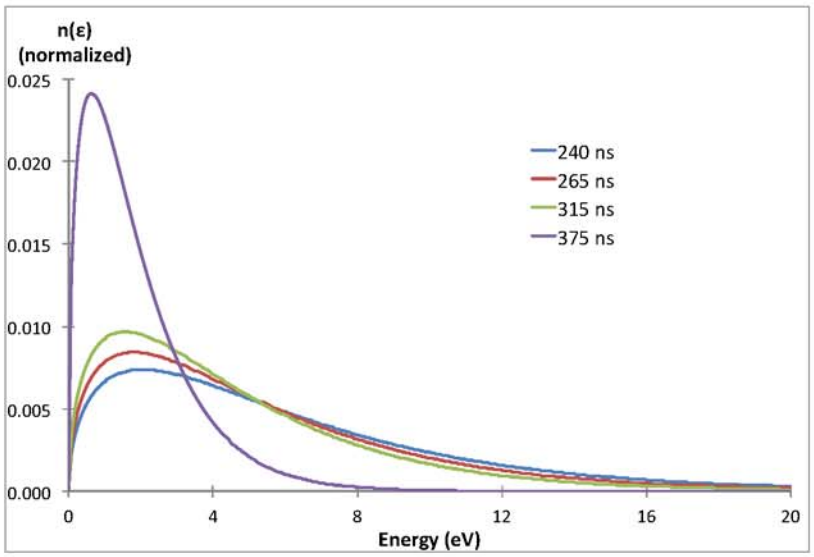

Figure 5.77: Time-resolved Maxwellian EEDFs for t=240 ns-375 ns after start of the ionization wave propagation in a near-surface, nanosecond pulse discharge in helium (P=100 torr, ≈14 mJ/pulse).

t=800 ns, where additional coupling of energy by the secondary discharge pulse causes the electrons to gain energy once again, such that the EEDF tail extends out to ≈6 eV (with an order of magnitude drop in population). After this ($t > 900$ ns), the electrons lose energy once again, and the EEDF exhibits dominance of low energy electrons. Similar to the conclusion made in section 5.8, comparison of the present results with kinetic modeling calculations can be used for model validation, as well as to verify if the EEDF in the near-surface discharge is fully Maxwellian (i.e. even at high electron energies).

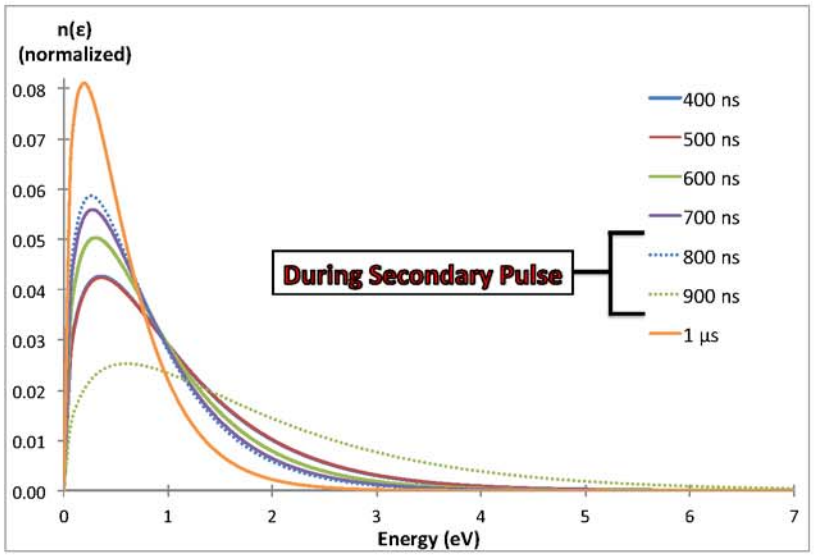

Figure 5.78: Time-resolved Maxwellian EEDFs for t=400 ns-1 μs after start of the ionization wave propagation in a near-surface, nanosecond pulse discharge in helium (P=100 torr, $\approx$14 mJ/pulse).

Chapter 6: Conclusions and Future Work

This dissertation has presented studies of fundamental dynamics and kinetics of nonequilibrium plasmas in nanosecond pulse discharges. Nanosecond pulse, high energy ($\geq$4 mJ/pulse), discharges at moderate pressure (75-200 torr) have been studied in a number of gas mixtures including nitrogen, helium, hydrogen and oxygen. Measurements of fundamental characteristics of plasmas in these discharges have been accomplished using laser scattering diagnostic techniques, including spontaneous Raman scattering and Thomson scattering.

Time-resolved measurements of N_2 vibration distribution function (VDF), 'first-level' N_2 vibrational temperature (T_{V01}), electron number density (n_e), electron temperature (T_e) and electron energy distribution function have been conducted in different types of nanosecond pulse, electric discharges. Electron number density, electron temperature and EEDF control the local energy loading and electron energy partition in the plasma (specifically, ionization and recombination rate coefficients), and therefore provide insight into rates of production of species in nanosecond pulse discharges which are critical for applications such as plasma flow control (PFC) and plasma assisted combustion (PAC). In addition, time-resolved measurements of vibrational distribution function (VDF) and vibrational temperature (T_V) provide insight into the rates of processes controlling vibrational energy loading and relaxation in nanosecond

pulse discharges in molecular gases, and are important for NO formation (a regulated pollutant), plasma lifetime (specifically in air plasmas) and the rate of temperature increase.

Spontaneous Raman scattering has been used to study temporal evolution of the N_2 vibrational distribution function (VDF) in nitrogen and air, in a nanosecond pulse, 'diffuse filament' discharge sustained between two spherical electrodes. Highly nonequilibrium conditions were observed, with vibrational levels up to $v = 12$ in nitrogen and $v = 11$ in air significantly populated and detected. First-level N_2 vibrational temperature has also been measured, and found to exceed $T_v = 2500$ K in air and 4000 K in nitrogen, while the rotational/translational temperature at these conditions is expected to be ≈500-1000 K, indicating highly nonequilibrium conditions. Time-resolved average number of vibrational quanta per N_2 molecule have also been measured, indicating a significant rise during the discharge pulse. Results in nitrogen have been compared with 0-D kinetic modeling predictions. Trends for the N_2 VDFs and first-level N_2 vibrational temperature were reproduced well by the model. However, VDF decay rate was significantly overpredicted, while the rate of the secondary rise in vibrational temperature after the discharge pulse was underpredicted.

Future work in this area would be to perform kinetic modeling calculations for all experimental conditions tested, preferably using a 2-D kinetic model. This has the potential to shed light on several unresolved issues of N_2 vibrational kinetics in nanosecond pulse discharge plasmas, particularly the reason for the slower VDF decay rate than predicted by the 0-D model. Also, measurements of the time-resolved N_2 VDF for different O_2 fractions in nitrogen would be extremely helpful to study the

effect of oxygen molecules and O atoms in these plasmas in more detail (in particular, V-T relaxation of N_2 by O atoms).

A Thomson scattering diagnostic, for measurement of electron density, electron temperature and electron energy distribution (EEDF) has been developed. A custom-built, triple-grating spectrometer is used to filter out interference to the Thomson signal from Rayleigh scattering, as well as to block stray light from reaching the detector. Rayleigh scattering filtering is achieved using a spectral masking procedure, which utilizes a stainless steel mask to physically block the spectrally 'narrow' Rayleigh scattering signal, but allows the majority of the spectrally 'wide' Thomson signal through. The linear dispersion of the present diagnostic is ≈1 mm/nm, while the sensitivity level of Thomson scattering measurements allows for electron number density measurements down to $\approx 10^{12}$ cm^{-3}.

In the future, the Thomson scattering diagnostic sensitivity may be improved in several ways. First, current grating efficiencies are ≈40%. This results in only approximately 6.5% of the scattered signal propagating through the triple-grating spectrometer to the detector. This could be improved to ≈35% (i.e. by a factor of ≈5) using a modern transmission grating setup, where the individual transmission gratings have ≈70% efficiencies. This would require significant redesign of the triple grating spectrometer, but may well be worthwhile for studying lower electron density plasmas. Another possibility for improving the diagnostic sensitivity is replacing the ICCD camera with a more advanced, filmless ICCD. The camera used in the present experiments has a quantum efficiency of ≈10% at 532 nm. Currently available filmless ICCDs have potential for quantum efficiency of up to 50% at 532 nm, offering an additional factor of five improvement.

Temporally resolved electron number density, electron temperature and electron energy distribution function (EEDF) have been measured in a nanosecond pulse, 'diffuse filament' discharge, sustained between two spherical electrodes and in a near surface, nanosecond pulse discharge (initially developing as a surface ionization wave) using a Thomson scattering diagnostic. Experimental studies have been conducted in helium, as well as in various mole fractions of H_2 in helium and O_2 in helium. Sphere-to-sphere filament discharge results in helium, at high coupled pulse energy ($\approx$17 mJ/pulse), have been compared with 2-D, axisymmetric, kinetic modeling predictions. Modeling predictions have yielded insight into major electron density decay mechanisms (primarily dissociative recombination at the present conditions) as well as the importance of superelastic collisions during the discharge afterglow. At these conditions, electron densities were found to range from 10^{13} to 10^{15} cm^{-3}, while electron temperatures ranged from 0.1 to 7.0 eV.

Future work in this area would be to perform further, 2-D modeling calculations for the entire range of experimental conditions tested. This would greatly improve understanding of kinetic processes controlling EEDF in these discharges. Also, electron number density, electron temperature and EEDF measurements in N_2-He mixtures would be a significant advance for characterization of electron kinetics in air-species containing plasmas.

Bibliography

[1] A. Starikovskiy and N. Aleksandrov. "Plasma-Assisted Ignition and Combustion". *Prog. Energy Combustion Sci.*, 39:61–110, 2013.

[2] S.M. Starikovskaya. "Plasma Assisted Ignition and Combustion". *Journal of Physics D: Applied Physics*, 39(16):R265–R299, 2006.

[3] I.V. Adamovich, W.R. Lempert, J.W. Rich, and Y.G. Utkin. "Repetitively Pulsed Nonequilibrium Plasmas for Magnetohydrodynamic Flow Control and Plasma-Assisted Combustion". *Journal of Propulsion and Power*, 24(6):1198–1215, 2008.

[4] I.V. Adamovich, I. Choi, N. Jiang, J.H. Kim, S. Keshav, W.R. Lempert, E. Mintusov, M. Nishihara, M. Samimy, and M. Uddi. "Plasma Assisted Ignition and High-Speed Flow Control: Non-Thermal and Thermal Effects". *Plasma Sources Science and Technology*, 18(034018), 2009.

[5] J. Little, K. Takashima, M. Nishihara, I. Adamovich, and M. Samimy. "Separation Control with Nanosecond Pulse Driven Dielectric Barrier Discharge Plasma Actuators". *AIAA Journal*, 50:350–365, 2012.

[6] D.V. Roupassov, A.A. Nikipelov, M.M. Nudnova, and A. Starikovskii. "Flow Separation Control by Plasma Actuator with Nanosecond Pulsed-Periodic Discharge". *AIAA Journal*, 47(1):168, 2009.

[7] M. Nishihara, K. Takashima, J.W. Rich, and I.V. Adamovich. "Mach 5 Bow Shock Control by a Nanosecond Pulse Surface Dielectric Barrier Discharge". *Physics of Fluids*, 23:066101, 2011.

[8] A. Hicks, J.R. Bruzzese, and I.V. Adamovich. "Effect of Iodine Dissociation in an Auxiliary Discharge on Gain in a Pulser-Sustainer Discharge Excited Oxygen-Iodine Laser". *Journal of Physics D: Applied Physics*, 43:025206, 2010.

[9] J.R. Bruzzese, R. Richards, and I.V. Adamovich. "Effect of Flow Cooling on Gain and Output Power of an Electrically Excited Oxygen-Iodine Laser". *Journal of Physics D: Applied Physics*, 43:425206, 2010.

[10] David B. Graves. "The Emerging Role of Reactive Oxygen and Nitrogen Species in Redox Biology and some Implications for Plasma Applications to Medicine and Biology". *Journal of Physics D: Applied Physics*, 45:263001, 2012.

[11] V. Guerra and J. Loureiro. "Self-Consistent Electron and Heavy-Particle Kinetics in a Low-Pressure N_2-O_2 Glow Discharge". *Plasma Sources Science and Technology*, 6:373–385, 1997.

[12] K. Frederickson, W. Lee, P. Palm, I.V. Adamovich, J.W. Rich, and W.R. Lempert. "Mitigation of Electron Attachment to Oxygen in High Pressure Air Plasmas by Vibrational Excitation". *Journal of Applied Physics*, 101:093302, 2007.

[13] A. Montello, Z. Yin, D. Burnette, I.V. Adamovich, and W.R. Lempert. "Picosecond CARS Measurements of Nitrogen Vibrational Loading and Rotational/Translational Temperature in Non-equilibrium Discharges". *Journal of Physics D: Applied Physics*, 46:464002, 2013.

[14] D. Messina, B. Attal-Trétout, and F. Grisch. "Study of a Non-equilibrium Pulsed Nanosecond Discharge at Atmospheric Pressure using Coherent Anti-Stokes Raman Scattering". *Proc. Combustion Institute*, 31:825–832, 2007.

[15] A.A. Devyatov, S.A. Dolenko, A.T. Rakhimov, T.V. Rakhirnova, N.N. Roi, and N.V. Suetin. "Investigation of Kinetic Processes in Molecular Nitrogen by the CARS Method". *Sov. Phys.–JETP*, 63:246–250, 1986.

[16] C.T. Chang, M. Hashmi, and H.C. Pant. "Study of a Laser-Produced Plasma by Langmuir Probes". *Plasma Physics*, 19:1129–1138, 1977.

[17] W.P.S. Tan. "Langmuir Probe Measurement of Electron Temperature in a Druyvesteyn Electron Plasma". *Journal of Physics D: Applied Physics*, 6:1206–1216, 1973.

[18] K. Dittmann, C. Küllig, and J. Meichsner. "160 GHz Gaussian Beam Microwave Interferometry in Low-Density RF Plasmas". *Plasma Sources Science and Tehcnology*, 21:024001, 2012.

[19] D.L. Crintea, D. Luggenhölscher, V.A. Kadetov, Ch. Isenberg, and U. Czarnetzki. "Phase Resolved Measurements of Anisotropic Electron Velocity Distribution Functions in a Radio-Frequency Discharge". *Journal of Physics D: Applied Physics*, 41:082003, 2008.

[20] Y. Noguchi, A. Matsuoka, M.D. Bowden, K. Uchino, and K. Muraoka. "Measurements of Electron Temperature and Density of a Micro-Discharge Plasma Using Laser Thomson Scattering". *Japan Journal of Applied Physics*, 40:326, 2001.

[21] R. Johnsen, E.V. Shun'ko, T. Gougousi, and M.F. Golde. "Langmuir-Probe Measurements in Flowing-Afterglow Plasmas". *Physical Review E: Statistical, Nonlinear, and Soft Matter Physics*, 50(5):3994–4004, 1994.

[22] O. Waldmann and G. Fussmann. "Influence of the Langmuir Probe Shaft on Measuring Plasma Parameters". *Contrib. Plasma Phys.*, 48(5-7):534–539, 2008.

[23] M. Laroussi. "Relationship Between the Number Density and the Phase Shift in Microwave Interferometry for Atmospheric Pressure Plasmas". *International Journal of Infrared and Millimeter Waves*, 20(8):1501–1508, 1999.

[24] Wonchul Lee. *"Development of Raman and Thomson Scattering Diagnostics for Study of Energy Transfer in Nonequilibrium, Molecular Plasmas"*. PhD thesis, The Ohio State University, 2003.

[25] Yuri P. Raizer. *"Gas Discharge Physics"*. Springer-Verlag, 1991.

[26] I. Shkurenkov, D. Burnette, W.R. Lempert, and I.V. Adamovich. "Kinetics of Excited States and Radicals in a Nanosecond Pulse Discharge and Afterglow in Nitrogen and Air". *Plasma Sources Science and Technology*, 23(065003), 2014.

[27] E. Plönjes, P. Palm, J.W. Rich, I.V. Adamovich, and W. Urban. "Electron-Mediated Vibration-Electronic (V-E) Energy Tansfer in Optically Pumped Plasmas". *Chemical Physics*, 279:43–54, 2002.

[28] V. Guerra, P.A. Sá, and J. Loureiro. "Role Played by the $N_2(A^3\sum_u^+)$ Metastable in Stationary N_2 and N_2-O_2 Discharges". *Journal of Physics D: Applied Physics*, 34:1745–1755, 2001.

[29] I.V. Adamovich, S. Saupe, M.J. Grassi, O. Shulz, S. Macheret, and J.W. Rich. "Vibrationally Stimulated Ionization of Carbon Monoxide in Optical Pumping Experiments". *Chemical Physics*, 173:491–504, 1993.

[30] C.E. Treanor, J.W. Rich, and R.G. Rehm. "Vibrational Relaxation of Anharmonic Oscillators with Exchange-Dominated Collisions". *Journal of Chemical Physics*, 48:1798–1807, 1968.

[31] M. Cacciatore, A. Kurnosov, and A. Napartovich. "Vibrational Energy Transfer in N2-N2 Collisions: A New Semiclassical Study". *Journal of Chemical Physics*, 123:174315, 2005.

[32] G.D. Billing and E.R. Fisher. "VV and VT Rate Coefficients in N_2 by a Quantum-Classical Model". *Chemical Physics*, 43:395–401, 1979.

[33] I.V. Adamovich, S.O. Macheret, and J.W. Rich. "Spatial Nonhomogeneity Effects in Nonequilibrium Vibrational Kinetics". *Chemical Physics*, 182:167–183, 1994.

[34] Gabriel Laufer. *"Introduction to Optics and Lasers in Engineering"*. Cambridge University Press, 1996.

[35] Alan C. Eckbreth. *"Laser Diagnostics for Combustion Temperature and Species"*. Overseas Publishers Association under license from Gordon and Breach Science Publishers, 2 edition, 1996.

[36] A.M. Roettgen, W.R. Lempert, and I.V. Adamovich. "Measurements of N_2 Vibrational Distribution Function in Pulsed Nanosecond Nonequilibrium Discharge by Spontaneous Raman Scattering". *51st AIAA Aerospace Sciences Meeting, Grapevine, TX*, AIAA 2013-0576, Jan. 2013.

[37] A. Lo, G. Cléon, P. Vervisch, and A. Cessou. "Spontaneous Raman Scattering: A Useful Tool for Investigating the Afterglow of Nanosecond Scale Discharges in Air". *Applied Physics B: Lasers and Optics*, 107:229–242, 2012.

[38] N.L. Aleksandrov, F.I. Vysikailo, R.Sh. Islamov, I.V. Kochetov, A.P. Napartovich, and V.G. Pevgov. "Electron Distribution Function in 4:1 N_2-O_2 Mixture". *High Temperature*, 19:17–21, 1981.

[39] N.L. Aleksandrov, F.I. Vysikailo, R.Sh. Islamov, I.V. Kochetov, A.P. Napartovich, and V.G. Pevgov. "A Theoretical Model for a Discharge in an N_2:O_2 = 4:1 Mixture". *High Temperature*, 19:342–346, 1981.

[40] I.V. Adamovich, V.I. Borodin, A.P. Chernukho, J.W. Rich, and S.A. Zhdanok. "N_2 Isotope Separation in Nonequilibrium Reactions of Nitrogen Oxidation in DC Electric Discharge Systems". *26th Plasmadynamics and Lasers Conference, San Diego, CA*, AIAA 95-1988, Jun. 1995.

[41] C.E. Treanor, I.V. Adamovich, M.J. Williams, and J.W. Rich. "Kinetics of NO Formation Behind Strong Shock Waves". *Journal of Thermophysics and Heat Transfer*, 10:193–198, 1996.

[42] I.A. Kossyi, A.Yu Kostinsky, A.A. Matveyev, and V.P. Silakov. "Kinetic Scheme of Nonequilibrium Discharge in Nitrogen-Oxygen Mixtures". *Plasma Sources Science and Technology*, 1:207–220, 1992.

[43] John Sheffield. *"Plasma Scattering of Electromagnetic Radiation"*. Academic Press, Inc., 1975.

[44] Vladimir N. Ochkin. *"Spectroscopy of Low Temperature Plasma"*. Wiley-VCH Verlag GmbH, 2009.

[45] E.E. Salpeter. "Electron Density Fluctuations in a Plasma". *American Physical Review*, 120(5):1528–1535, Dec. 1960.

[46] Peter F. Bernath. *"Spectra of Atoms and Molecules"*. Oxford University Press, Inc., second edition, 2005.

[47] Jobin-Yvon Spex. *"Guide for Spectroscopy"*. Instruments S.A., 1994.

[48] A.M. Roettgen, V. Petrishchev, W.R. Lempert, and I.V. Adamovich. "Thomson Scattering Measurements of Electron Density and Electron Temperature in a Nanosecond Pulse Surface Discharge". *SciTech 2015: 53rd AIAA Aerospace Sciences Meeting, Kissimmee, FL*, AIAA 2015-1829, Jan. 2015.

[49] A.M. Roettgen, I. Shkurenkov, W.R. Lempert, and I.V. Adamovich. "Thomson Scattering Studies in He and He-H_2 Nanosecond Pulse Nonequilibrium Plasmas". *SciTech 2014: 52nd AIAA Aerospace Sciences Meeting, National Harbor, MD*, AIAA 2014-1358, Jan. 2014.

[50] T. Hori, M. Kogano, M.D. Bowden, K. Uchino, and K. Muraoka. "A Study of Electron Energy Distributions in an Inductively Coupled Plasma by Laser Thomson Scattering". *Journal of Applied Physics*, 83(4):1909–1916, 1998.

[51] Yukikazu Itikawa. "Cross Sections for Electron Collisions with Nitrogen Molecules". *J. Phys. Chem. Ref. Data*, 35(1), 2006.

[52] Terrence S. Brown and D.J. Rose. "Plasma Diagnostics using Lasers: Relations between Scattered Spectrum and Electron-Velocity Distribution". *Journal of Applied Physics*, 37(7):2709–2714, Jun. 1966.

[53] A.M. Roettgen, I. Shkurenkov, W.R. Lempert, and I.V. Adamovich. "Time-Resolved Electron Temperature and Number Density Measurements in a Nanosecond Pulse Filament Discharge Using Thomson Scattering". *Aviation 2014: 45th AIAA Plasmadynamics and Lasers Conference, Atlanta, GA*, AIAA 2014-2113, Jun. 2014.

[54] Leonard G.H. Huxley. *"Diffusion and Drift of Electrons in Gases"*. John Wiley & Sons, inc., 1974.

[55] Yu.B. Golubovskii, V.A. Maiorov, J. Behnke, and J.F. Behnke. "Modelling of the Homogeneous Barrier Discharge in Helium at Atmospheric Pressure". *Journal of Physics D: Applied Physics*, 36:39–49, 2003.